Universidade de Aveiro Departamento de Engenharia Mecânica
2007

Thomas Fiedler

Métodos experimentais e numericos no estudo de estruturas de esferas ocas em painéis sanduíche

Numerical and Experimental Investigation of Hollow Sphere Structures in Sandwich Panels

Universidade de Aveiro Departamento de Engenharia Mecânica
2007

Thomas Fiedler

Métodos experimentais e numericos no estudo de estruturas de esferas ocas em painés 'sandwich'

Numerical and Experimental Investigation of Hollow Sphere Structures in Sandwich Panels

tese apresentada à Universidade de Aveiro para cumprimento dos requisitos necessários à obtenção do grau de Doutor em Engenharia Mecânica, realizada sob a orientação científica do Dr. Andreas Öchsner, Professor Auxiliar Convidado, e do Professor José Grácio, Professor Catedrático, do Departamento de Engenharia Mecânica da Universidade de Aveiro

Apoio financeiro da FCT e do FSE no âmbito do III Quadro Comunitário de Apoio.

o júri

presidente

Prof. Doutor Carlos Alberto Diogo Soares Borrego
Professor Catedrático da Universidade de Aveiro

Prof. Doutor José Joaquim de Almeida Grácio
Professor Catedrático da Universidade de Aveiro

Prof. Doutor Andreas Oechsner
Full Professor of Technical University of Malaysia

Prof. Doutor Ulrich Krupp
Professor of University of Applied Sciences – Osnabrick - Germany

Prof. Doutor António Joaquim Mendes Ferreira
Professor Associado da Faculdade de Engenharia da Universidade do Porto

Prof. Doutor Filipe Miguel Horta e Vale Teixeira-Dias
Professor Auxiliar da Universidade de Aveiro

agradecimentos

Firstly and over all, I would like to thank my supervisor, Prof. Andreas Öchsner. I could not have imagined having a better advisor and mentor for my PhD, and without his support, guidance and knowledge my work on this thesis would not have been such an instructive and joyful experience.

Special thanks go to Dr. Matej Vesenjak and Prof. Zoran Ren for a great time and the joint work on impact behavior of MHSS at the University of Maribor, Slovenia. Furthermore, I want to acknowledge Eusebio Solórzano for the experimental data of the thermal conductivities of MHSS.

Dr. Richard Howard and Prof. Graeme Murch tremendously helped to improve this thesis by correcting the English and I honestly appreciate the time they spent reading my thesis. I also want to acknowledge MSc Filipe Ferreira for his support with the Portuguese translations.

I would also like to thank the academic staff and colleagues at the University of Aveiro, Portugal for their support of my thesis. I especially want to point out the contributions of several German exchange-students who supported my research in the scope of internships, student projects, diploma theses and BBQ's.

Furthermore, I want to acknowledge Dipl.-Ing. Gerd Bingel and the German company Glatt GmbH, Dresden, for their kind support and the allocation of metallic hollow spheres specimens.

Finally, I want to sincerely thank my family for moral support across three borders of Europe. And last but not least Mirja, for the very special person she is - and for the incredible amount of patience she had with me in the last two years.

palavras-chave

metais celulares, estruturas metálicas com vazios esféricos estruturas sanduíche, propriedades mecânicas, propriedades térmicas, método dos Elementos Finitos, testes experimentais

resumo

O presente trabalho propõe estudar o comportamento de estruturas compostas por esferas ocas metálicas em painéis sanduíche. Estudos numéricos utilizando o método de Elementos Finitos foram feitos para caracterizar o comportamento de provetos representativos. A primeira parte do estudo envolveu o estudo de diferentes tipos de estruturas metálicas compostas por esferas ocas metálicas, adesivamente fundidas, MHSS ("Metallic Hollow Sphere Structures"). A influência da morfologia, topologia e da técnica de fusão das esferas nas propriedades materiais foi avaliada numericamente. Testes de compressão uni-axial com provetes MHSS confirmaram os resultados numéricos. A condutividade térmica dos provetes MHSS foi também avaliada. A segunda parte do trabalho concentra-se na deformação utilizando 3 pontos de aplicação de força em painéis sanduíche compostos por chapas de alumínio envolvendo vários materiais celulares como espumas M-Pore® e Alporas® em alumínio, estruturas em forma de colméia e MHSS adhesivamente fundidas. A resistência à deformação, a capacidade de carga do material e o modo de falha foram verificados através de testes de flexão utilizando 3 pontos de aplicação de força. A comparação dos resultados experimentais possibilita a comparação entre os vários materiais celulares no que diz respeito às propredades testadas.

keywords

cellular metalls, metallic hollow sphere structures, sandwich structures, mechanical properties, thermal properties, finite element method, experimental testing.

abstract

This thesis addresses the performance of novel metallic hollow sphere structures (MHSS) in sandwich panels. Numerical finite element analyses and experimental tests are conducted. The first part of this thesis focuses on different types of metallic hollow sphere structures. The influence of the morphology, topology, joining technology and material composition on their mechanical properties is numerically investigated. Uni-axial compressive tests with adhesively bonded MHSS are performed in order to confirm the numerical findings. In addition, the effective thermal conducivities of MHSS are determined. The main focus of the second part of this work lies on experimental three-point bending tests of sandwich panels. The investigated sandwich panels are assembled by aluminium face sheets which enclose different cellular core materials, namely M-Pore® and Alporas® aluminium foams, honeycomb structures and adhesively bonded MHSS. The flexural stiffness, the load-carrying capacity and the failure mode are determined using three-point bending tests. The comparison of these experimental findings allows for the performance valuation of different cellular metal cores.

Table of Contents

1 Introduction **1**
- 1.1 Cellular Metals . . . 1
- 1.2 Potential for cellular lightweight structures . . . 3
- 1.3 Sandwich Structures . . . 6
- 1.4 State of the research . . . 7

2 Theoretical Foundation **10**
- 2.1 Mechanics . . . 10
  - 2.1.1 Linear Elasticity . . . 10
  - 2.1.2 Plasticity . . . 11
- 2.2 Heat transfer . . . 18
  - 2.2.1 Thermal conduction . . . 18
  - 2.2.2 Thermal convection . . . 19
  - 2.2.3 Thermal radiation . . . 20

3 Methodology **21**
- 3.1 Finite Element Method . . . 21
  - 3.1.1 Mathematics . . . 21
  - 3.1.2 Geometry . . . 26
  - 3.1.3 Discretisation . . . 28
  - 3.1.4 Material Properties . . . 35
- 3.2 Experimental Testing . . . 37
  - 3.2.1 Mechanical Testing . . . 37
  - 3.2.2 Thermal Testing . . . 43

4 Results **45**
- 4.1 Hollow Sphere Structures . . . 45
  - 4.1.1 Mechanical Properties: Finite Element Method . . . 45
  - 4.1.2 Mechanical Properties: Experimental findings . . . 68
  - 4.1.3 Mechanical Properties: Impact Behaviour . . . 73
  - 4.1.4 Thermal Properties . . . 81
- 4.2 Sandwich Structures . . . 91
  - 4.2.1 Mechanical Properties: Experimental Findings . . . 91
  - 4.2.2 Mechanical Properties: Finite element approach . . . 108
  - 4.2.3 Minimum weight design . . . 111
  - 4.2.4 Thermal Properties of sandwich structures . . . 114

5 Conclusions **117**

6 Future research work **121**

References **131**

List of symbols

Arabic minuscules

Symbol	Description
b	Deflection due to bending
b_s	Deflection due to shear loading
b_t	Total deflection due to bending and shear loading
c	Core thickness of a sandwich structure
$\boldsymbol{d}$	Nodal displacements vector
d_min	Minimum distance between two neighboring spheres
d_o	Overhang of the specimen in the three-point bending test
d_s	Distance between the supports in the three-point bending test
f	Face sheet thickness
h	Total height of a sandwich structure
$\overline{\boldsymbol{k}}$	Stiffness matrix
$k_{0.2}$	0.2 % offset yield strength
k_c	Compressive yield stress
k_t	Tensile yield stress
k^c	Yield stress of the core material
k^f	Yield stress of the face sheet material
l	Total length of a sandwich structure
l_s	Side length of a unit cell
m	Mass of a sandwich structure
p	Cowper Symond strain rate parameter
$\boldsymbol{p}$	Volume load
$\hat{\boldsymbol{p}}$	Vector of external loads
$\mathbf{q}$	Hardening tensor
$\boldsymbol{q}$	Area load
r	Inner radius of the spherical shell
s	Scale factor
t	Thickness of the spherical shell
t_adh	Thickness of the adhesive layer joining face sheets and core material
u	flexural deflection
u_max	Maximum tolerable deflection
w	Width of a sandwich structure
w_pl	Specific plastic work

Arabic capitals

Symbol	Description
C	Cowper Symond strain rate parameter
C_{ijkl}	Elasticity tensor
$\overline{\mathbf{C}}$	Elasticity matrix
$\overline{\boldsymbol{D}}$	Differential operator matrix
E	Young's modulus
E_{Str}	Flexural stiffness of sandwich structures
F	Force
F_{cr}	Critical force of failure initiation in the three-point bending
F_{max}	Maximum force in the three-point bending test
F_{min}	Required minimum load-carrying capacity of a sandwich structure
F_{r}	Reaction force
G	Shear modulus
$\overline{\boldsymbol{G}}$	Matrix of the trial functions
I_{zz}	Geometrical moment of inertia
K	Bulk modulus
M	Torque
N_i	Shape function
P	Plateau modulus
Q	Shear force
R	Thermal resistance
$\dot{Q}$	Sum of the nodal heat fluxes
$\dot{Q}_{\mathrm{cond}}$	Conductive heat flux
$\dot{Q}_{\mathrm{conv}}$	Convective heat flux
$\dot{Q}_k$	Nodal heat flux
$\dot{Q}_{\mathrm{rad}}$	Radiation heat flux
$\dot{Q}_{\mathrm{tot}}$	Total heat flux
R	Outer radius of the spherical shell
T_1, T_2	Constant temperature boundary conditions
V_{free}	Totalised volume of the void(s) inside the unit cell
V_{M}	Totalised volume of the matrix inside the unit cell
V_{rel}	Relative volume of the voids
V_{S}	Totalised volume of the spherical shell(s) inside the unit cell
V_{U}	Volume of the unit cell
W_{el}	Elastic energy
W_{pl}	Plastic energy
W_{tot}	Total absorbed energy
δW	Virtual work

Greek minuscules

Symbol	Description
δ	Standard deviation
$\overline{\delta}$	Normalised standard deviation
ε	Total strain tensor
ε_{D}	Densification strain
$\varepsilon_{\mathrm{el}}$	Elastic strain tensor
$\varepsilon_{\mathrm{eff}}^{\mathrm{pl}}$	Equivalent plastic strain
ε_{p}	Plastic strain tensor
λ	Thermal conductivity
λ_{eff}	Effective thermal conductivity of MHSS
η	Coordinate in the unit space
ν	Poison's ratio
$\overline{\rho}$	Average density
ρ_{c}	Density of the core material
ρ_{f}	Density of the face sheet material
ρ_{m}	Density of the matrix material
ρ_{s}	Density of the spherical shell material
σ	Stress tensor
$\sigma_{\mathrm{I,II,III}}$	Principal stresses
σ_{eff}	Effective stress
σ_{max}	Maximum stress of a MHSS before densification
σ_{pl}	Stress level at the beginning of the stress plateau
τ^{c}	Shear strength of the core material
ξ	Coordinate in the unit space

Greek capitals

Symbol	Description
Θ	Angle in the principal stress space

List of abbreviations

Abbreviation	**Description**
Al	Aluminium
Ep	Epoxy resin
EPS	Expanded poly styrol
FEM	Finite element method
MHSS	Metallic hollow sphere structure
St	Steel
TPS	Transient plane source

1 Introduction

1.1 Cellular Metals

The concept of porous and cellular metals first emerged in the beginning of the 1970's [1, 2, 3]. The basic idea seeks to imitate the cellular structure of high performance lightweight structures in nature such as the human osseus structure and can therefore be related to the field of bionic research. A closely related approach has already been successfully brought into application in both the aviation industry [4, 5] and the space industry [6, 7] through the use of hexagonal honeycomb structures in sandwich cores. During the last few years, techniques for the manufacturing of novel cellular and porous metals have been developed [8, 9]. These materials exhibit a significant potential for future oriented applications due to their specific properties.

By definition, cellular metals are materials with high porosity which are divided into distinct cells. The boundaries of these cells are made of solid metal, whilst the internal regions are air cavities. Cellular metals therefore exhibit densities which are typically below 10% of their corresponding base metal. This porosity can be quantified by the relative volume V_{rel} which is the volume occupied by the base material divided by the total volume of the structure. Two special cases of cellular metals are metallic foams and sponges. Metallic foams like Alporas® (cf. Fig. 1a)) originate from a liquid and are characterised by closed cells. Metallic sponges such as M-Pore®, (cf. Fig. 1b) are characterised by an interconnected porosity of open cells. Both, metallic foams and sponges exhibit a random geometry within their microstructure. In contrast to cellular metals, porous metals contain a multitude of microscopic pores and the densities of these materials are in the range of their base material(s). It should be mentioned here, that the definitions of metallic foam, sponge and porous metals are not mutually exclusive.

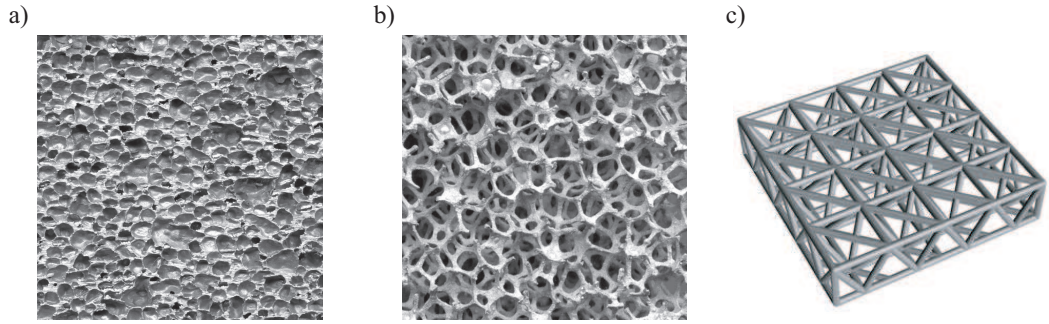

Figure 1: Cellular metals: a) Alporas® aluminium foam; b) M-Pore® aluminium sponge; c) Lattice block material [10].

Well-known advantages of cellular metals are their excellent ability for energy adsorption [11, 12, 13], good damping behaviour [14, 15, 16], sound absorption [17],

excellent heat insulation [18, 19, 20] and a high specific stiffness [21, 22, 23]. The combination of these properties opens a wide field of potential applications, e.g. in automotive, aviation or space-industry [24, 25, 26]. However, despite more than 30 years of intensive scientific research few industrial applications of these technologies can be found. Essential limiting factors for the utilisation are unevenly distributed material parameters [27, 28] and relatively high production costs. Less variation in the mechanical properties can be achieved with lattice block materials (cf. Fig. 1c)). These structures are manufactured by investment casting and therefore exhibit a well defined, reproducible geometry. This manufacturing technology is only able to produce open celled structures. Further limitations are high costs and anisotropic properties caused by the microstructure orientation.

Metallic hollow sphere structures (MHSS) are a new group of cellular metals characterised by easily reproducible geometry and therefore consistent mechanical and physical properties. A new powder metallurgy based manufacturing process enables the production of metallic hollow spheres of defined geometry [29]. This technology brings a significant reduction in costs in comparison to earlier applied galvanic methods and all materials suitable for sintering can be applied. EPS (expanded poly styrol) spheres are coated with a metal powder - binder suspension by turbulence coating. The green spheres produced can either be sintered separately to manufacture single hollow spheres or be pre-compacted and sintered in bulk (cf. Fig. 2) thus creating sintering necks between adjacent spheres [30]. Depending on the parameters of the sintering process the micro-porosity of the sintered cell wall can be adjusted. In a subsequent debindering process, the EPS spheres are pyrolised. The increase of the carbon content of the sintered metal by the diffusion of the incinerated binder and polymer causes degradation of mechanical properties and corrosion resistance. Special reducing processes are required to reduce this effect [31].

Various joining technologies such as sintering, soldering and adhering can be used to assemble the single hollow spheres to interdependent structures [32, 33]. Adhering is the most economic way of joining and therefore is attractive for a wide range of potential applications. Another important advantage is the possible utilisation of the mechanical behaviour and morphology of the adhesive layer as a further design parameter for the optimisation of the structure's mechanical properties for specific applications. Figure 3 shows two different types of adhesively bonded MHSS. In the case of syntactic morphology, the hollow spheres are completely embedded within the adhesive matrix. In contrast, the adhesive is concentrated at the contact points of neighboring spheres for partial MHSS. Consequently, partial MHSS also exhibit interconnected porosity.

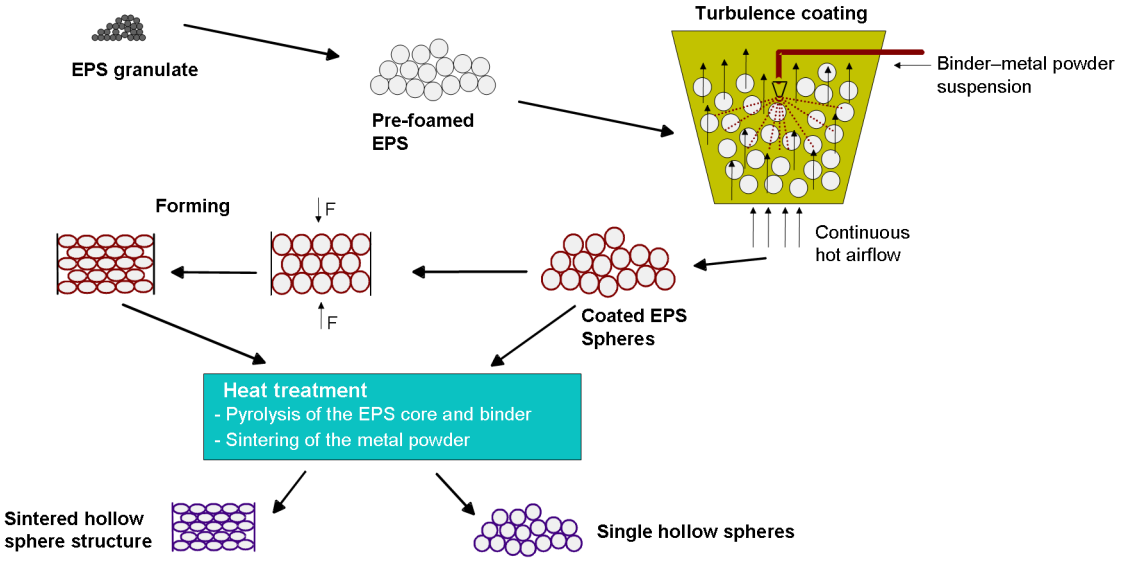

Figure 2: Manufacturing process of metallic hollow sphere structures.

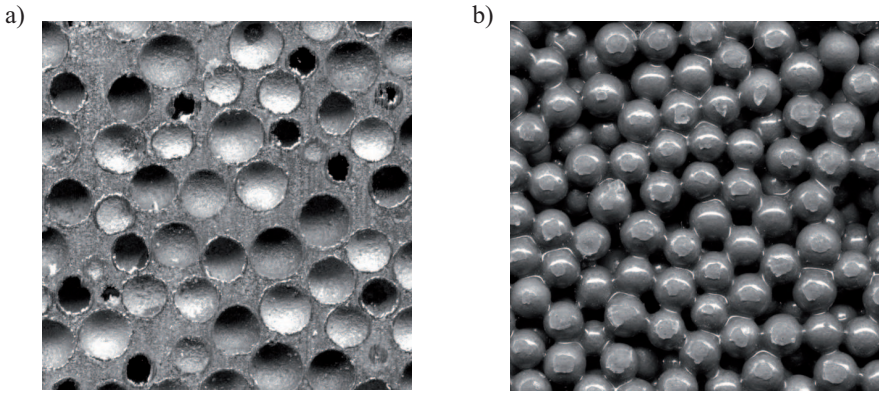

Figure 3: Adhesively bonded MHSS: a) Cross section of a syntactic MHSS; b) Partial morphology.

1.2 Potential for cellular lightweight structures

Cellular metals exhibit a multitude of interesting properties. Based on these characteristics, highly integrated applications can be created. Figure 4 shows several basic properties. First, due to the high porosity of MHSS, the material is able to compress at high strains. Figure 4 comprises a stress-strain relation of a MHSS. A distinct stress plateau can be observed which characterises the ability of the structure to absorb energy at a low stress level and high strains. This property enables the application of MHSS in energy absorbing structures, e.g. crash elements in the automotive industry [25].

Another clear attribute of cellular structures is the damping of mechanical and acoustic oscillations. In conjunction with its low density, this property suggests the

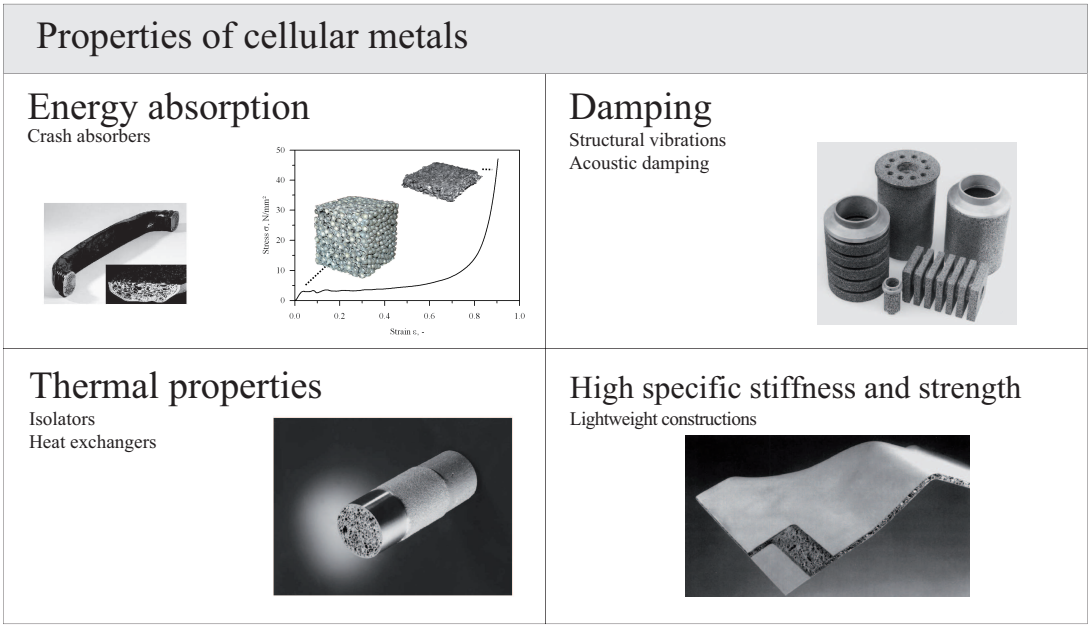

Figure 4: Properties of cellular metals (right side [8], left side [34]).

utilisation in parts where high accelerations occur. Oscillations can be damped and energy consumption be reduced due to the small amount of accelerated mass. The significant potential of hollow sphere composite structures in machine tools has already been demonstrated [35, 36]. Furthermore, cellular metals can act as sound suppressor and acoustic insulator.

Cellular metals also exhibit a low thermal conductivity in comparison to their base materials. In particular, adhesively bonded MHSS show very low thermal conductivities, due to the insulating effect of the adhesive matrix between the metallic shells of the spheres. Consequently, MHSS can be applied as thermal insulators. Other approaches aim for the utilisation of metallic sponges inside heat exchangers [37, 38]. However, since MHSS exhibit no (syntactic morphology) or only low (partial morphology) interconnected porosity, they possess a high flow resistance and are not suitable for such applications.

One of the most important properties of cellular metals is their high specific stiffness and strength. This principle also occurs in nature (e.g. osseus structure) and was one of the initial impulses for the research on cellular materials. In Fig. 5 Young's modulus and the compressive strength are plotted on a logarithmic scale versus the averaged density of the structures. The mechanical properties of adhesively bonded MHSS (bold circles ◯) are compared to various other cellular metals from the *Metfoam*'97 database. It can be observed that adhesively bonded MHSS exhibit a relatively poor specific stiffness which can be explained by the low stiffness of the adhesive matrix within the structure. However, the MHSS show excellent compressive strengths in

comparison to the other cellular structures.

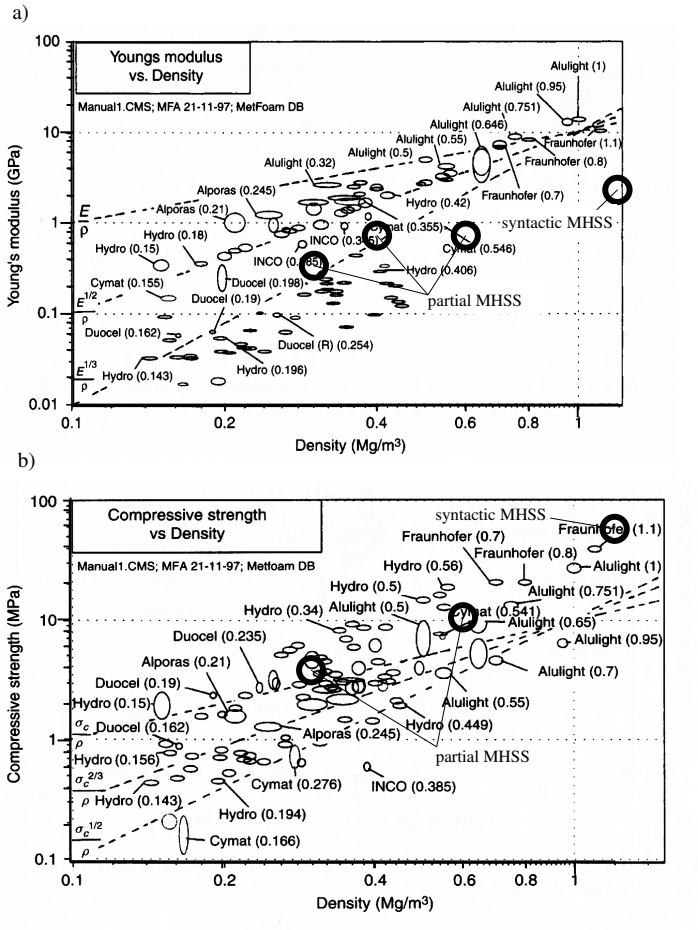

Figure 5: Modified Ashby diagram from [21].

As mentioned before, the scattering of material parameters [27, 28] represents the essential limiting factor for the industrial application of cellular metals. This problem can be overcome by the utilisation of classical regular honeycomb structures or lattice block materials. However, these materials require expensive manufacturing and processing techniques and are characterised by their anisotropic properties. Due to their potential lower production costs and macroscopic isotropic properties MHSS provide an attractive alternative. Their biggest potential lies in multifunctional applications [11]. One particularly good example that brings together many features of MHSS is the coachwork in automotive industry. The benefits of lightweight technology help the reduction in fuel consumption and the improvement of the driving dynamic while increasing in passive safety derives from the energy absorption capacity at low stress levels. Furthermore, the driving comfort can be increased by acoustic and thermal

insulation in conjunction with the damping of driving vibrations.

1.3 Sandwich Structures

Sandwich structures are essential machine elements in lightweight construction. In particular, aluminum sandwich construction has been recognised as a promising concept for structural design of lightweight transportation systems such as aircraft [39, 40], high-speed trains [41, 42] and fast ships [43, 44].

The definition of a sandwich structure is a composite where a core material is enclosed by two or more layers. The basic principle of sandwich structures is for two strong face sheets to bear the applied loads whilst the core acts as a spacer which retains the face sheets in position by carrying shear stresses. Therefore, the core must be stiff enough in the direction perpendicular to the faces to ensure that they remain the correct distance apart and exhibit sufficient shear stiffness to ensure that when the panel is bent the faces do not slide over each other. The core material does not need to reach the mechanical performance of the face sheets and typically low density materials are applied [45]. Nowadays, the industrial standard for sandwich cores are honeycomb structures which exhibit excellent stiffness at very low densities. However, the processing of honeycomb structures, especially as a core between curved face sheets, is complex and therefore increases the manufacturing costs. Furthermore, honeycomb structures possess poor resistance to contact and impact loads [46, 47, 48] and exhibit anisotropic properties. Thus there is a necessity for new innovative core materials.

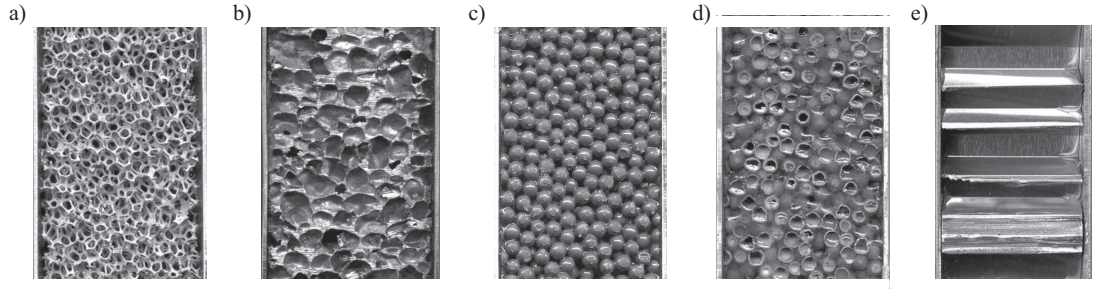

Figure 6: Sandwich structures containing different core materials: a) M-Pore®, b) Alporas®, c) Partially adhesively bonded MHSS, d) Syntactic adhesively bonded MHSS, e) Honeycomb structure.

In Fig. 6 a) a M-Pore® aluminium sponge is used as core material. This commercially available material is characterised by very high porosity and therefore low density ($\rho_c = 0.27$ g/cm^3). Figure 6 b) shows the Alporas® aluminium foam with closed cells and a slightly higher density ($\rho_c = 0.34$ g/cm^3) but also improved mechanical properties. In Figs. 6 c) and d) partial ($\rho_c = 0.3, 0.6$ g/cm^3) and syntactic MHSS

- cores ($\rho_c = 0.75, 1.2$ g/cm^3) are shown. For industrial applications these core materials have to be able to compete with classical honeycomb structures ($\rho_c = 0.09$ g/cm^3, cf. Fig. 6 e)). The benefits of cellular metal as sandwich cores, relative to competing concepts, arise primarily in curved configurations where the isotropy of the material is advantageous [11, 21, 49]. Due to the multi-functional properties of cellular metals the selection of the optimum core material requires the consideration of all characteristics with relevance to the intended application. Furthermore, the potential utilisation in safety relevant fields puts great demands on the predictability and stability of their properties

In the scope of this work, MHSS are analysed under the viewpoint of their application as core material in sandwich panels. Special focus is put on adhesively bonded MHSS. This joining technology allows flexible processing and the adjustment of the properties of the composite by the selection of different adhesives. Numerical and experimental analysis on their mechanical and thermal properties are performed. Furthermore, identical tests are carried out on 'classical' core materials in order to obtain reference values for comparison to clearly show the key features of this innovative material.

1.4 State of the research

Cellular metals

In 1943 Sosnik attempted to produce cellular metal by foaming aluminium using mercury as a foaming agent [50]. A major disadvantage of this process was the toxicity introduced by the use of mercury. This shortcoming was dealt with by Elliot [51] in 1956 who substituted mercury with foaming agents generating gas by thermal decomposition. In the following decades, comprehensive research within the area of cellular metals was conducted. In [8] Banhart gave an extensive overview of the manufacturing techniques used to generate modern cellular metals. Encyclopaedic descriptions of cellular metals, their manufacturing, processing and properties are given in the treatises by Ashby [21] and Degischer [33]. However, despite the intensive research on the manufacturing and properties of cellular metals, the key problem of the scattering of material parameters [27, 28] due to the stochastic geometry of the cellular metals still remained to be solved.

As a promising solution to this problem, the focus shifted on metallic hollow sphere structures. Four main approaches for the manufacturing of single metallic hollow spheres can be identified: The gas atomization process described by Sypeck et al. [52] is restricted to relatively small spheres ($R < 1$ mm) with thick sphere walls (0.1 - 0.3 mm). The main disadvantage of this method is the difficulty of controlling the geometrical dimensions of the hollow spheres. Larger diameters between 1 and 6 mm can be achieved by spraying a metal powder - binder slurry through the outer

orifice of a coaxial nozzle. However, this process, patented by Toribin [53], yields deviations from the spherical shape and strong variations of the sphere wall thickness of the single hollow spheres. Excellent uniformity of the sphere wall thickness can be achieved by galvanic coating of styrofoam spheres as introduced by Jäckel [54]. The disadvantage of this process are high manufacturing costs, in particular for a high sphere wall thickness. A more cost effective alternative was later introduced by Jäckel [29] in which the spheres are coated in a fluidized bed process. In a subsequent sintering process single hollow spheres or sintered hollow sphere bulk material were produced. The work of Studnitzky et al. [31] focused on the problem of carbon control during the debindering of the green bodies in the sintering process.

At the time when the present research commenced, little research on the mechanical properties of MHSS existed. Lim et al. performed experimental analysis on sintered MHSS [55]. Small samples assembled by a maximum of 10 spheres into each direction were tested and a distinct dependence on the sample size was observed. Furthermore, a highly simplified two-dimensional finite element model was used to study deformation mechanisms in single hollow spheres. However, the numerical models gave no information about the mechanical properties of MHSS, where neighboring spheres are interacting during elastic and plastic deformation. A refined finite element approach was performed by Gasser et al. [56] who used a three dimensional model of a sintered MHSS. A face centred cubic arrangement of the spheres was investigated and the elastic properties were numerically determined for the 0^o loading planes (cf. Fig. 7). These analyses were further expanded by Sanders and colleagues [57, 58]. Three dimensional models of sintered MHSS with primitive cubic [57], body centred cubic and face centred cubic [58] arrangement of the spheres were analysed and elastic and plastic properties of these structures were determined. However, these analyses were restricted on sintered structures and tetrahedral finite elements were used for the finite element meshes. This element class shows inferior performance in comparison with hexahedral elements, which preferably should be used within the plastic range [59, 60]. Zhao and colleagues investigated the impact behavior of adhesively bonded nickel hollow spheres structures and sintered iron agglomerates of hollow spheres [61]. Within this experimental analyses, a distinct strain rate dependency of the materials could be observed. To the author's knowledge, no detailed research on the mechanical behavior of adhesively bonded MHSS and the thermal properties of MHSS had been conducted up to this time.

Sandwich structures

The rapid development in aircraft engineering in the 1950's stimulated the research on sandwich construction. This research area is very well documented and comprehensive works on the mechanic properties of sandwich compounds are e.g. [45, 62, 63]. A classical core material for sandwich compounds are honeycomb structures. Though sandwich structures are established in industrial applications, honeycomb structures

are the subject of on-going research. In a recent publication, Paik et al. [39] investigated the strength of aluminium honeycomb structures under varying loading conditions, including three-point bending tests. Recently published literature deals with the use of metallic foams as sandwich cores. A PhD thesis by Bart-Smith [49] addressed the performance of two different aluminium foams in sandwich structures. The bending stiffness of the sandwich compounds was determined in four-point bending tests and the failure modes: face yield, core shear and core indentation were observed. Additional three-point bending tests of Bart-Smith and colleagues aimed for the determination of the bending performance of sandwich construction with thin Alporas® cellular metal cores [64]. Steeves and colleagues conducted research on sandwich structures with polymer foam cores [65, 66]. In the first part of this work, analytic formulas for the prediction of failure loads in three-point bending and guidelines for minimum weight design were derived [65]. Subsequent experimental three-point bending tests by Steeves et al. [66] showed that more improved predictions of failure mechanisms and failure load could be achieved by performing detailed finite element analyses. Deshpande et al. [67] investigated investment cast truss core sandwich beams. Due to the investment cast processing, the core materials had a controlled regular geometriy and three-point bending tests indicated significantly better performance than the competing concept of metallic foam cores with stochastic geometries. In 2004 [68], fabrication protocols based on the sheet forming of trusses and shell elements as well as textile assembly were used to manufacture regular open celled cores for sandwich compounds. It was found that the specific load carrying capacity in three-point bending of these structures outperformed cellular metals with stochastic geometry and was competitive with classical honeycomb structures. Mohan et al. [69] performed four-point bending tests on sandwich structures with Alporas® aluminium foam cores and alumina face sheets. Special focus was given to the dependency of the failure mode on the geometrical dimensions of the sandwich specimen. The experimental results were found to be in good agreement with analytical predictions and results of finite element analyses. Due to the brittle alumina face sheets, the failure mode core sheet fracture could be observed next to the common failure mechanisms: core shear and core indentation. Pollien and colleagues [70] performed three-point bending tests on graded open-cell aluminium foam core sandwich beams. The investigated sandwich cores were assembled by different layers of aluminium foam with varying densities. It was found that although the structures showed poor performance for stiffness-limited design, a potential exists from the standpoint of load-limited design. At the beginning of the research work, described in this thesis, no research work had been conducted on MHSS in sandwich structures.

2 Theoretical Foundation

2.1 Mechanics

In the following, the required continuum mechanics for the understanding of this thesis is summarised. In addition to linear-elastic material behaviour, plasticity is considered. More detailed descriptions of the continuum mechanical basis can be found in the classical textbooks [71, 72, 73].

2.1.1 Linear Elasticity

Based on Hooke's law formulated in 1678 for a uniaxial stress state, the CAUCHY strain tensor ε_{ij} and stress tensor σ_{ij} are linked by the linear transformation

$$\sigma_{ij} = C_{ijkl} \cdot \varepsilon_{ij} \tag{1}$$

which is called CAUCHY-elasticity [71]. The material tensor C_{ijkl} of the elastic constants is of fourth order and consequently contains $3^4 = 81$ components. In the considered case of linear elasticity, all entries of this matrix are constants. Due to its symmetry, the elasticity tensor exhibits only 36 independent variables. Under the presumption of the existence of an elastic potential $w(\varepsilon_{ij})$, the amount of independent components is further reduced to 21. Based on this elastic potential, the stress components of σ_{ij} can be determined by differentiation according to

$$\sigma_{ij} = \frac{\partial w}{\varepsilon_{ij}}. \tag{2}$$

This type of elasticity is known as GREEN-elasticity [71]. Geometric symmetries of the material yield further reduction of the independent variables in the elasticity tensor. A geometry that exhibits three mutually perpendicular symmetry planes is orthotropic symmetric. In this case, the elasticity tensor is defined by 9 independent coefficients

$$\overline{\mathbf{C}}^{\text{orth.}} = \begin{pmatrix} C_{11} & C_{12} & C_{13} & & & \\ & C_{22} & C_{23} & & \varnothing & \\ & & C_{33} & & & \\ & & & C_{44} & & \\ & sym. & & & C_{55} & \\ & & & & & C_{66} \end{pmatrix}. \tag{3}$$

In the scope of this work, the finite element models exhibit cubic symmetries and therefore the equalities $C_{11} = C_{22} = C_{33}$, $C_{12} = C_{13} = C_{23}$ and $C_{44} = C_{55} = C_{55}$ are valid. Consequently, the elastic behaviour can be described based on only three independent elastic parameters C_{11}, C_{12} and C_{44}. Two of these elastic constants can be

expressed in dependence on the elastic parameters YOUNG's modulus E and POISSON's ratio ν:

$$C_{11} = \frac{E \cdot (1-\nu)}{(1+\nu) \cdot (1-2\nu)}, \quad C_{12} = \frac{E \cdot \nu}{(1+\nu) \cdot (1-2\nu)}. \tag{4}$$

The orientation of the applied loads is thereby aligned with the axis of the cubic symmetry planes. The third elastic constant C_{44} can be expressed in dependence on the shear modulus ($C_{44} = 1/G^{45^o}$). This analysis requires the rotation of the loading planes by 45^o about one of the symmetric axis and therefore a second set of finite element models [74]. The orientation of these loading planes is shown in Fig. 7 for a primitive cubic arrangement of circular inclusions.

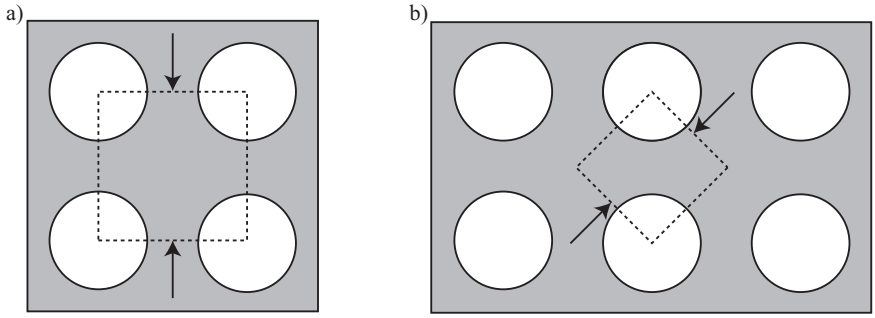

Figure 7: Orientation of the loading planes for primitive cubic topology: a) 0^o-loading planes; b) 45^o-loading planes.

In the case of an isotropic material, a set of two independent material parameters is sufficient to completely characterise the linear-elastic behaviour of a material [75]. Within the field of mechanical engineering, typically the two engineering constants YOUNG's modulus E and POISSON's ratio ν are used. Alternatively, e.g. in soil mechanics, the shear modulus G and bulk modulus K are chosen instead. Simple equations for the transformation of these elastic constants are provided in Table 1.

Shear modulus	Bulk modulus
$G = \frac{E}{2(1+\nu)}$	$K = \frac{E}{3(1-2\nu)}$

Table 1: Transformation of elastic constants for isotropic materials.

2.1.2 Plasticity

The constitutive description of plastic material behaviour comprises the yield condition, the flow rule and the hardening rule. The yield condition determines the onset of plastic yielding. The flow rule describes the evolution of the plastic strain in dependence on all loads that have affected and are currently affecting the material (loading

history). The hardening rule incorporates the effect of material hardening (e.g. strain hardening) on the yield condition and flow rule.

Plastic material behaviour is characterised by plastic strains $\boldsymbol{\varepsilon}_\mathrm{p}$ which remain even after the removal of all loads. In contrast, elastic strains $\boldsymbol{\varepsilon}_\mathrm{el}$ vanish after unloading. The constraint on small strains enables the additive composition of the total strain tensor $\boldsymbol{\varepsilon}$ according to

$$\boldsymbol{\varepsilon} = \boldsymbol{\varepsilon}_\mathrm{el} + \boldsymbol{\varepsilon}_\mathrm{p}. \tag{5}$$

After the substitution of $\boldsymbol{\varepsilon}$ by $\boldsymbol{\varepsilon}_\mathrm{el}$ in Eq. (1), the elastic strains can be determined. However, in the case of plastic strains $\boldsymbol{\varepsilon}_\mathrm{p}$ no linear relation between the stresses and strains can be formulated. The plastic strains are dependent on the loading history and therefore rate equations or, in the case of time independent plasticity, incremental relations must be applied. The incremental plastic strains $\mathrm{d}\boldsymbol{\varepsilon}_\mathrm{p}$ can then be integrated over the loading history in order to obtain $\boldsymbol{\varepsilon}_\mathrm{p}$. Equation (5) can be rewritten as the additive composition of the strain increments:

$$\mathrm{d}\boldsymbol{\varepsilon} = \mathrm{d}\boldsymbol{\varepsilon}_\mathrm{el} + \mathrm{d}\boldsymbol{\varepsilon}_\mathrm{p}. \tag{6}$$

Yield condition In the case of a uniaxial stress state, the onset of the plastic yield is related to the uniaxial yield stress. For multi-axial stress states, a yield condition is applied which first transforms the stress tensor σ_{ij} into an equivalent scalar and then relates this value to an experimental uniaxial value. In the general formulation the yield condition F[1]: $\mathbb{R}^6 \times \mathbb{R}^{\dim(q_{ij})} \rightarrow \mathbb{R}$ can be expressed in dependence on the stress tensor σ_{ij} and the hardening tensor q_{ij} as

$$F = F(\sigma_{ij}, q_{ij}). \tag{7}$$

Under the assumption of ideal plasticity, the hardening tensor q_{ij} is equal zero and the yield condition $F(\sigma_{ij})$: $\mathbb{R}^6 \rightarrow \mathbb{R}$ is only dependent on the stresses. If this yield condition can be split into a stress fraction $f(\sigma_{ij})$ and an experimental material parameter k, then f is the designated yield criteria

$$F(\sigma_{ij}) = f(\sigma_{ij}) - k. \tag{8}$$

The physical interpretations of the values for F are

$F(\sigma_{ij}) < 0$	pure elastic material behaviour,
$F(\sigma_{ij}) = 0$	plastic material behaviour,
$F(\sigma_{ij}) > 0$	not defined for time independent plasticity.

[1] Only six components of the stress tensor are independent due to symmetry.

The yield condition $F(\sigma_{ij}) = 0$ represents a closed hypersurface in a n-dimensional stress space. A direct graphical representation of this yield surface is generally not possible. However, a reduction of its dimensionality can be achieved by a principal axis transformation of σ_{ij}. The components of the stress tensor are then reduced to the principal stresses σ_I, σ_{II} and σ_{III}. In the principal stress space it is possible to visualise the yield condition as a three-dimensional surface. This principal stress state is shown in Fig 8. Inside the principal stress space, hydrostatic stress states lie on the space diagonal which is therefore called as the hydrostatic axis. Any plane perpendicular to the hydrostatic axis is called an octahedral plane. The particular octahedral plane passing through the origin is the deviatoric plane or π-plane [72]. The position of an arbitrary stress point P inside the principal stress space can be expressed based on its three basic invariants $P(\frac{1}{\sqrt{3}}J_1^{\circ},\ \sqrt{2J_2'}, \Theta(J_2', J_3'))$ [76].

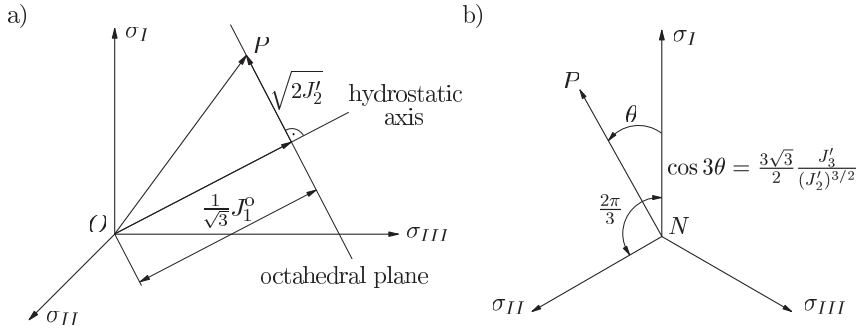

Figure 8: Principal stress space.

The components σ_{ij} of the stress tensor are dependent on the particular coordinate system. In order to obtain a coordinate-system-independent representation of the yield condition it can be formulated in dependence on the invariants of the stress tensor (see also Appendix D).

$$F = F(J_1^{\circ}, J_2', J_3'). \tag{9}$$

On the basis of the dependency of the yield condition on the invariants, a descriptive classification can be performed. Yield conditions independent of the hydrostatic stress can be represented by the invariants J_2' and J_3'. Stress states with $J_2' = const.$ lie on a circle around the hydrostatic axis in an octahedral plane. The yield surface forms a prismatic body whose longitudinal axis is represented by the hydrostatic axis. A dependency of the yield condition on J_3' results in deviation from the circular shape. A dependency on J_1° becomes visible as a change in size of the cross-section of the yield surface in different deviator planes. However, the shape of the cross-section remains similar in mathematical sense. Therefore, a dependency on J_1° can be represented by subsectional views through planes along the hydrostatic axis.

Von Mises Yield condition The VON MISES yield condition is often applied in order to describe the plastic behaviour of ductile metallic materials. This yield condition presumes that the yield condition is only dependent on the deviatoric stress state and therefore not influenced by the hydrostatic stress J_1°. The yield condition can therefore be formulated in dependence on the second invariant J_2' only:

$$F(J_2') = \sqrt{3J_2'} - k_{\mathrm{t}}. \tag{10}$$

The graphical representation of the yield surface in the principal stress space is given in Fig. 9. The yield condition describes a cylindrical surface with a radius of $\sqrt{2/3} \cdot k_{\mathrm{t}}$ in relation to the hydrostatic axis.

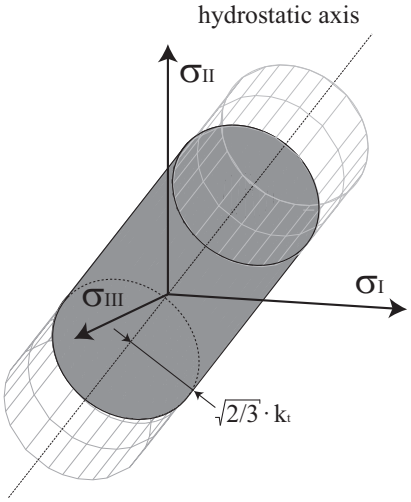

Figure 9: VON MISES yield condition.

Modified Von Mises Yield condition The description of the anisotropic plastic behaviour of a material in the tensile and compressive regime can be achieved by means of a modified VON MISES yield criterion [77] where the yield strength is dependent on the algebraic sign of the hydrostatic stress state. Figure 10 illustrates the yield surface of this criterion in the principal stress space. In order to relate arbitrary stress states to uniaxial material parameters (i.e. tensile k_{t} and compressive k_{c} flow strength), the effective VON MISES stress $\sigma_{\mathrm{eff}} = \sqrt{3J_2'}$ is determined (cf. Eq. (10)). It should be mentioned here that the modified VON MISES criterion introduces potential problems for stress states where the hydrostatic stress is equal (e.g. pure shear stress) or close to zero and the yield strength discontinuously changes between two values.

Examples for further yield conditions are DUCKER-PAGER [78] which is often applied in the field of soil mechanics or the five parameter model according to WILLAM-WARNKE [79] for concrete.

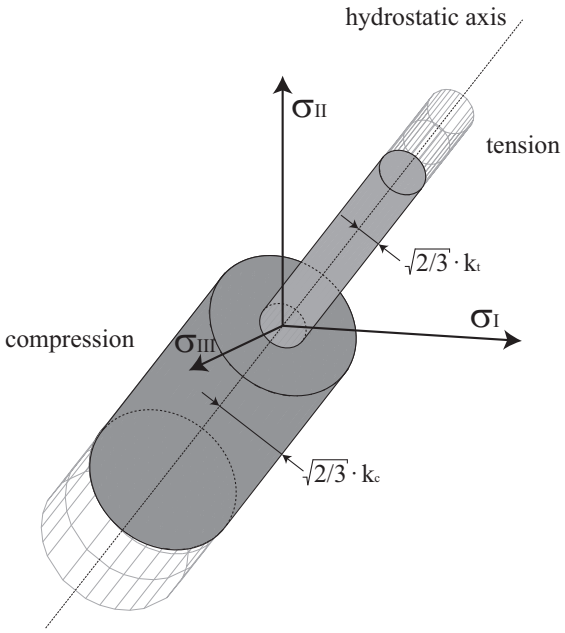

Figure 10: Modified VON MISES yield condition.

Flow Rule The flow rule describes the evolution of the infinitesimal increments of the plastic strains $\mathrm{d}\boldsymbol{\varepsilon}_\mathrm{p}$. The most general ansatz for the flow rule is [80]

$$\mathrm{d}\varepsilon_{\mathrm{p},ij} = \mathrm{d}\lambda \cdot r_{ij}(\sigma_{ij}, q_{ij}), \tag{11}$$

where the vector function $r_{ij}(\sigma_{ij}, q_{ij})$ determines the direction and the coefficient $\mathrm{d}\lambda$ the length of the plasticity vector $\mathrm{d}\varepsilon_{\mathrm{p},ij}$. The variable $\mathrm{d}\lambda$ is denoted as a consistency parameter and has to comply with the inequality $\mathrm{d}\lambda > 0$. The equality $\mathrm{d}\lambda = 0$ is only feasible for $\mathrm{d}\varepsilon_{\mathrm{p},ij} = 0$. Based on *Ducker*'s stability postulate [81] the following flow rule can be derived:

$$\mathrm{d}\varepsilon_{\mathrm{p},ij} = \mathrm{d}\lambda \cdot \frac{\partial F(\sigma_{ij}, q_{ij})}{\partial \sigma_{ij}}. \tag{12}$$

According to Eq. (12) the vector $\mathrm{d}\varepsilon_{\mathrm{p},ij}$ is oriented perpendicular to the yield surface and pointing in the outside direction ($\mathrm{d}\lambda > 0$). A flow rule of this type fulfills the normality rule and is called the associated flow rule. In the case of the VON MISES yield condition the flow rule (11) yields:

$$\mathrm{d}\varepsilon_{\mathrm{p},ij} = \mathrm{d}\lambda \cdot \frac{\sqrt{3}}{2 \cdot J_2'} s_{ij}, \tag{13}$$

with s_{ij} representing the deviatoric stress tensor. In the case of the modified VON MISES yield condition the flow rule is identical to Eq. (13), since the orientation of the normal vector is similar and only the radius relative to the hydrostatic axis varies (cf. Fig. 10).

Analogous to the effective stress σ_{eff}, an equivalent plastic strain $\varepsilon_{\text{eff}}^{\text{pl}}$ is defined. The incremental specific plastic work $\mathrm{d}w_{\text{p}}$ can be calculated by multiplication of the stress σ_{ij} and strain tensors $\mathrm{d}\varepsilon_{\text{pl},ij}$ or by the product of the effective values σ_{eff} and $\mathrm{d}\varepsilon_{\text{eff}}^{\text{pl}}$. Thereby, both products must yield the same result:

$$\mathrm{d}w_{\text{p}} = \sigma_{ij}\ \mathrm{d}\varepsilon_{\text{pl},ij} \stackrel{!}{=} \sigma_{\text{eff}} \cdot \mathrm{d}\varepsilon_{\text{eff}}^{\text{pl}} \tag{14}$$

Accordingly, the equivalent plastic strain is given by

$$\mathrm{d}\varepsilon_{\text{eff}}^{\text{pl}} = \frac{\sigma_{ij}\ \mathrm{d}\varepsilon_{\text{pl},ij}}{\sigma_{\text{eff}}}. \tag{15}$$

In the particular case of the VON MISES yield condition, the effective stress is $\sigma_{\text{eff}} = \sqrt{3J_2'}$ and the equivalent plastic strain is defined as [76]

$$\mathrm{d}\varepsilon_{\text{eff}}^{\text{pl}} = \frac{2}{3} \cdot \sqrt{\mathrm{d}\varepsilon_{\text{pl},ij}\ \mathrm{d}\varepsilon_{\text{pl},ij}}. \tag{16}$$

Hardening Rule So far, it was assumed that the yield condition is only dependent on the stresses. In the following, the influence of hardening is discussed. Two types of hardening, namely isotropic and kinematic hardening can be distinguished. Isotropic hardening corresponds to a uniform expansion of the yield surface in the principal stress space. The position of the axis of the yield surface (e.g. the hydrostatic axis for VON MISES) remains constant. The mathematical description of isotropic hardening is achieved by the introduction of the hardening variable κ:

$$F = f(\sigma_{ij}) - k(\kappa) = 0. \tag{17}$$

In the case of kinematic hardening, the size and shape of the yield surface remains constant and only its position inside the principal stress space is altered.

$$F = f(\sigma_{ij} - \alpha_{ij}) - k = 0 \tag{18}$$

In the scope of this analysis only ideal plasticity will be considered and therefore the phenomenon of hardening be disregarded.

Strain Rate Dependency High strain rates $\dot{\varepsilon}$ influence the plastic material response. For most materials, an increase of strain rate raises the yield stress ($m > 0$, cf. Fig. 11). The dependency of the material response on the strain rate is usually quantified with the strain-rate sensitivity m:

$$m = \frac{\ln\left(\frac{\sigma_2}{\sigma_1}\right)}{\ln\left(\frac{\dot{\varepsilon}_2}{\dot{\varepsilon}_2}\right)}, \tag{19}$$

where the σ_1 and σ_2 are the stresses at the corresponding strain rates $\dot{\varepsilon}_1$ and $\dot{\varepsilon}_2$. For many materials, the effect of the strain rate on the yield stress at a fixed strain and temperature can be described by a dependence on the strain-rate sensitivity by a power-law expression

$$\sigma = D \cdot \varepsilon^m, \tag{20}$$

where m is the strain rate sensitivity and D a material parameter. At moderate loading rates often the COWPER SYMOND relationship [82] is used

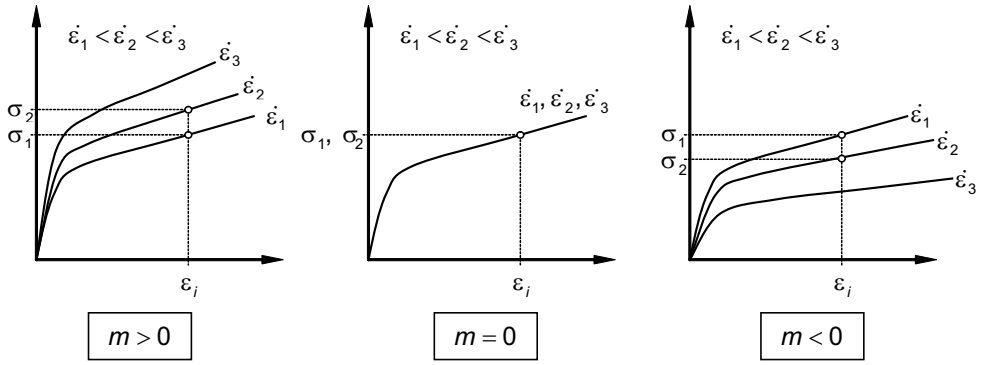

Figure 11: Material strain rate sensitivity.

$$k_{\text{dye}} = k \left[1 + \left(\frac{\dot{\varepsilon}}{C} \right)^{\frac{1}{p}} \right], \tag{21}$$

where k_{dye} is the dynamic yield stress and k denotes the static yield stress. The coefficients C and p are the COWPER SYMOND strain rate parameters. Typical values for these parameters are shown in Table 2. The COWPER SYMOND relationship [77, 83, 84] can be included in elasto-plastic response by simply modifying the yield stress.

Material	C	p
Mild steel	40.4 s^{-1}	5
Aluminium alloy	6500 s^{-1}	4
Epoxy resin	1050 s^{-1}	3.7

Table 2: Cowper Symond's strain rate parameters for selected materials [82].

It should be noted that the strain-rate sensitivity is also temperature dependent [85] and typically increases with temperature.

The effect of strong strain-rate dependency of cellular metals has already been observed by Hornwort et al. [86], by studying mechanical properties of closed-cell structures at strain rates up to 2 s^{-1}. It was found that cellular materials have a

significantly different stress-strain relationship at higher strain-rates without the characteristic plateau stress.

2.2 Heat transfer

In this thesis, numerical simulations of the heat transfer properties of MHSS are compared to experimental results. The heat transfer is defined as energy in transit due to a temperature difference [87]. As shown in Fig. 12, heat transfer is brought about due to three different mechanisms: thermal radiation $\dot{Q}_{\text{rad}}$, thermal convection $\dot{Q}_{\text{conv}}$ and thermal conduction $\dot{Q}_{\text{cond}}$.

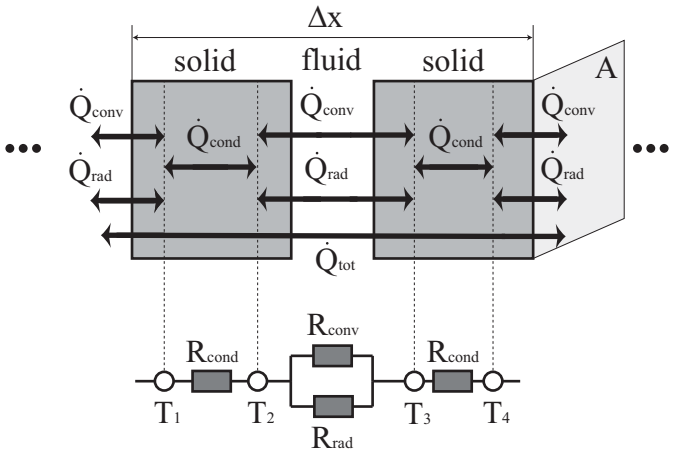

Figure 12: Principles of heat transfer.

Heat transfer can be studied in more detail by making use of an analogy to electrical circuits in which a thermal circuit is made up of thermal resistances R_i. Thus the total heat flux $\dot{Q}_{\text{tot}}$ can be obtained in terms of the outer temperatures T_1 and T_4 as long as the effective thermal conductivity λ_{eff} of the system is known:

$$\lambda_{\text{eff}} = \frac{\dot{Q}_{\text{tot}}}{A} \cdot \frac{\Delta x}{T_4 - T_1}, \tag{22}$$

where A is the area of the control surfaces and Δx the distance between these surfaces. The effective thermal conductivity can be obtained under the consideration of all relevant heat transfer mechanisms of the thermal system. If an analytical solution exists, λ_{eff} is calculated based on the thermal resistances R_i. The determination of this material parameter making use of finite element analysis is described in Section 3.1.3.

2.2.1 Thermal conduction

The principal physical mechanism of thermal conduction in gases and liquids is the molecular exchange of kinetic energy due to random collisions. Thermal conduction in

solids is based on lattice vibration and transport of free electrons. Therefore, good solid thermal conductors enable large numbers of free electrons to move from high to low temperature regions and thereby enhancing the transport of thermal energy. Energy can also be transmitted as vibrational energy in lattice structures by so called lattice waves (Phonons) [87]. The conduction of thermal energy is described by Fourier's law

$$\dot{Q}_{\text{cond}} = -\lambda \cdot A \frac{\Delta T}{\Delta x}. \tag{23}$$

The material parameter λ is termed the thermal conductivity.

2.2.2 Thermal convection

Convection heat transfer describes the heat transfer between a solid body and a moving fluid. Two types of thermal convection, namely free and forced convection, can be distinguished. In the case of free convection, the movement of the fluid is experienced as a result of a density gradient near the surface. The concept of forced convection is used if there is an inherent movement of the fluid that is generated by an external source (e.g. a fan).

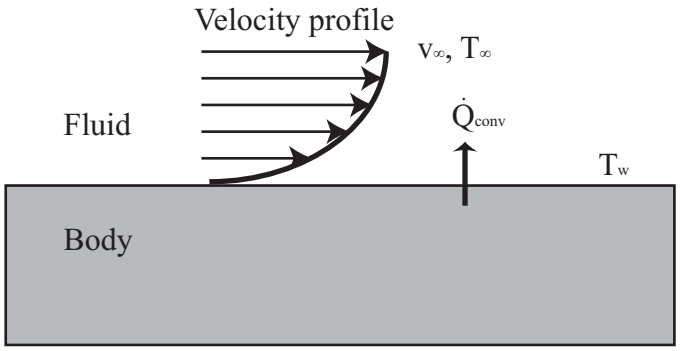

Figure 13: Principle of thermal convection.

Figure 13 shows the velocity profile of a fluid moving in the vicinity of a stationary solid body. As the fluid gets closer to the solid body its velocity drops to zero as a result of viscous friction. At the fluid/solid interface the thermal energy is transferred by thermal conduction (film conductance). Inside the fluid however, the thermal energy is transported by thermal conduction in conjunction with the bulk movement of the fluid. This thermal convective energy is described by Newton's law of cooling [88]

$$\dot{Q}_{\text{conv}} = h \cdot A(T_s - T_\infty), \tag{24}$$

where T_s is the surface temperature, T_∞ is the temperature of the fluid far away from the surface, A is the contact area of solid and liquid and h is the convection heat transfer coefficient. For simple systems, h can be calculated analytically. However,

complex systems often require empirical models derived from experimental studies or detailed numerical simulations.

2.2.3 Thermal radiation

The terminology 'thermal radiation' refers to electromagnetic radiation emitted from the surface of an object. Thermal radiation is generated by the transformation of kinetic energy due to random molecular movement (BROWNIAN motion) into electromagnetic radiation. The frequency distribution of the emitted thermal radiation is a probability distribution depending only on the temperature. Thermal radiation causes thermal energy exchange between objects, since the emitted energy increases with the temperature ($\sim T^4$). The thermal radiation properties of a body are described by the following equation [88]

$$\alpha + \beta + \gamma = 1, \tag{25}$$

where α represents the absorption factor, β is the reflection factor and γ is the transmission factor. The absorption factor is equal to the emissivity ϵ. Most solid bodies do not transmit thermal radiation ($\gamma = 0$) and in order to simplify thermal radiation analysis, objects are often considered as black bodies where the reflection factor is also presumed to be zero ($\beta = 0$). Thus, a black body is a perfect emitter and absorber and the following relation holds

$$\alpha = \epsilon = 1 \tag{26}$$

The thermal radiation power of a black body is given by

$$\dot{q}_{\text{rad}}(f, T) = \frac{2 \cdot h \cdot f^3}{c^2} \cdot \frac{1}{e^{\frac{hf}{k_B T}} - 1}, \tag{27}$$

where c is the speed of light, h is Planck's constant, k_B is the Boltzmann constant, f the frequency and T the temperature of the body. Integration of Eq. (27) over all frequencies yields the Stefan-Boltzmann law [88]

$$\dot{Q}_{\text{rad}} = \sigma \cdot A \cdot T^4 \tag{28}$$

with the BOLTZMANN constant σ and the surface area A.

3 Methodology

3.1 Finite Element Method

The aim of these numerical analyses is to investigate the behaviour of MHSS with complex geometries subjected to non-linear material behaviour (plasticity). Classical analytical mechanics is restricted to the solution of simplified models. Therefore, complex problems have to be simplified and the validity of the obtained results for the considered problems is not guaranteed. The finite element method is a tool which is ideally suited to the non-linear analysis of complex geometries. The origins of the finite element method (FEM) date back to Clough and emerged about 1960 [89]. The approach flourished due to the rapid evolution of computer technology and finite element methods are now well established as standard tools for industrial applications.

3.1.1 Mathematics

The basic idea of the finite element method is the decomposition of a domain with a complicated geometry into geometrically simple sub-domains, such that the governing differential equation can be solved (approximately) for these finite elements. The single element solutions are then assembled to obtain the complete system solution with the appropriate boundary conditions. The assembly process uses appropriate balance equations at the nodes which can then be used to define the elements and serve also as connection points between the elements. In the following section, the governing differential equations will be transformed to the principal finite element equation that is used to model elasto-statics. An analogous approach based on the partial differential equation of heat conduction can be applied for the derivation of the governing finite element equation in conductive heat transfer.

Elasto-Statics The continuum mechanical modelling (cf. Fig. 14) of elasto-statics requires three components: the material law, the kinematic compatibility condition and the equilibrium condition. These three components have to be linked in order to obtain the governing differential equation.

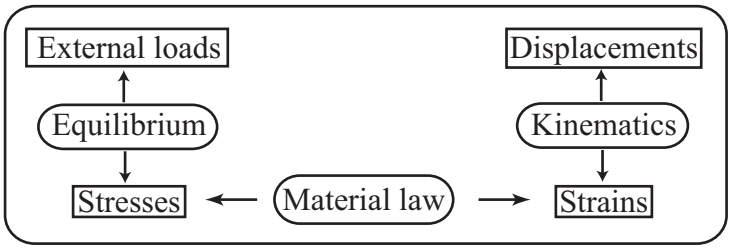

Figure 14: Continuum mechanical modelling.

For the simplest case of elasto-statics, the material law is given by HOOKE's law (1). The incorporation of plastic material behaviour can be achieved by determining the elasto-plastic material matrix [89]. The kinematic compatibility condition can be formulated based on the well-known equations for the strains and angles depending on the displacements

$$\begin{array}{lll} \varepsilon_x = \frac{\delta u}{\delta x}, & \varepsilon_y = \frac{\delta v}{\delta y}, & \varepsilon_z = \frac{\delta w}{\delta z}, \\ \gamma_{xy} = \frac{\delta v}{\delta x} + \frac{\delta u}{\delta y}, & \gamma_{yz} = \frac{\delta w}{\delta y} + \frac{\delta v}{\delta z}, & \gamma_{zx} = \frac{\delta u}{\delta z} + \frac{\delta w}{\delta x} \end{array} \tag{29}$$

and be rewritten in the form of a matrix equation[2]

$$\boldsymbol{\varepsilon} = \begin{pmatrix} \varepsilon_x \\ \varepsilon_y \\ \varepsilon_z \\ \gamma_{xy} \\ \gamma_{yz} \\ \gamma_{zx} \end{pmatrix} = \begin{bmatrix} \frac{\partial}{\partial x} & 0 & 0 \\ 0 & \frac{\partial}{\partial y} & 0 \\ 0 & 0 & \frac{\partial}{\partial z} \\ \frac{\partial}{\partial y} & \frac{\partial}{\partial x} & 0 \\ 0 & \frac{\partial}{\partial z} & \frac{\partial}{\partial y} \\ \frac{\partial}{\partial z} & 0 & \frac{\partial}{\partial x} \end{bmatrix} \cdot \begin{pmatrix} u \\ v \\ w \end{pmatrix} = \overline{\boldsymbol{D}} \cdot \boldsymbol{u}. \tag{30}$$

The matrix $\overline{\boldsymbol{D}}$ is a differential operator matrix which relates the displacements to the strains. The last element of the continuum mechanical modelling is the equilibrium condition which is shown in Fig. 15 for a volume element in x-direction. The

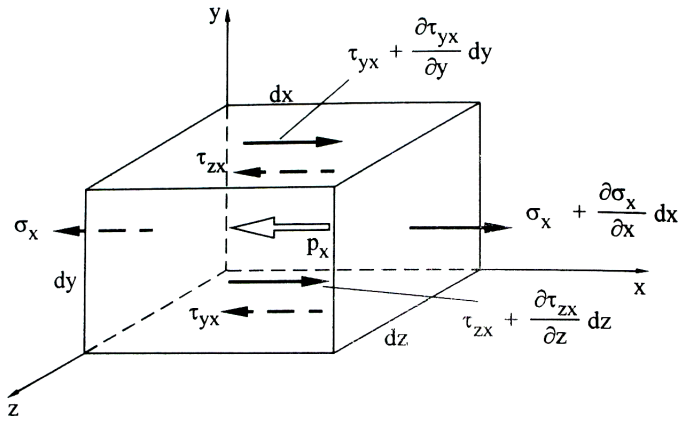

Figure 15: Equilibrium condition of a volume element in x-direction [89].

evaluation of all force equilibriums in x, y and z-direction enables the formulation of the equilibrium condition according to

[2]The nine dependent compounds of the strain ε_{ij} and stress σ_{ij} tensors are assembled in a vector ($\boldsymbol{\varepsilon}$ or $\boldsymbol{\sigma}$) comprising only six independent variables.

$$\left[\begin{array}{ccc|ccc} \frac{\partial}{\partial x} & 0 & 0 & \frac{\partial}{\partial y} & 0 & \frac{\partial}{\partial z} \\ 0 & \frac{\partial}{\partial y} & 0 & \frac{\partial}{\partial x} & \frac{\partial}{\partial z} & 0 \\ 0 & 0 & \frac{\partial}{\partial z} & 0 & \frac{\partial}{\partial y} & \frac{\partial}{\partial x} \end{array}\right] \cdot \left(\begin{array}{c} \sigma_x \\ \sigma_y \\ \sigma_z \\ \hline \tau_{xy} \\ \tau_{yz} \\ \tau_{zx} \end{array}\right) = \left(\begin{array}{c} p_x \\ p_y \\ p_z \end{array}\right). \tag{31}$$

The first term in Eq. (31) corresponds to the transposed differential operator matrix $\overline{\boldsymbol{D}}^{\mathrm{T}}$ and this differential equation can be reformulated as

$$\overline{\boldsymbol{D}}^{\mathrm{T}} \cdot \boldsymbol{\sigma} = \boldsymbol{p} \tag{32}$$

The components p_i of the vector $\boldsymbol{p}$ are the body forces per unit volume.

Calculus of variations The differential equation (32) connects the external loads $\boldsymbol{p}$ and the inner stresses $\boldsymbol{\sigma}$. The exact solution of this equation cannot generally be achieved. Instead, different approximation techniques like Galerkin principles or variational principles are applied. Both of the named approaches yield the same result and accordingly only the variational principle will be further elucidated. Therefore, the expression of the virtual work is required. Two types, namely the internal δW_{i} and external virtual work δW_{e} are distinguished. The external virtual work is defined by external loads and their virtual displacements. A virtual displacement denotes a small displacement which is in agreement with all kinematic constraints. External loads comprise singular loads $\boldsymbol{F}$, area loads $\boldsymbol{q}$ and volume loads $\boldsymbol{p}$. In conjunction with the kinematic constraints $\boldsymbol{u}$, the general form of the external virtual work can be written as

$$\delta W_{\mathrm{e}} = \delta \boldsymbol{u}^{\mathrm{T}} \cdot \boldsymbol{F} + \int_V \delta \boldsymbol{u}^{\mathrm{T}} \cdot \boldsymbol{p} \mathrm{d}V + \int_O \delta \boldsymbol{u}^{\mathrm{T}} \cdot \boldsymbol{q} \mathrm{d}O, \tag{33}$$

where the integral $\int_O$ symbolises the integration over the surface and $\int_V$ indicates the integration over the volume of the considered domain. The internal virtual work is obtained by the volume integration of the product of stresses and virtual strains

$$\delta W_{\mathrm{i}} = \int_V \delta \boldsymbol{\varepsilon}^{\mathrm{T}} \cdot \boldsymbol{\sigma} \mathrm{d}V. \tag{34}$$

Next, an alternative equilibrium condition (cf. Eq. (31)) is introduced. An elastic body is in equilibrium with external loads, if the external virtual work is equal to its internal virtual work:

$$\delta W_{\mathrm{e}} = \delta W_{\mathrm{i}}. \tag{35}$$

After merging Eqs. (33),(34) and (35), the following expression can be expanded

$$\int_V \delta\boldsymbol{\varepsilon}^{\mathrm{T}} \cdot \boldsymbol{\sigma} \mathrm{d}V = \delta\boldsymbol{u}^{\mathrm{T}} \cdot \boldsymbol{F} + \int_V \delta\boldsymbol{u}^{\mathrm{T}} \cdot \boldsymbol{p} \mathrm{d}V + \int_O \delta\boldsymbol{u}^{\mathrm{T}} \cdot \boldsymbol{q} \mathrm{d}O. \tag{36}$$

The incorporation of HOOKE's law (1) and the kinematic compatibility condition (30) finally yields

$$\int_V \delta\boldsymbol{u}^{\mathrm{T}} \cdot \overline{\boldsymbol{D}}^{\mathrm{T}} \cdot \overline{\boldsymbol{C}} \cdot \overline{\boldsymbol{D}} \mathrm{d}V \cdot \boldsymbol{u} = \delta\boldsymbol{u}^{\mathrm{T}} \cdot \boldsymbol{F} + \int_V \delta\boldsymbol{u}^{\mathrm{T}} \cdot \boldsymbol{p} \mathrm{d}V + \int_O \delta\boldsymbol{u}^{\mathrm{T}} \cdot \boldsymbol{q} \mathrm{d}O. \tag{37}$$

If $\boldsymbol{u}$ represents the real displacements, Eq. (37) provides the exact solution. However, this equation cannot generally be solved. The real continuum displacement vector $\boldsymbol{u}$ is replaced by an approximate solution within a single element which is denoted in the following as $\boldsymbol{u}_0$. This approximation is composed of so-called shaped-functions which define the distribution of the displacement components within an element and its nodal displacement values as:

$$\boldsymbol{u}_0 = \overline{\boldsymbol{G}} \cdot \boldsymbol{d}. \tag{38}$$

Matrix $\overline{\boldsymbol{G}}$ contains the shape functions and links the nodal displacements $\boldsymbol{d}$ with the displacement distribution within an element. The matrix $\overline{\boldsymbol{G}}$ is assembled by polynomial functions which can easily be integrated or differentiated.

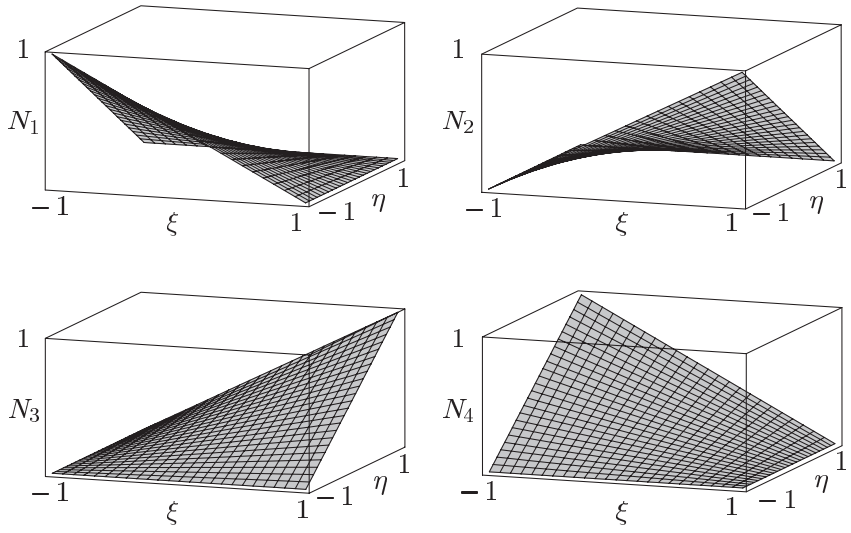

Figure 16: Linear shape functions for a plane element.

Figure 16 shows the linear shape functions for a plane element in the $\xi\eta$-space which is also named unit space. To this end, the coordinates (x, y) are transformed to the unit space where each coordinate ranges from -1 to 1. In the linear two dimensional case, the matrix $\overline{\boldsymbol{G}}$ of shape functions results as

$$\overline{\boldsymbol{G}}^T = \{1 \quad \xi \quad \eta \quad \xi\eta\}\frac{1}{4}\begin{bmatrix} 1 & 1 & 1 & 1 \\ -1 & 1 & 1 & -1 \\ -1 & -1 & 1 & 1 \\ 1 & -1 & 1 & -1 \end{bmatrix} = \{N_1 \quad N_2 \quad N_3 \quad N_4\}. \tag{39}$$

One may note that each N_i $(i = 1, 2, 3, 4)$ is unity when ξ and η assume the coordinates of node i, but zero when ξ and η assume the coordinates of any other node.

The substitution of the real displacement vector $\boldsymbol{u}$ by the approximate solution $\boldsymbol{u}_0$ (discretisation) enables the solution of the continuum mechanical problem. However, the governing differential equation is only solved for the nodes and errors due to the discretisation, numerical approximation techniques, etc. are introduced. The shape functions are utilised to extrapolate the singular nodal solutions over the whole domain.

Under the application of the calculus of variations Eq. (38) is transformed to

$$\delta\boldsymbol{u}^{\mathrm{T}} = \delta\boldsymbol{d}^{\mathrm{T}} \cdot \overline{\boldsymbol{G}}^{\mathrm{T}} \tag{40}$$

and relation (37) can be reformulated according to

$$\int_V (\overline{\boldsymbol{D}} \cdot \overline{\boldsymbol{G}})^{\mathrm{T}} \cdot \overline{\boldsymbol{C}} \cdot \overline{(\boldsymbol{D}} \cdot \overline{\boldsymbol{G}})\mathrm{d}V\,\boldsymbol{d} = \overline{\boldsymbol{G}}^{\mathrm{T}} \cdot \boldsymbol{F} + \int_V \overline{\boldsymbol{G}}^{\mathrm{T}} \cdot \boldsymbol{p}\mathrm{d}V + \int_O \overline{\boldsymbol{G}}^{\mathrm{T}} \cdot \boldsymbol{q}\mathrm{d}O. \tag{41}$$

The left side of this equation contains the product of stiffness and displacements. The right side of the relation is composed of the external loads. Accordingly, Eq. (41) can be simplified as

$$\overline{\boldsymbol{k}} \cdot \boldsymbol{d} = \hat{\boldsymbol{p}}. \tag{42}$$

Equation (42) is the governing equation of the finite element method (e.g. [90]) and relates the nodal displacements $\boldsymbol{d}$ vector over the stiffness matrix $\overline{\boldsymbol{k}}$ to the external loads $\hat{\boldsymbol{p}}$. The stiffness matrix is defined as

$$\overline{\boldsymbol{k}} = \int_V (\overline{\boldsymbol{D}} \cdot \overline{\boldsymbol{G}})^{\mathrm{T}} \cdot \overline{\boldsymbol{C}} \cdot \overline{(\boldsymbol{D}} \cdot \overline{\boldsymbol{G}})\mathrm{d}V. \tag{43}$$

The solution of the linear system of equations (42) is obtained with a so-called solver in which algorithms such as the Cholesky elimination algorithm or multifrontal sparse algorithms are used.

The transition from the real displacements $\boldsymbol{u}$ to the nodal displacements $\boldsymbol{d}$ requires the discretisation of the continuous domain. Therefore, nodes are introduced which represent the geometry. These nodes are related to the finite elements where one node can also be assigned to more than one element. Therewith, the connectivity of the

elements is defined. An agglomeration of finite elements is called a finite element mesh. Examples for finite element meshes are given in Section 3.1.3.

3.1.2 Geometry

The numerical investigation of MHSS presumes the knowledge of its geometric dimensions. Therefore, measurements on experimental samples are performed. Figure 17 shows an example of a partial MHSS including the determined dimensions. The averaged value of the outer sphere diameter R is 1.5 mm, the minimum distance $d_{\min}$ between two neighboring spheres is 0.36 mm and the sphere wall thickness t is 0.075 mm.

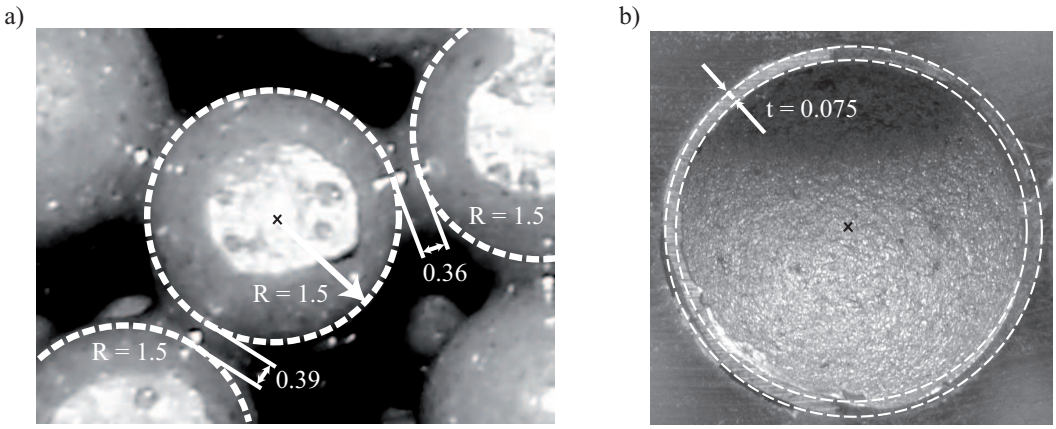

Figure 17: Geometric dimensions of MHSS: a) Outer radius R and minimum distance $d_{\min}$; b) Sphere wall thickness t.

Based on these measurements, volumetric finite element models are generated. Two different morphologies are considered. Figure 18 shows a syntactic and a partial MHSS. The dark grey spherical shells are connected by a light grey matrix which completely embeds the spheres (syntactic, cf. Fig. 18 a)) or is only concentrated in proximity to their contact points (partial, cf. Fig. 18 b)). The experimental samples are manufactured by pouring the hollow spheres in bulk into a mould and therefore exhibit essentially a random arrangement (cf. Fig. 17). The best approach would be a finite element model of such a random structure which comprises the entire specimen and thus, to generate a model without simplifications with respect to the geometry. However, in order to obtain significant results for the macroscopic behaviour of metallic hollow sphere structures, it is sufficient to model a *representative* volume. This volume has to include approximately 10 to 15 spheres in each direction [55]. The required refinement of the mesh in conjunction with its dimensions would yield a huge number of unknowns which would exceed the capacity of the available computer hardware. Therefore, a cubic symmetry of the arrangement of the spheres is assumed. This

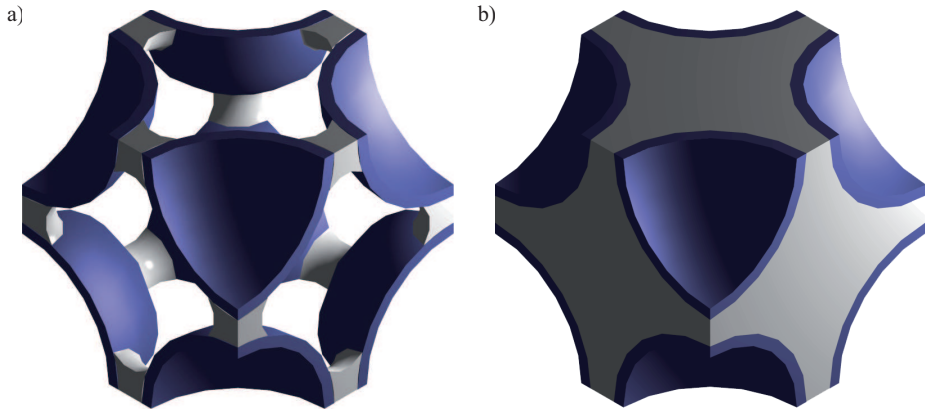

Figure 18: Morphologies of primitive cubic MHSS: a) Partial, b) Syntactic.

approach allows for the utilisation of symmetry boundary conditions and a distinct reduction of the required mesh size. The considered cubic symmetric arrangements of spheres, in the following also designated topologies, are shown in Fig. 19.

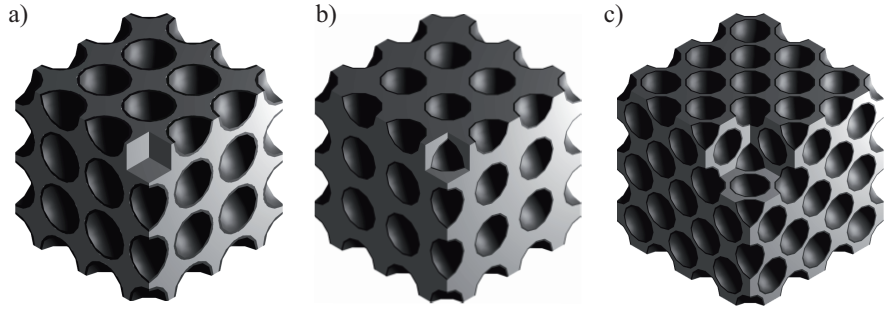

Figure 19: Topologies of syntactic MHSS: a) Primitive cubic, b) Body centred cubic, c) Face centred cubic.

In the field of lightweight construction, the average density $\overline{\rho}$ of MHSS is of great importance. This material parameter depends on the inner diameter r, the topology and the morphology. The minimum distance $d_{\min}$ between two neighboring spheres is 0.36 mm and the outer radius R of a sphere is 1.5 mm (cf. Fig. 17). Consequently, the side lengths l_s of a unit cell are

$$l_s = \begin{cases} 2 \cdot R + d_{\min} = 3.36 \text{ mm} & \text{(primitive cubic)} \\ (4 \cdot R + 2 \cdot d_{\min})/\sqrt{3} = 3.88 \text{ mm} & \text{(body centred cubic)} \\ (4 \cdot R + 2 \cdot d_{\min})/\sqrt{2} = 4.75 \text{ mm} & \text{(face centred cubic)} \end{cases} . \tag{44}$$

The volumes of the unit cell can be calculated according to $V_{\mathrm{U}} = l_s^3$ and the volumes

of the matrix of syntactic MHSS are

$$V_{\mathrm{M}} = V_{\mathrm{U}} - \begin{cases} 4/3 \cdot \pi R^3 = 23.80 \text{ mm}^3 & \text{(primitive cubic)} \\ 8/3 \cdot \pi R^3 = 30.10 \text{ mm}^3 & \text{(body centred cubic)} \\ 16/3 \cdot \pi R^3 = 50.76 \text{ mm}^3 & \text{(face centred cubic)} \end{cases} . \tag{45}$$

In [91], the calculation of the matrix volume was shown for a partial morphology. The total volume of the fragments of spherical shells inside the unit cell can be determined according to

$$V_{\mathrm{M}} = V_{\mathrm{U}} - \begin{cases} 4/3 \cdot \pi (R^3 - r^3) & \text{(primitive cubic)} \\ 8/3 \cdot \pi (R^3 - r^3) & \text{(body centred cubic)} \\ 16/3 \cdot \pi (R^3 - r^3) & \text{(face centred cubic)} \end{cases} . \tag{46}$$

Last, the free volume of the void(s) is given by

$$V_{\mathrm{free}} = \begin{cases} 4/3 \cdot \pi r^3 & \text{(primitive cubic)} \\ 8/3 \cdot \pi r^3 & \text{(body centred cubic)} \\ 16/3 \cdot \pi r^3 & \text{(face centred cubic)} \end{cases} . \tag{47}$$

An overview of these volumes is given in Table 3. Based on this volumetric values, the

Topology	V_{U} mm^3	V_{M} (synt.) mm^3	V_{M} (part.) mm^3	V_{S} mm^3	V_{free} mm^3
pc	37.93	23.80	1.50	$\frac{4}{3}\pi \cdot (R^3 - r^3)$	$\frac{4}{3}\pi \cdot r^3$
bcc	58.37	30.10	3.98	$\frac{8}{3}\pi \cdot (R^3 - r^3)$	$\frac{8}{3}\pi \cdot r^3$
fcc	107.3	50.76	12.21	$\frac{16}{3}\pi \cdot (R^3 - r^3)$	$\frac{16}{3}\pi \cdot r^3$

Table 3: Volumetric dimensions of MHSS in dependence on the inner radius r.

average density $\overline{\rho}$ of metallic hollow sphere structures can be determined according to

$$\overline{\rho}(r) = \frac{V_{\mathrm{M}} \cdot \rho_{\mathrm{M}} + V_{\mathrm{S}} \cdot \rho_{\mathrm{s}}}{V_{\mathrm{U}}}, \tag{48}$$

where ρ_{s} represents the density of the spherical shell and ρ_{m} the density of the matrix material. The relative free Volume V_{rel} which quantifies the porosity of the structure is defined as

$$V_{\mathrm{rel}} = \frac{V_{\mathrm{free}}}{V_{\mathrm{U}}}. \tag{49}$$

3.1.3 Discretisation

Finite element analysis demands the discretisation of the geometries by subdividing them into geometrically simple finite elements. In the scope of these analyses, primarily three dimensional geometries are considered. For the three dimensional meshing,

principally tetrahedral or hexahedral elements can be employed. Earlier investigations [59, 60] have shown that hexahedral elements yield superior performance. Therefore, the geometry of the structures is discretised based on regular hexahedral elements. This approach is much more time-consuming, but it is important in order to achieve a more accurate simulation of the non-linear behaviour (e.g. plasticity) of such materials.

Hollow Sphere Structures

Finite Element Models The meshing of the micro-structure of MHSS requires the decomposition of these complex geometries into simple sub-geometries. Based on the obtained fragments, meshing algorithms can be applied in order to obtain regular hexahedral meshes. Therefore, these sub-geometries have to exhibit a principally cubical shape. Fig. 20 demonstrates the decomposition of a syntactic body centred cubic geometry. In order to minimise the number of fragments, symmetries

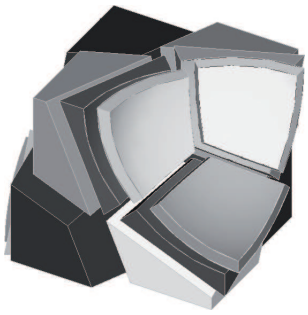

Figure 20: Segmentation of the geometry of a body centred cubic MHSS into sub-geometries.

are exploited. In the example shown, only 3 sub-geometries need to be meshed and, by mirroring, a total of 18 fragments are obtained which accumulate to the target geometry.

In the following, an overview of the utilised finite element meshes of the microstructure of MHSS is given. All meshes shown are generated for different sphere wall thicknesses t with the values $t = 0.02, 0.035, 0.05, 0.075, 0.1$. Figure 21 shows finite element meshes for syntactic morphology and the different topologies. The light grey elements exhibit the material properties of the matrix whereas the dark grey elements simulate the metallic shells. Depending on the considered joining technology, the matrix simulates the sintered necks or adhesive joints between the neighboring spheres. In Fig. 22 b) the primitive cubic geometry of the microstructure is rotated by 45^o around one of the symmetry axes. This approach allows the definition of new loading planes in order to investigate the anisotropic behaviour of the structure. It is discussed earlier in Section 2.1.1 that this second orientation of the loading planes enables the full characterisation of the elastic properties of geometries with cubic symmetry.

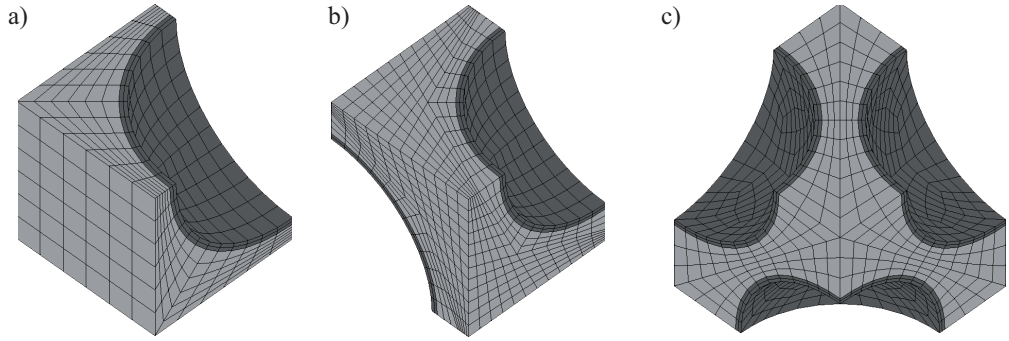

Figure 21: Syntactic finite element models ($t = 0.05$): a) Primitive cubic, b) Body centred cubic, c) Face centred cubic.

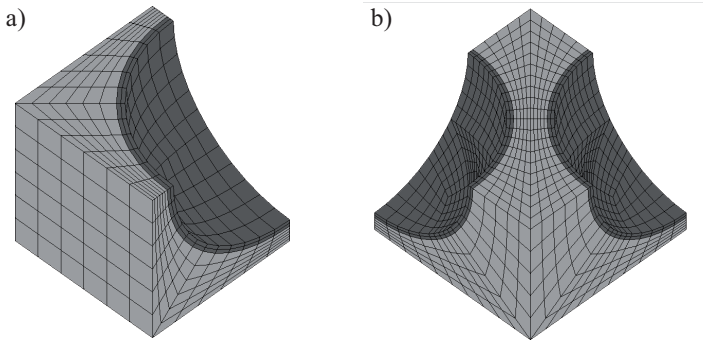

Figure 22: Different orientation of syntactic primitive cubic MHSS: a) Principal material coordinate system, b) Rotated material coordinate system.

Figures 23 and 24 display the corresponding finite element models for the partial morphology.

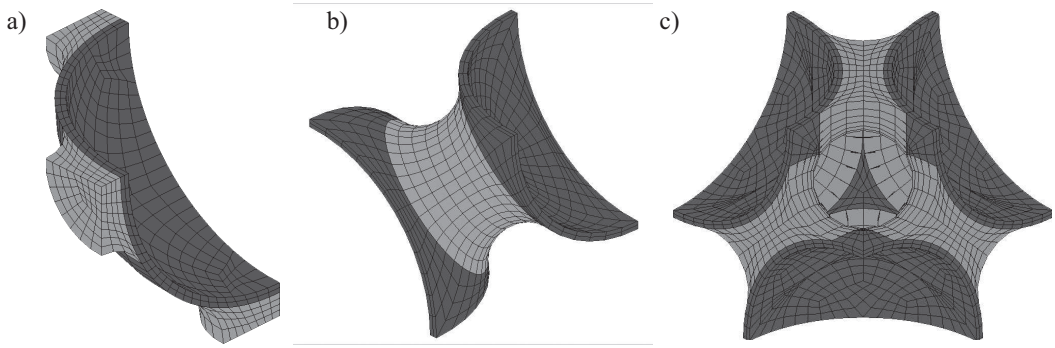

Figure 23: Partial finite element models ($t = 0.05$): a) Primitive cubic, b) Body centred cubic, c) Face centred cubic.

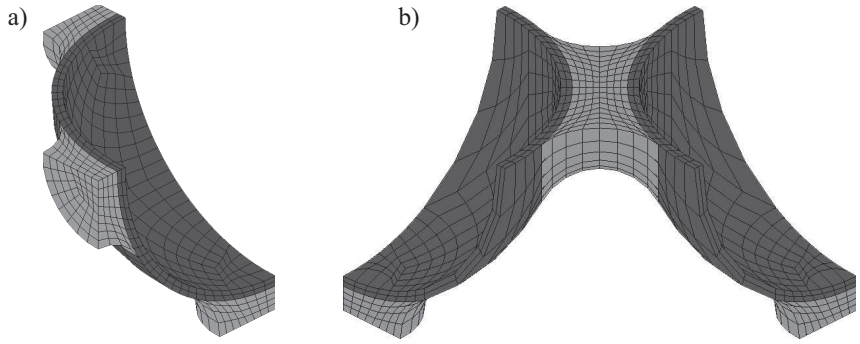

Figure 24: Different orientation of partial primitive cubic MHSS: a) Principal material coordinate system, b) Rotated material coordinate system.

Mechanical Boundary Conditions Uniaxial tensile and compressive tests of MHSS are simulated in order to determine their mechanical properties. Figure 25 illustrates the mechanical boundary conditions of these analyses. Due to the cubic symmetry of the MHSS and the applied loads, only one eighth of a unit cell needs to be considered within the finite element models. The uniaxial loading is prescribed by the definition of a nodal displacement $u(t)$ on all nodes that lie inside the upper surface. This time dependent boundary condition $u(t)$ is a ramp function which displaces the nodes in the negative y-direction. In order to simulate the mechanical response of the whole structure, repetitive [92] and reflective [93] boundary conditions are defined. The reflective symmetry conditions constrain the displacement perpendicular to the surface on which they are defined and simulate the influence of the remaining unit cell. Repetitive boundary conditions model the interaction with neighboring unit cells. According to these constraints, all nodes exhibit the *same* displacement in the direction of the normal vector of these surface. As result of these symmetry boundary conditions, the finite element models simulate an infinite structure where the influence of a free boundary is disregarded. This assumption holds for MHSS which comprise at least 10 spheres in each direction [55].

The macroscopic strains ε and stresses σ are obtained using a FORTRAN subroutine. The nodal forces F_n of all nodes within one of the three surfaces, where a repetitive boundary condition is prescribed, are summed up. The macroscopic engineering stresses σ are obtained by dividing this sum by the areas of the corresponding surfaces of the finite element models ($\sigma = \sum F_\mathrm{n}/A$). For the calculation of the engineering strains, the average displacement $\overline{u}_\mathrm{n}$ of these nodes perpendicular to the surface is determined and divided by the half length of the unit cell ($\varepsilon = 2\overline{u}_\mathrm{n}/l_s$).

Thermal Boundary Conditions A finite element model for the thermal analysis of the microstructure is illustrated as an example in Fig. 26. At the left and right side of the joints, two constant temperatures T_1 and T_2 are prescribed. The

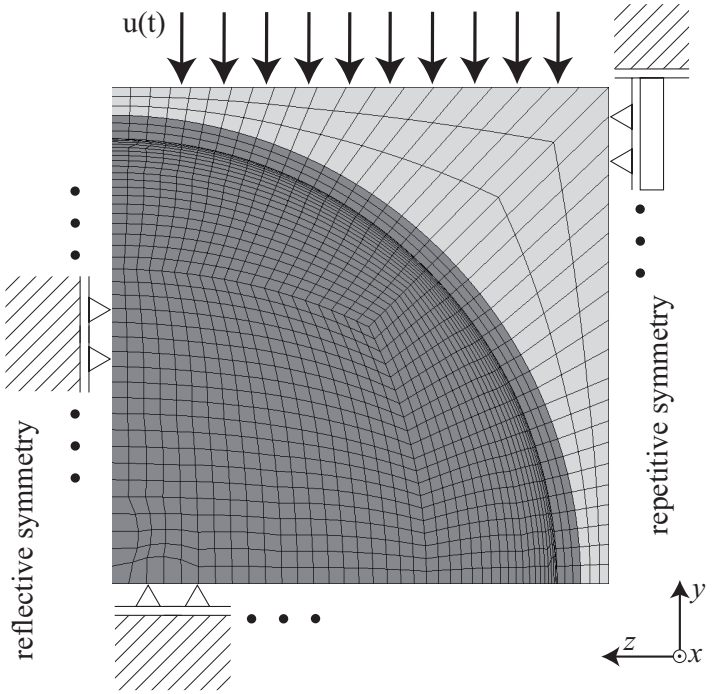

Figure 25: Boundary conditions of the mechanical finite element analysis.

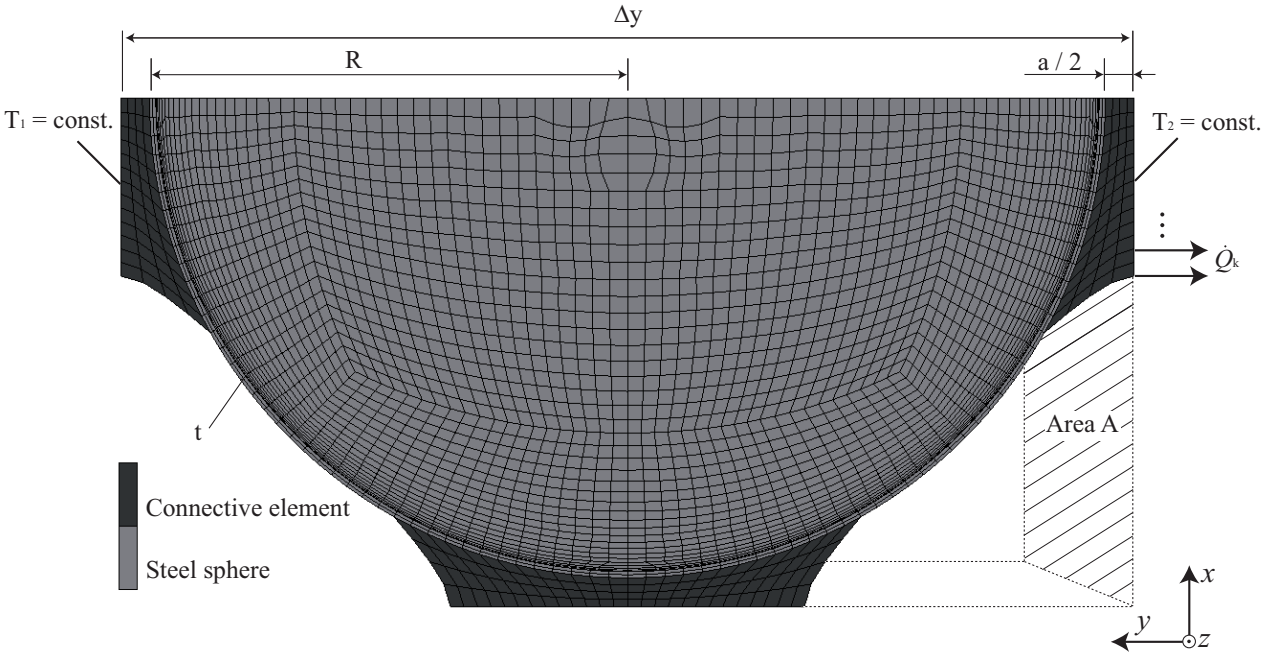

Figure 26: Boundary conditions of the thermal finite element analysis.

nodal reaction heat flux in the direction perpendicular to these surfaces is notated as $\dot{Q}_k$. The total heat flux through one of the surfaces where the temperature boundary condition is prescribed is given by the sum of the single nodal reaction fluxes

$$\dot{Q}(T_1, T_2) = \sum_j \dot{Q}_j(T_1, T_2), \tag{50}$$

where j denotes the number of nodes where T_1 or T_2 is assigned. The heat flux perpendicular to all remaining surfaces is zero which corresponds to periodic boundary conditions. It is shown in [18, 94] that the influence of thermal radiation on the effective thermal conductivity of porous metals, especially at temperatures below 700 K is low and its contribution to the effective thermal conductivity is therefore disregarded within these studies. Furthermore, the open porosity of MHSS is small (partial) or nonexistent (syntactic) and consequently also the effect of free or forced convection is excluded from the numerical simulation. Due to these simplifications, Fourier's law yields the effective thermal conductivity $\lambda_{\text{eff}}(T_1, T_2)$ (cf. Eq. 22) of the structure:

$$\lambda_{\text{eff}}(T_1, T_2) = \frac{\dot{Q}(T_1, T_2)}{A} \cdot \frac{\Delta y}{\Delta T}. \tag{51}$$

The spatial distance Δy and the projected area A are defined by the geometry (cf. Fig. 26), the temperature difference $\Delta T = T_2 - T_1$ is given by the boundary conditions and the total heat flux $\dot{Q}(T_1, T_2)$ is result of the finite element calculation.

Sandwich Structures

Finite Element Models A second class of finite element models comprises various sandwich structures. Figure 27 visualises a volumetric three dimensional finite element model of a sandwich structure. It is shown that the complex geometry of the microstructure of the MHSS core is not modelled. Instead, the macroscopic mechanical and thermal properties of the microstructure are assigned to the solid elements which represent the core material. This homogenisation technique allows for a significant reduction of required finite elements and therefore calculation time. The geometry of the sandwich structure is then determined by the total length l, the total height h, the thickness t of a single face sheet, the width w and, in case of the three-point bending tests, the span d_s between the supports of the specimen (cf. also Fig. 34).

Mechanical Analysis In the mechanical load cases, three-point bending tests of sandwich structures are simulated. The supports and the pressure stamp can be modelled by two different approaches. First, cylindrical contact bodies representing the two supports and the pressure stamp can be generated (cf. Fig. 27). The two supports position the sandwich structure and the pressure stamp transmits the bending and shear forces by continuously translating in the negative y-direction. However, the definition of the contact condition distinctly increases the calculation time

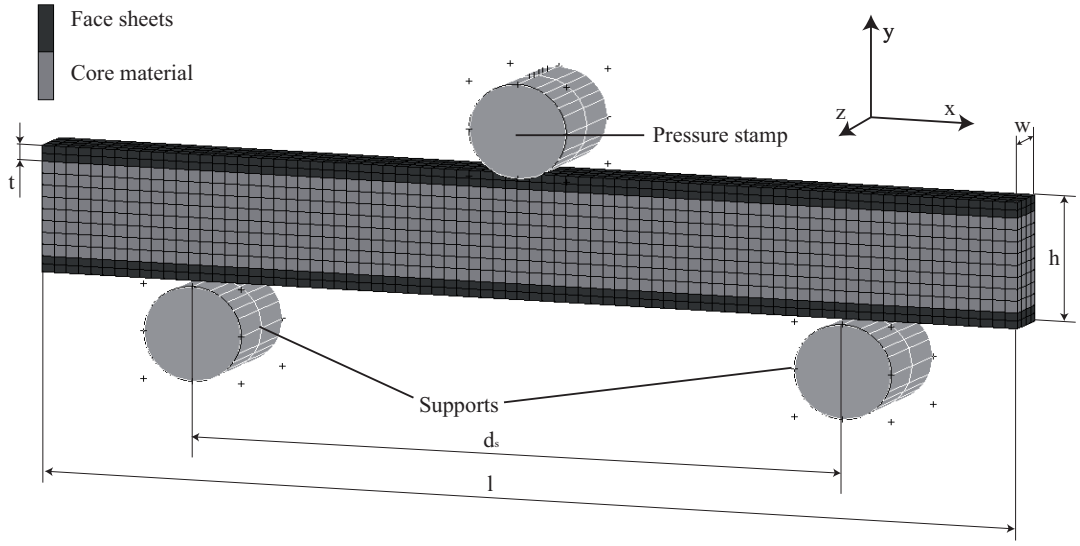

Figure 27: Three dimensional finite element mesh of a homogenised sandwich structure.

and oscillations in the contact forces between different contact bodies indicate numerical instabilities. Therefore, a second approach based on the prescription of nodal displacements is performed. The supports are modelled by the prevention of the displacement of the sandwich structure in the negative y-direction along the contact line between support and face sheet. Accordingly, the pressure stamp is substituted by a time dependent nodal displacement. A comparison of the obtained results for both approaches yields similar results. Therefore, nodal displacements are chosen for the definition of the boundary conditions in order to reduce calculation time and increase the numerical stability of the calculations.

Thermal Analysis For the thermal finite element analysis of sandwich structures, the results of the thermal conductivities of the microstructure (unit cell) of the MHSS at low temperature gradients (cf. Section 4.1.4) are assigned to a homogenised finite element model. Therefore, a simple two dimensional mesh is assembled by planar rectangular elements (thickness 1) with the thermal conductivity corresponding to the results obtained for the microstructure of a primitive cubic MHSS. This procedure allows for the simulation of large structures without the necessity of modelling the whole microstructure. Furthermore, two aluminium face sheets can be attached to the homogenised finite element model of the core in order to model a sandwich structure with a varying face sheet thickness t. The evaluation of the directional thermal conductivity perpendicular to the face sheets of the sandwich structure is performed according to Eq. (51).

3.1.4 Material Properties

Mechanical properties If not indicated differently, linear elasticity and ideal plasticity (VON MISES yield condition) are presumed for the base materials of the finite element models.

In the first part of the numerical analysis, different material combinations used in MHSS are investigated. Due to the manufacturing process (cf. Fig. 2), the sphere wall material is a sintered metal. In particular, the experimental samples provided by the enterprise GLEICH GMBH (Dresden, Germany) are sintered steel spheres. Depending on the sintering temperature and sintering time, the density and mechanical properties of the sintered steel can be adjusted. In order to confine the complexity of the numerical analysis, only high density spheres with superior mechanical properties are considered. The mechanical properties of this material were determined at the FRAUENHOFER INSTITUT in Dresden according to DIN ISO 5755 (German industrial norm) and are displayed in Table 4. The densities of the sintered steel alloys are obtained by cutting approx. 20 hollow spheres of each density carefully into pieces in order to remove the solid surface layer of the spheres. Then, the mass of these pieces is weighed on a precision balance. The total volume of the fragments is determined by pouring them into a fluid inside a measuring cup. The quotient of mass and volume change is the density of the material. In addition to the sintered steel, a sintered aluminium alloy [95] is considered in the numerical analyses in order to study the influence of the sphere wall material on the macroscopic properties of MHSS. The hollow spheres can be joined by adhesive bonding, casting or sintering. In the case of adhesive bonding, the mechanical properties of the adhesive are required. Therefore, compressive tests were performed on the epoxy resin L1100 (manufacturer: R&G GMBH, Waldenbuch, Germany) at the University of Maribor, Slovenia. Figure 28 shows the obtained stress-strain relation.

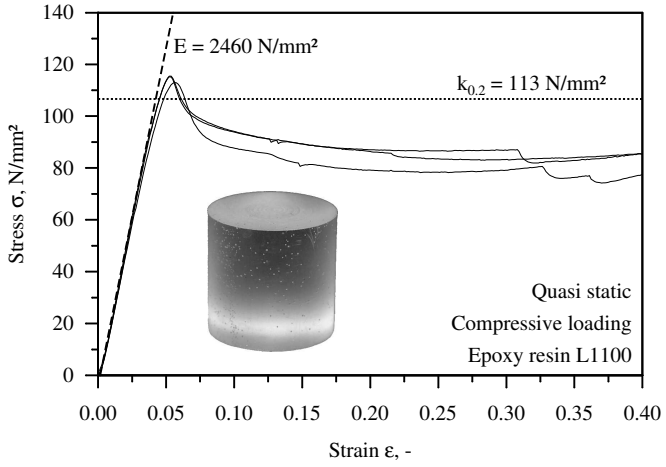

Figure 28: Mechanical properties of the epoxy resin L1100 [96].

In the second part of this work, three-point bending tests on sandwich compounds are performed. Thereby, the core materials are adhesively bonded with Al5005 aluminium face sheets. The mechanical properties of all base materials are summarised in Table 4.

Material	Abbreviation	E [N/mm^2]	ν [-]	k_t [N/mm^2]	k_c [N/mm^2]	ρ [kg/dm^3]
Sint. Steel (high dens.)	St	110000	0.3	300	300	6.95
Sint. Steel (low dens.)	-	-	-	-	-	5.35
Sint. Aluminium [95]	Al	58820	0.34	24	24	2.67
Epoxy Resin [97]	Ep	2460	0.36	61.5	113	1.13
Al5005 (UNS A95005) [98]	-	68900	0.3	127	127	2.7

Table 4: Mechanical properties of the base materials.

For reasons of comparison, 'classical' cellular materials are investigated in the experimental and finite element analyses. Two commercially available cellular metals are considered. The mechanical properties of the open celled M-Pore® aluminium sponge and the closed cell Alporas® foam are given in Table 5.

Material	E [N/mm^2]	ν [-]	k_t [N/mm^2]	k_c [N/mm^2]	ρ [kg/dm^3]
Alporas [99]	1100	0.33	0.33	1.6	0.34
M-Pore [100]	85	0.31	-	1.6	0.27

Table 5: Mechanical properties of commercial aluminium foams.

Thermal properties The thermal finite element analysis of MHSS requires the definition of the thermal properties of their base materials. The thermal conductivity λ of the epoxy resin L1100 is measured by the transient plane method which is further elucidated in the following section. The thermal conductivities of the considered metals are shown in Tab. 6. All visualised characteristic values are valid at room temperature.

Material	Abbreviation	Thermal conductivity λ [W/(mm·K)]
Steel	St	0.050
Aluminium	Al	0.232
Epoxy resin	Ep	0.000214

Table 6: Thermal material properties [101].

Furthermore, non-linear analyses with temperature dependent thermal material properties are performed. Therefore, further material models are included in the nu-

merical simulations. The temperature dependent thermal conductivities $\lambda(T)$ are plotted in Fig. 29 versus the absolute temperature T.

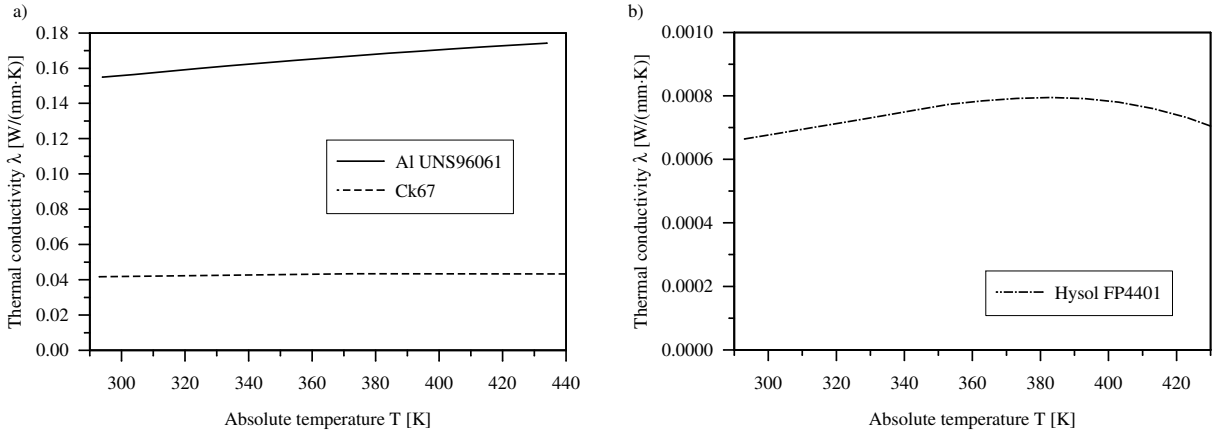

Figure 29: Temperature dependent thermal conductivities: Al UNS96061 [102], Ck67 [103], Hysol FP4401 [104].

3.2 Experimental Testing

In addition to the numerical analysis, experimental tests are performed. The intention is the comparison and validation of the numerical results with experimental data.

3.2.1 Mechanical Testing

All mechanical tests are performed on a uniaxial Shimadzu AG 50 kNG testing machine. The force is measured using a Shimadzu load cell with 50 kN maximum capacity. Figure 30 also shows the inductive displacement transducer (LVDT) which is used for the measurement of displacements. The measuring signals are processed in a HBM MGC+ measuring amplifier and captured on a mobile computer.

Two different types of mechanical experiments are performed. The uniaxial mechanical properties of MHSS are obtained by compressive testing. Furthermore, three-point bending tests are performed on MHSS and sandwich structures with various core materials.

Compressive Testing Compressive testing is used to determine Young's modulus E, the 0.2% offset yield strength $k_{0.2}$ and the hardening behaviour of MHSS. The experimental setup is schematically drawn in Fig. 31 a). In order to minimise friction, the surfaces of both pressure stamps are lubricated. The upper pressure stamp moves downwards with a constant velocity $\dot{u}(t) = 1$ mm/min and thereby continuously compacts the specimen. The samples are of cubical shape and have a side length of 30

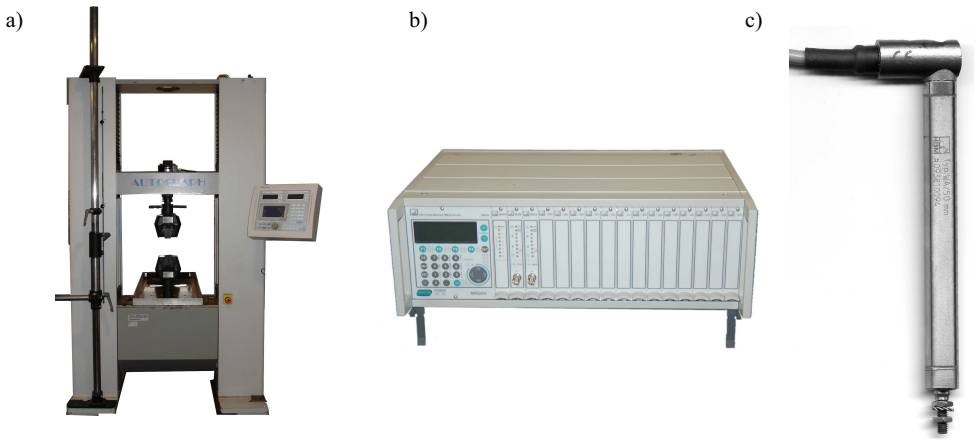

Figure 30: Experimental equipment: a) Uniaxial SHIMADZU testing machine, b) HBM MGC+ measuring amplifier, c) LVDT.

mm. Figure 31 shows a specimen before b) and after c) compressive loading. The

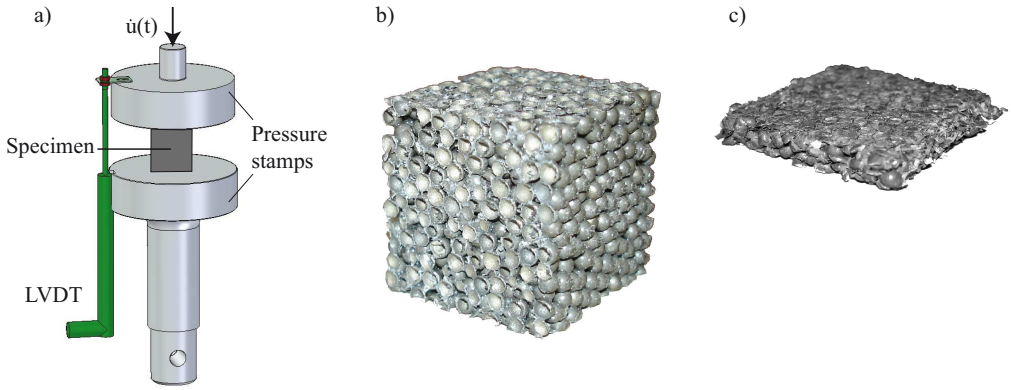

Figure 31: Compressive testing: a) Experimental set-up, b) MHSS specimen, c) MHSS specimen after compaction.

upper pressure stamp is attached to the load cell which records the reaction force of the sample. The displacement is measured with an inductive displacement transducer which is connected to both pressure stamps. In comparison to the measurement of the displacement at the crosshead of the testing machine, this arrangement avoids perturbations of the measurements due to the finite stiffness of the machine frame. The force and displacements signals are recorded with an MGC+ measuring amplifier and processed with the software CATMAN©.

For the evaluation of the compressive tests, the engineering stresses and strains are calculated. The engineering stress σ is defined by the measured force $F(t)$ divided by the initial cross section of the specimen $A = 900$ mm^2. The engineering strain ε is the measured displacement $u(t)$ divided by the initial height (30 mm) of the sample. According to Eq. (1) Young's modulus can be determined: $E = \sigma/\varepsilon$. The 0.2 % offset

yield strength $k_{0.2}$ and the hardening behaviour are obtained by the evaluation of the stress-strain diagram.

Three-Point Bending The central aim of this work is the evaluation of the performance of novel MHSS as cores in sandwich panels. Therefore, three-point bending tests are performed. The experimental setup of the three-point bending test is shown in Fig. 32. The specimen is positioned on top of two rotatable cylindrical bearings. The bending force is transmitted by the pressure cylinder which moves downwards with the constant velocity $\dot{u}(t) = 1$ mm/min. This pressure cylinder is connected with the pressure stamp. The pressure stamp again is attached to the load cell in the cross head of the machine, which is utilised for the measurement of the reaction force $F(t)$. The displacement $u(t)$ is gauged by an inductive displacement transducer (LVDT). The transducer is attached to the pressure cylinder and positioned on the bottom plate between the stiff posts. All elements of the fixture are manufactured in massive steel in order to minimise the superimposition of its elastic deformation on the measured displacement signal. Furthermore, all moving parts and contact surfaces are lubricated for friction minimisation.

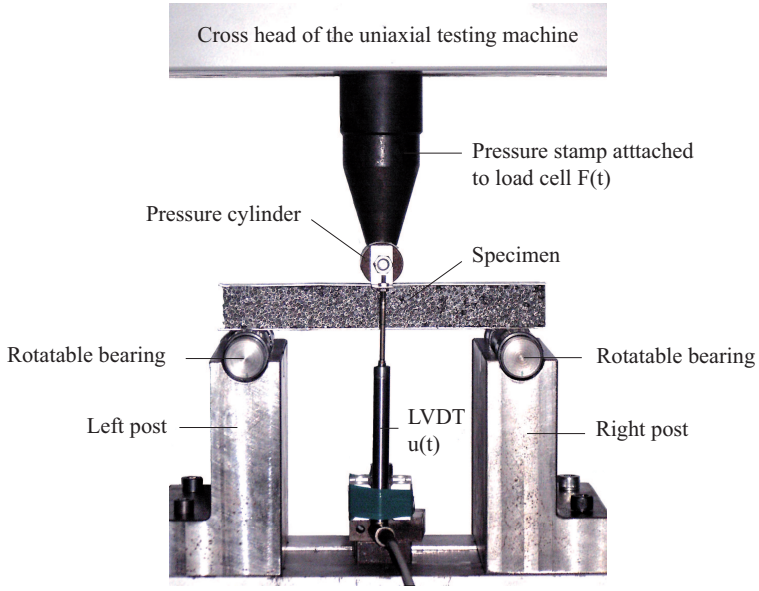

Figure 32: Experimental set-up of the three-point bending test.

In order to obtain additional data for the comparison with the numerical results, strain gauges (cf. Fig. 33) are attached to some of the sandwich specimens. The measurement of strain using strain gauges assumes that the strain on the object is transferred without loss to the strain gage. The very close bonding which is required between the specimen and the strain gage is best provided by an adhesive [105]. The resistance of an electrical conductor changes with mechanical stress. This change of

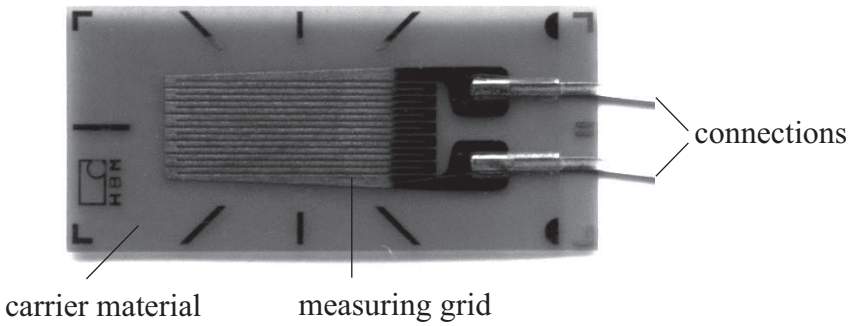

Figure 33: Strain gauge.

resistance is caused by the conductor's geometrical deformation and the change in resistivity of the conductor material as a result of changes within the microstructure. For strain gauges, materials are chosen where the change of resistance in dependence on the strain exhibits a linear characteristic. Accordingly, strain gauges can be characterised by their sensitivity or gauge factor k:

$$k = \frac{\Delta R/R_0}{\Delta l/l_0} = \frac{\Delta R/R_0}{\varepsilon}. \tag{52}$$

ΔR is the change in electrical resistance of the strain gage, R_0 its initial electrical resistance and $\varepsilon = \Delta l/l_0$ the engineering strain. Equation (52) relates the change of resistance which is measured during the experiment to the mechanical strains. In conjunction with the gauge factor k, which is provided by the manufacturer, the strain ε can be determined. Within the linear-elastic area, Hooke's law (1) can be applied to calculate local stresses according to $\sigma = E/\varepsilon$. During the measurement, strain gauges are inserted in a Wheatstone bridge circuit [106]. Therefore, the strain gauge is connected to a measuring amplifier of the type MGC+ (HBM) which internally supplements the circuit and captures the signal during testing. The advantages of this circuit are the automatic correction of linearity deviations in the strain gauge characteristic [107, 108, 109] and the insensitivity to the strain gauge resistance tolerances. Figure 34 a) displays a schematic drawing of the experimental set-up of the three-point bending test. All geometric dimensions with relevance towards the evaluation are given. The geometry of the sandwich panel is characterised by the total height h, the face sheet thickness t, the core thickness c, the width w and its total length l. The span d_s between the supports and the overhang d_o complete the required dimensions. The flexural loading triggers a torque $M(x,t)$ and a shear force $Q(x,t)$ as visualised in Fig. 34 b).

The determination of Young's modulus of isotropic materials based on the results of the 3-point bending test [110, 111] is performed by the evaluation of the well-known formula of the bending line $b(x)$ (e.g. [45])

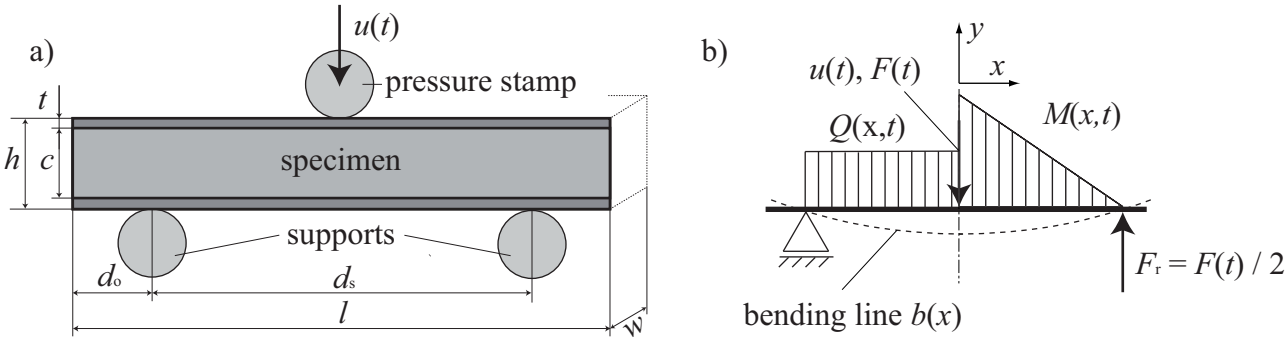

Figure 34: Three-point bending experiment: a) Schematics, b) Transmitted loads.

$$E \cdot I_{zz} \cdot b''(x) = M(x). \tag{53}$$

It should be mentioned here that the symbol E in Equation (53) is equal to Young's modulus only in the case of homogeneous and isotropic materials. Sandwich structures typically exhibit highly different material properties of face sheets and core material. Accordingly, the symbol E is replaced by E_{Str} which is in the following referred to as flexural stiffness. I_{zz} is the geometrical moment of inertia and in the case of a rectangular cross section [45] is equal to

$$I_{zz} = \frac{w \cdot h^3}{12}. \tag{54}$$

The distribution of the torque $M(x,t)$ inside the beam ($0 \leq x \leq d_s/2$) is given by

$$M(x,t) = \frac{F(t)}{2} \cdot \left(\frac{d_s}{2} - x \right). \tag{55}$$

Incorporation of the boundary conditions $b'(x = 0) = 0$ (symmetry) and $b(x = d_s/2) = 0$ (support) into Eq. (53) yields

$$E_{\mathrm{Str}} \cdot I_{zz} \cdot b(x) = -\frac{F(t)}{12}x^3 + \frac{F(t) \cdot d_s}{8}x^2 - \frac{F(t) \cdot d_s^3}{48}. \tag{56}$$

The displacement $b(x = 0)$ and the force $F(t)$ are measured in the experiment, respectively finite element simulation, and so E_{Str} is given by

$$E_{\mathrm{Str}} = -\frac{d_s^3}{4 \cdot w \cdot h^3} \cdot \frac{F(t)}{b(x = 0)}. \tag{57}$$

For a more accurate evaluation of the three-point bending test, also the deflection b_s due to the shear loading [45] has to be incorporated in the evaluation:

$$b_s'(x) = \frac{Q(x,t)}{A \cdot G}. \tag{58}$$

For three-point bending the shear force Q is equal to $F(t)/2$ for $-d_s/2 < x < 0$ and A is defined as [45]

$$A = \frac{w \cdot s^2}{c}, \tag{59}$$

where $s = c + t$ is the distance between the centrelines of the face sheets. In general, the shear modulus G is unknown. A pure shear state to determine G could be realised by torsion of cylindrical specimens. However, not all composite materials can be manufactured as cylindrical specimens and the test realisation would require a special testing machine. Alternatively, the shear modulus G may be estimated based on Young's modulus E. For *isotropic* materials the following relation holds:

$$G = \frac{E}{2(1+\nu)}. \tag{60}$$

For classical engineering materials Poisson's ratio ranges in the interval from 0 to 0.5. Based on these two extreme values, Eq. (60) yields

$$\frac{E}{3} \leq G \leq \frac{E}{2}. \tag{61}$$

Integration of Eq. (58) and application of the boundary condition $b_s(x = -d_s/2) = 0$ yields for the shear deflection

$$b_s(x) = \frac{Q}{A \cdot G} x - \frac{Q \cdot d_s}{2 \cdot A \cdot G}. \tag{62}$$

The total bending line b_t is obtained by linear superposition of the solution of the shear and the bending deflection as

$$b_t(x) = b(x) + b_s(x). \tag{63}$$

Transformation of Eq. (63) and substitution of G according to relation (60) finally yields for the flexural stiffness

$$E_{\mathrm{Str}} = -\frac{d_s^3}{4 \cdot w \cdot h^3} \cdot \left[1 + \frac{K_1 \cdot c \cdot h^3}{d_s^2 \cdot (c+t)^2}\right] \cdot \frac{F(t)}{b_t(x=0)} \tag{64}$$

with $K_1 = 2 \vee 3$ for $\nu = 0 \vee 0.5$. By comparing Eqs. (57) and (64) it becomes clear that the term $\frac{K_1 \cdot c \cdot h^3}{d_s^2 \cdot (c+t)^2}$ weighs the influence of the shear loading on the evaluation of the flexural stiffness. This term is proportional to $1/d_s^2$ and therefore for larger spans d_s the influence of the shear deflection can be neglected [110].

However, this approach is not valid for *heterogeneous* materials, i.e. sandwich panels. Since the material is no longer isotropic, the shear modulus G cannot be calculated based on the flexural stiffness E_{Str} of the structure. Alternatively, an evaluation method is used where the total deflection $b_t(x)$ is corrected by subtracting the

shear deflection $b_s(x)$ of the core. Therefore, the shear modulus G_c of the core needs to be known and then $b_s(x)$ can be calculated according to Eq. (62). Equation (63) now yields the deflection $b(x)$ which is exclusively due to bending and Eq. (57) can be applied for the determination of the structural flexural stiffness E_{Str}.

If the material properties of the base materials and the geometric dimensions are known, the flexural stiffness E_{Str} of a sandwich panel can be estimated by relating the flexural rigidity D_h of a homogenous material

$$D_h = E_{\mathrm{Str}} \cdot I_{zz} \tag{65}$$

to the flexural rigidity D_{Str} (e.g. [45]) of the sandwich structure

$$D_{\mathrm{Str}} = E_f \cdot \frac{w \cdot t^3}{6} + E_f \cdot \frac{w \cdot t \cdot s^2}{2} + E_c \cdot \frac{w \cdot c^3}{12}. \tag{66}$$

The variable I_{zz} is defined in Eq. (54), t is the thickness of a single face sheet, c the height of the core (cf. Fig. 34), s the distance between the centrelines of the upper and lower face sheet and E_f and E_c are Young's moduli of the face sheets and the core material respectively. The second expression in Eq. (66) is the contribution due to Steiner's theorem. Transforming the equality condition $D_{\mathrm{Str}} = D_h$ yields for the flexural stiffness of the structure E_{Str}:

$$E_{\mathrm{Str}} = \frac{6 \cdot E_f \cdot t \cdot s^2 + 2 \cdot E_f \cdot t^3 + E_c \cdot c^3}{h^3}. \tag{67}$$

3.2.2 Thermal Testing

The Transient Plane Source (TPS) is a transitory method to determine the thermal conductivity λ. All transitory methods are based on the analysis of the transient term solution of the heat conduction equation, which relates the change in temperature with time. These methods can be used to measure properties of inhomogeneous and/or anisotropic materials, offering the additional ability to measure in small samples. The TPS method has been successfully applied to cellular materials such as polymer and aluminium foams [112, 113].

In the TPS method, a round and plane heat source is used. It behaves as a transient plane source working simultaneously as a temperature sensor. This element consists of an electrical conducting pattern of thin nickel foil (10 μm thick) in the form of double spiral, inserted between two insulating layers made of Kapton. The TPS element is located between two samples with both sensor faces in contact with the two samples surfaces (cf. Fig. 35 a)). Two samples of similar characteristics are required for this purpose.

To perform the experiments, a constant electric power is supplied to the hot-disk sensor. The increase in temperature $\Delta T(t)$ is directly related to the variation in the

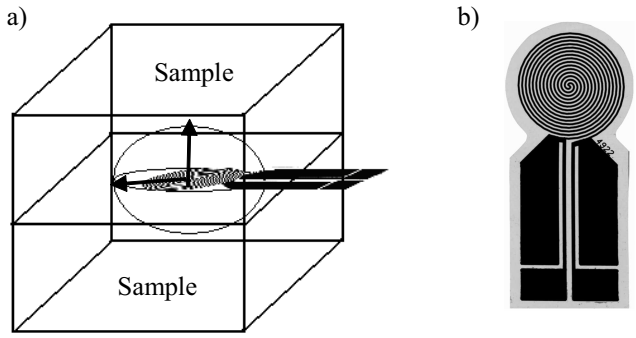

Figure 35: Transient plane source method: a) Experimental setup, b) Sensor.

sensor resistance $R(t)$ by the equation

$$R(t) = R_0 \cdot [1 + \alpha \cdot T(t)]\,, \tag{68}$$

where R_0 is the disk resistance at the beginning of the recording (initial resistance) and α is the temperature coefficient of resistance of the nickel foil. To relate the change in temperature with time, the equation for the heat conduction, assuming the conditions reported by Log et al. [114] and Gustavsson et al. [115], is applied.

4 Results

4.1 Hollow Sphere Structures

The first part of this work aims for the determination of the mechanical properties of metallic hollow sphere structures. Extensive numerical analyses are performed to understand the influence of the geometry and material composition of the microstructure on the macroscopic properties of MHSS. These numerical results are then compared to experimental findings.

4.1.1 Mechanical Properties: Finite Element Method

In the following, the results of the numerical analysis of the quasi-static uniaxial compressive and tensile testing of MHSS are discussed.

Adhesively Bonded Structures First, adhesively bonded structures are considered. Two morphologies can be distinguished: partial MHSS and syntactic MHSS (cf. Fig. 18). The stress-strain relations of these structures are plotted in Fig. 36. It can be observed that the syntactic MHSS exhibit higher stresses in comparison to the partial structures. Furthermore, the stresses increase with the density of the structure. As elucidated in Section 3.1.2, the change in density is caused by different sphere wall thicknesses t of the spherical shells. The stress-strain curves can be divided in a linear-elastic area, an elastic-plastic transition zone and the typical stress plateau for cellular materials. It should be mentioned here that within the scope of the finite element analysis all stress-strain relations exhibit the same characteristics. Therefore, only the material parameters E, ν and k will be discussed in the following and the stress-strain relations will only be shown in selected cases.

The linear-elastic area can be characterised by the material parameters Young's modulus E and Poisson's ratio ν. Young's modulus is plotted in Fig. 37 versus the average density $\overline{\rho}$ of the structures. The stiffness of partial MHSS increases linearly with the density, whereas the curve of syntactic MHSS exhibits a parabolic shape. In the field of lightweight technology, high specific material parameters are of great interest. If a material parameter is plotted versus the density, high specific values are located in the top left area of the graph. Identical specific values lie on straight lines that intersect the origin of the coordinate system. Accordingly, it can be concluded that syntactic MHSS exhibit the higher specific stiffness for average densities $\overline{\rho} > 0.52$ g/cm^3. Figure 38 shows Poisson's ratio of adhesively bonded MHSS. The syntactic MHSS exhibit much higher values for ν than the partial structures. This deviation can be explained by the significantly smaller volume fraction of the adhesive matrix in partial MHSS. Here, the joints that connect neighboring spheres act as thin rods that can contract and compress freely without causing strong transversal contractions.

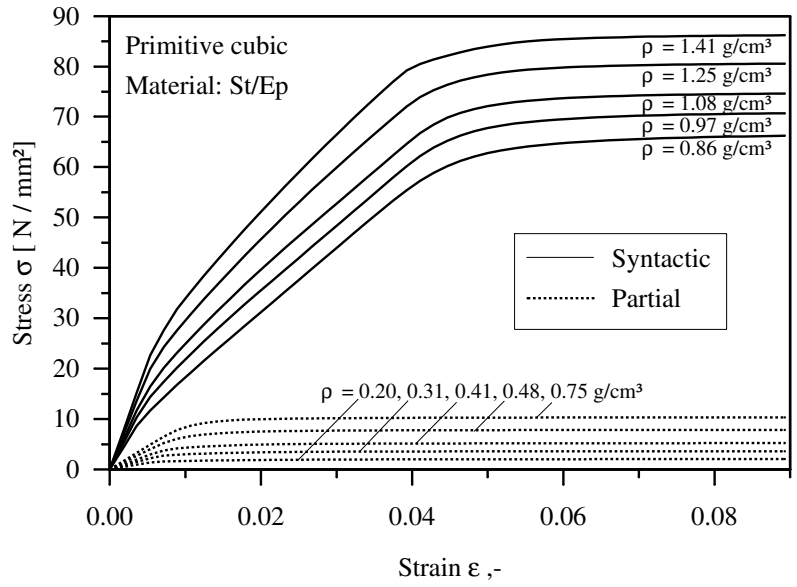

Figure 36: Stress-strain relations of adhesively joined MHSS.

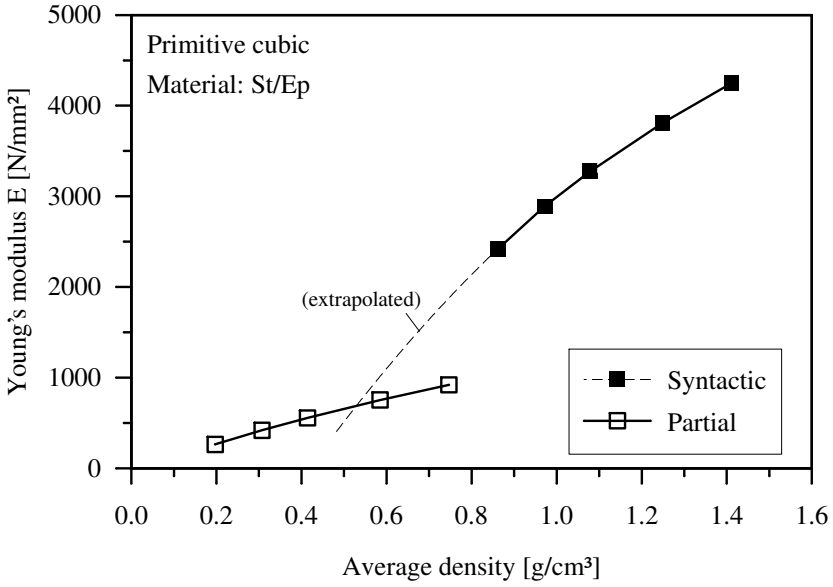

Figure 37: The dependence of Young's modulus E of adhesively bonded MHSS on the average density $\overline{\rho}$.

In contrast, the syntactic structures exhibit high Poisson's ratio ν that lie within the range of value of the epoxy resin $\nu_{\text{Epoxy}} = 0.36$.

Figure 39 shows the initial yield stresses k_c and k_t plotted versus the average density. The curves of both morphologies exhibit a linear characteristic. The epoxy resin exhibits anisotropic material properties, in particular the initial yield stress varies

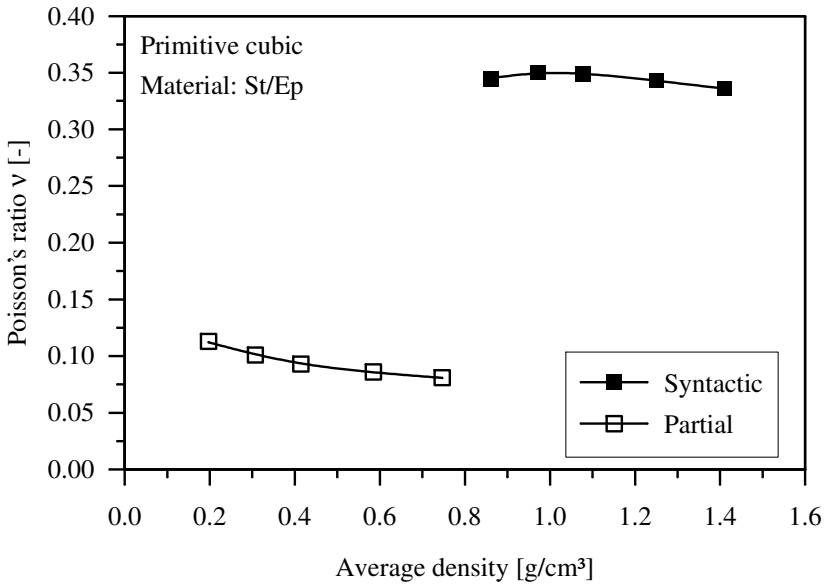

Figure 38: The dependence of Poisson's ratio ν of adhesively bonded MHSS on the average density $\overline{\rho}$.

for compressive k_c and tensile k_t loading. Therefore, also the initial yield stress of adhesively bonded MHSS is dependent on the loading direction. However, this effect is weak and only for small densities and partial morphology can a systematic deviation be observed.

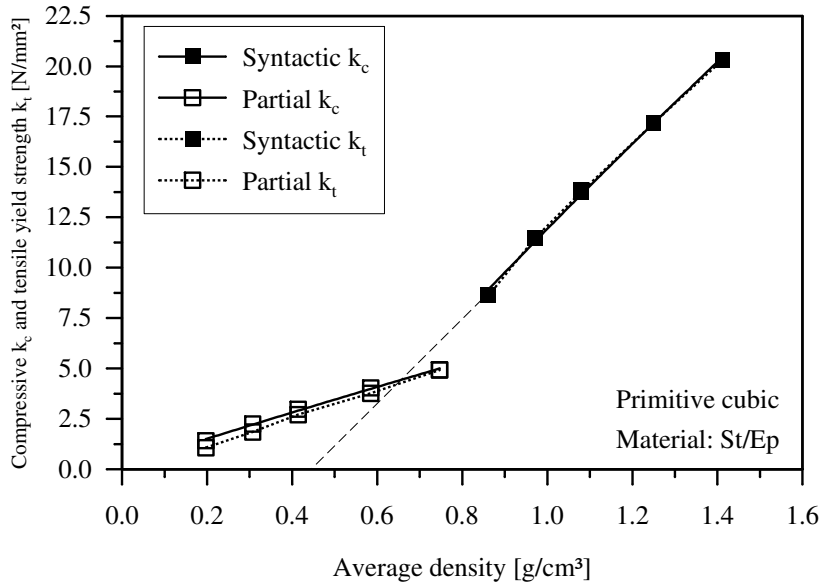

Figure 39: Initial yield stresses k_c and k_t of adhesively bonded MHSS dependence on the average density $\overline{\rho}$.

In the next step, the influence of the topology on the macroscopic properties of the structures is investigated. Figure 40 shows the dependence of the elastic material parameter Young's modulus E on the average density for different topologies. In the case of partial MHSS, a complex behaviour emerges. As already shown in Fig. 37, primitive cubic MHSS show a linear dependence on the average density. Body centred and face centred cubic MHSS exhibit higher stiffness at lower densities but increase proportionally less. For syntactic morphology, the highest specific values can be observed for a face centred cubic arrangement of the hollow spheres. However, the deviation in stiffness between the different topologies is small. As a consequence, Young's modulus E can be estimated by the linear function $E(\rho) = 3300 \cdot \rho$ [N/mm^2]. Poisson's ratio of adhesively bonded MHSS is shown in Table I in Appendix A. In the case of syntactic morphology, this material parameter is widely independent of the topology and sphere wall thickness and equal to $\nu = 0.34...0.35$. In contrast, Poisson's ratio of partial MHSS shows a strong dependence on the sphere wall thickness t of the hollow spheres and generally increases with this value, in particular for the body centred cubic topology.

Figure 41 shows the initial compressive k_c and tensile k_t yield stress dependencies on the average density. The full lines correspond to the compressive yield stress, whereas the dotted lines indicate the tensile yield stress. A linear fit can be employed in order to estimate the initial compressive yield stress k_c dependence on the average density. However, at low densities, the primitive cubic MHSS exhibit a slightly higher yield stress in comparison to the other cubic symmetrical structures. By comparing the tensile and compressive yield stresses it becomes clear that for low densities the values coincide. However, with increasing density the curves of the tensile yield stresses exhibit a sharp edge. The explanation is the relocation of the initial region of plastification. With increase of the density and therefore sphere wall thickness t, the initial area of plastification changes from the isotropic metallic sphere to the anisotropic adhesive matrix and therefore affects the macroscopic response of the structure.

The initial compressive and tensile yield stress of syntactic MHSS is not affected by the topology of the structure. The material parameter is well approximated by the linear function $k_c(\rho)$ as indicated in Figure 42. Furthermore, no dependency on the loading direction is observed for syntactic and adhesively bonded MHSS.

Casted and Sintered Structures In this section, the finite element results for the mechanical properties of sintered and casted MHSS are shown. Since the material properties of the sphere walls and the matrix are identical, these structures in the following are referred to as homogeneous structures.

Figure 43 shows the dependence of Young's modulus E of homogeneous MHSS on the average density $\overline{\rho}$. Due to the low porosity of syntactic MHSS in conjunction with the high density of the metallic matrix ρ_{m}, the average density of these structures is

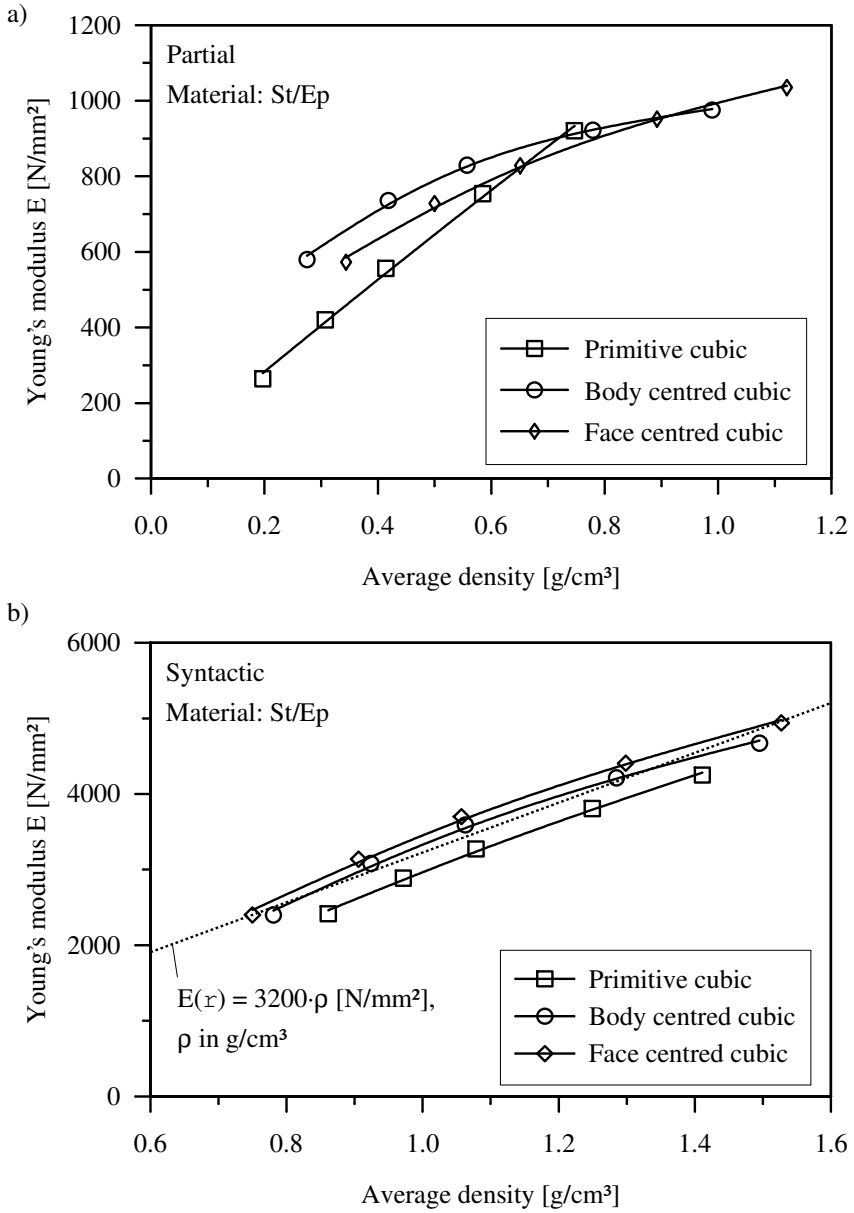

Figure 40: Young's modulus E of adhesively bonded MHSS in dependence on the average density $\overline{\rho}$ for different topologies: a) Partial, b) Syntactic.

much higher in comparison with the partial MHSS. The stiffnesses E of partial and syntactic MHSS are linearly dependent on the average density. The Poisson numbers of homogeneous MHSS are given in Table II in Appendix A. Poisson's ratios for primitive cubic topology and syntactic morphology are approximately 0.25. The Poisson number of sintered structures increases from 0.19 to 0.23 with increasing average density of the structure.

In Fig. 44 the initial yield stress is plotted versus the average density. The applied

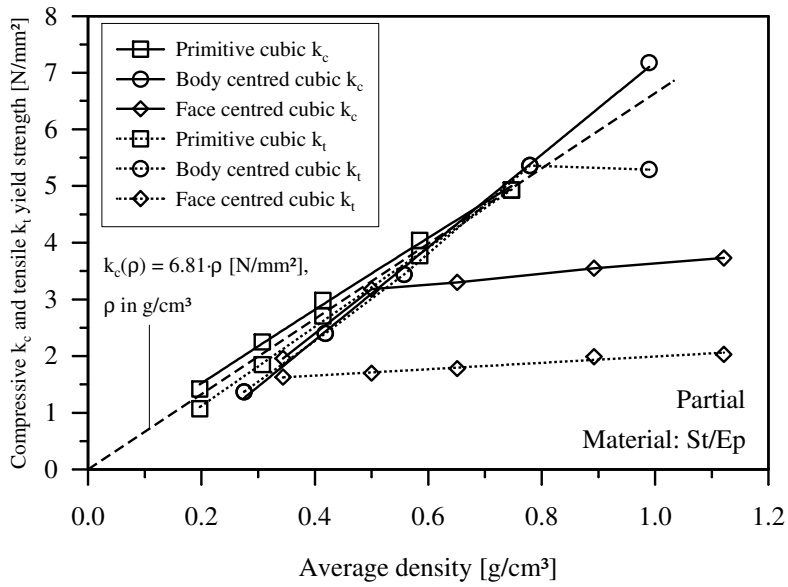

Figure 41: Initial compressive k_c and tensile yield stress k_t of adhesively bonded partial MHSS dependence on the average density $\overline{\rho}$ for different topologies.

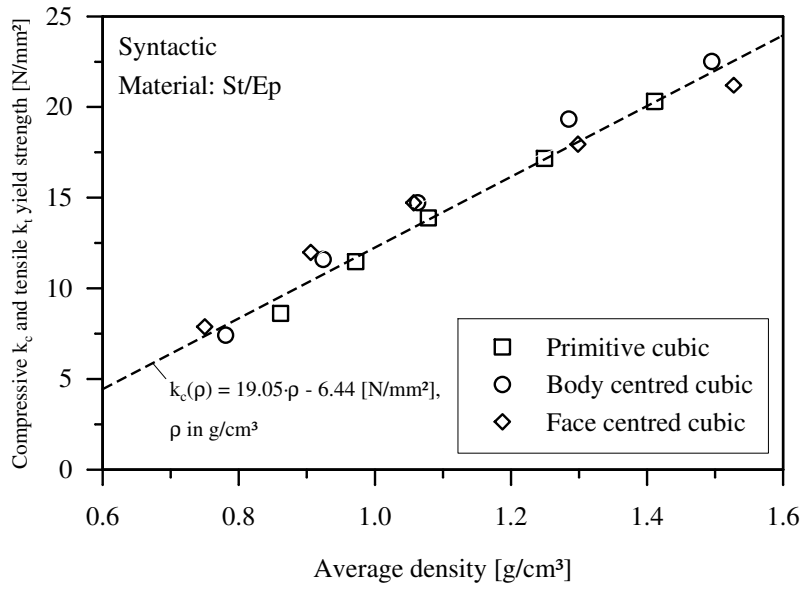

Figure 42: Initial compressive k_c and tensile yield stress k_t of adhesively bonded syntactic MHSS dependence on the average density $\overline{\rho}$ for different topologies.

material model for the sintered metal presumes isotropic material behaviour and consequently no difference between the compressive k_c and tensile yield stress k_t is observed. Analogous to Young's modulus the initial yield stress shows a linear dependence on the average density for both morphologies.

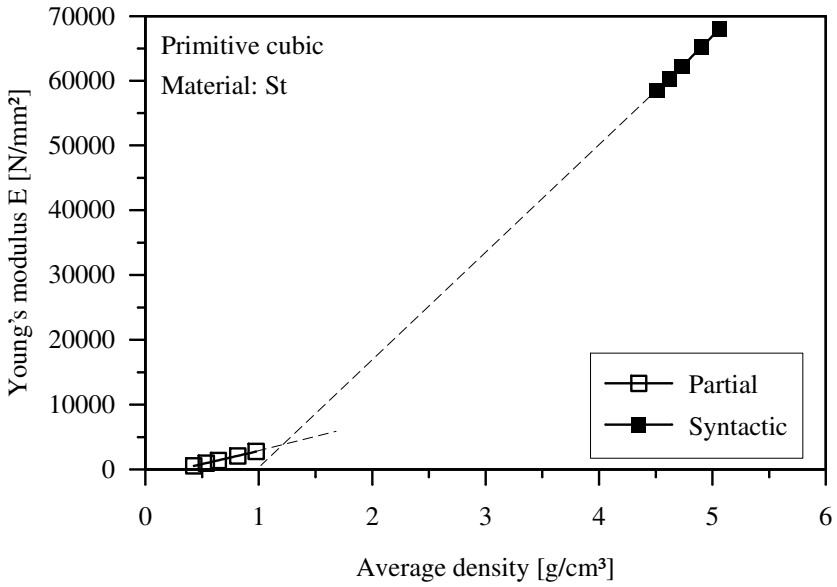

Figure 43: Young's modulus E of homogeneous MHSS dependence on the average density $\overline{\rho}$.

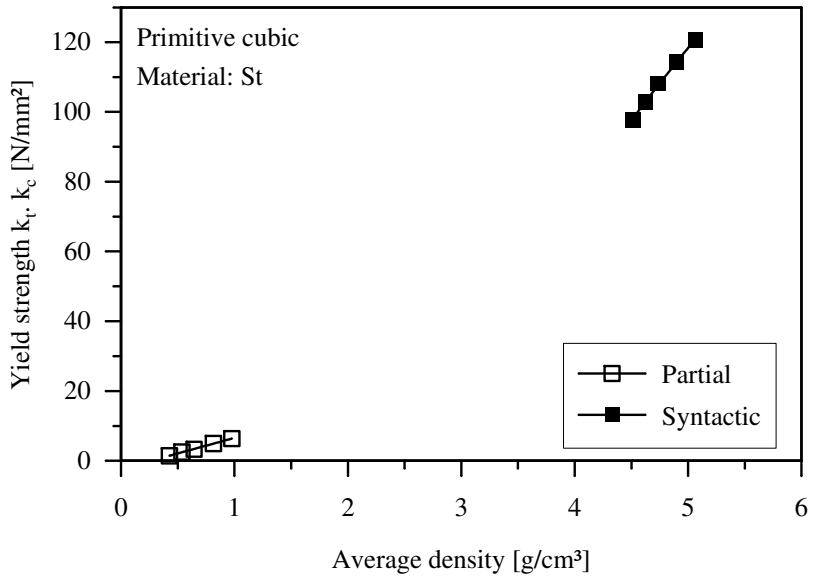

Figure 44: Initial yield stresses k_c and k_t of homogeneous MHSS in dependence on the average density $\overline{\rho}$.

In the following, the influence of the topology on the macroscopic properties of MHSS is investigated. Figure 45 shows Young's modulus E for primitive cubic, face centred cubic and body centred cubic arrangements of spheres. In the case of partial MHSS a strong dependence on the topology is observed. The primitive cubic arrangement exhibits the lowest absolute and specific stiffnesses E. The highest values are

obtained for body centred cubic MHSS which fact suggests the use of this arrangement of spheres for lightweight applications, where a high specific stiffness is aimed for. A different picture emerges for syntactic morphology. Here, the primitive cubic MHSS exhibit the highest absolute and specific Young's modulus. The corresponding results for the body centred and face centred cubic structures are similar, only slightly higher values are observed for the bcc structures. The values for Poisson's ratio are listed

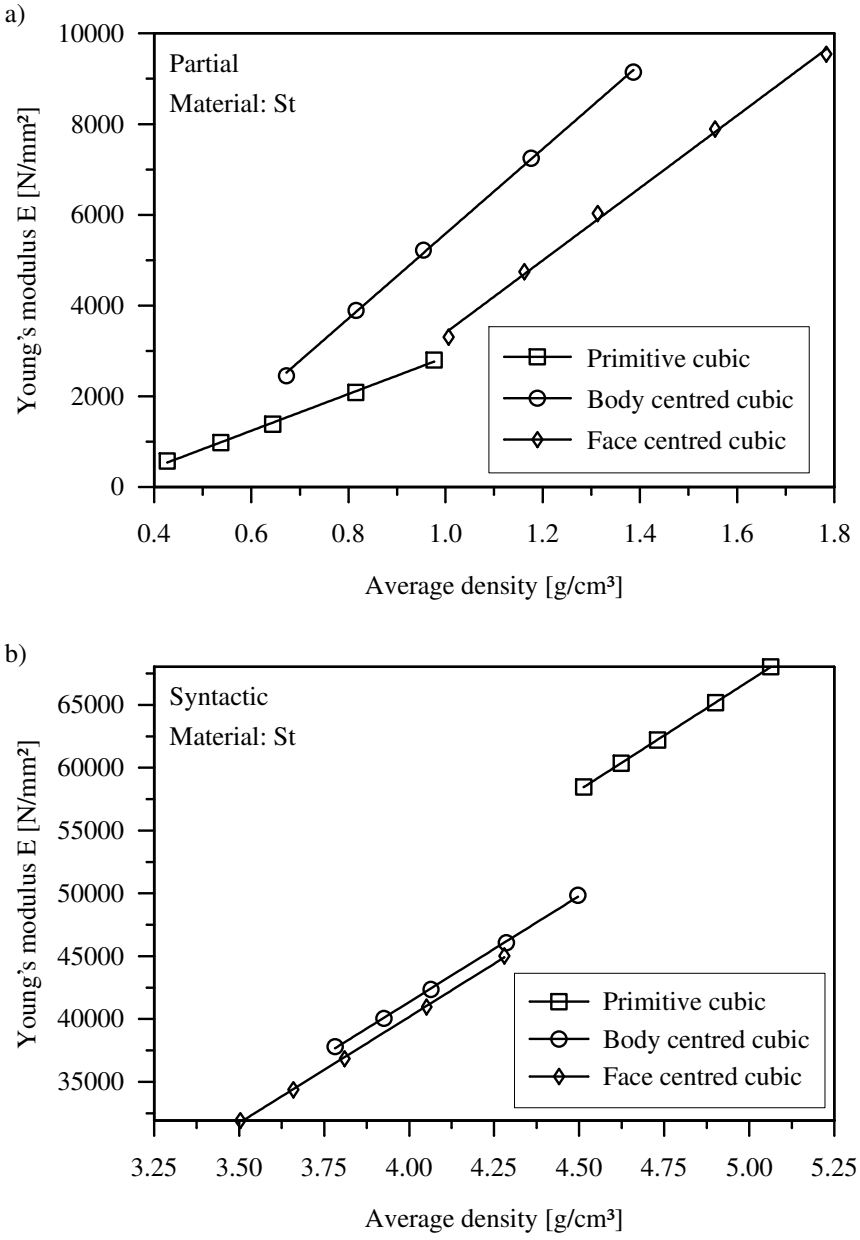

Figure 45: Young's modulus E of homogeneous MHSS dependence on the average density $\overline{\rho}$ for different topologies: a) Partial, b) Syntactic.

in Table II. The Poisson number for syntactic morphology varies slightly with the topology, but shows no significant dependence on the density. In general, Poisson's ratio of syntactic morphology is distinctly higher than for partial morphology. An anomaly is observed for partial morphology and body centred cubic topology. Due to the elastic deformation mechanism inside the structure a negative Poisson number is obtained for the two smallest densities. The localisation of the deformation yields a positive transversal contraction for tensile and a negative transversal contraction for compressive loading.

Figure 46 shows the initial yield stress plotted versus the average density. As mentioned above, the tensile k_t and compressive k_c yield stresses which coincide for homogeneous structures. The yield stresses of partial homogeneous structures exhibit a distinct dependence on the topology. The primitive cubic arrangement of spheres yields the maximum absolute and specific yield strength. Accordingly, this topology is advantageous for lightweight applications which require the bearing of high loads. In the case of syntactic morphology a linear function is provided as a rough approximation of the yield strength.

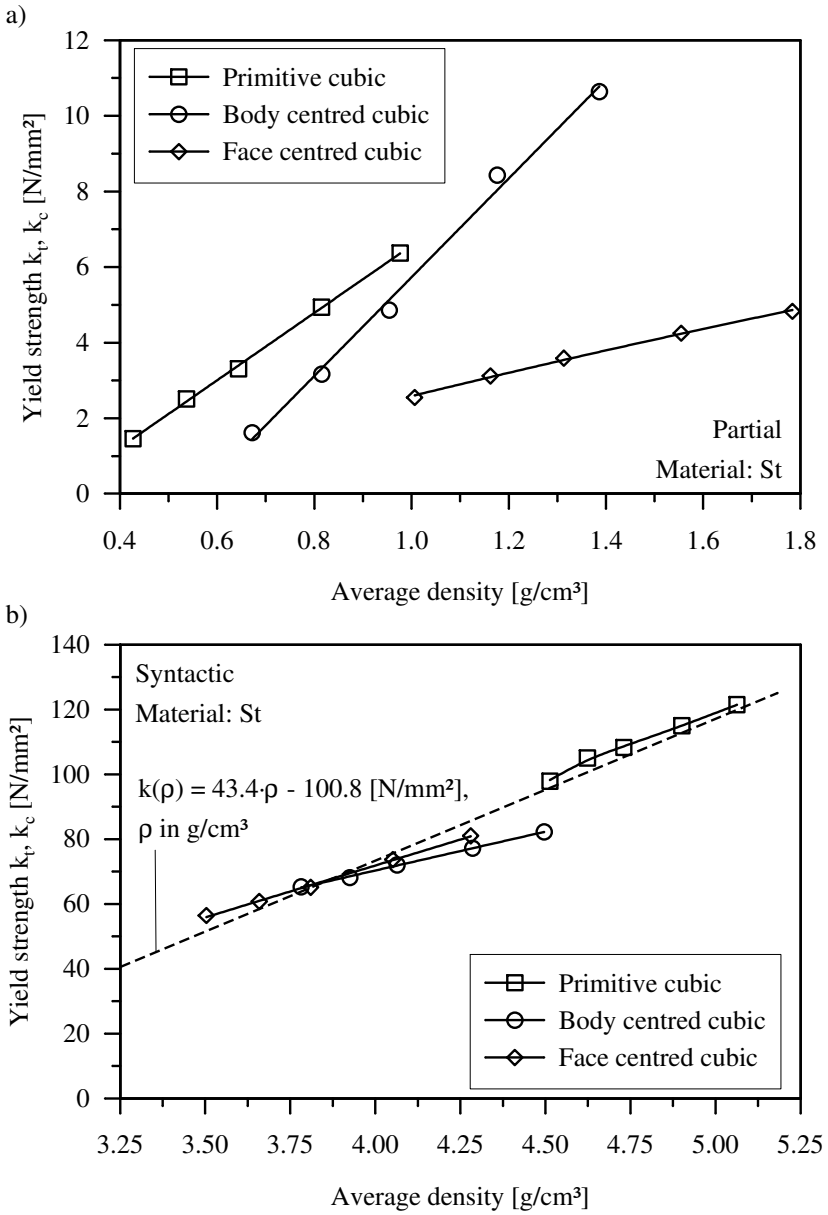

Figure 46: Initial compressive k_c and tensile yield stress k_t of homogeneous MHSS dependence on the average density $\overline{\rho}$ for different topologies: a) Partial, b) Syntactic.

Influence of the sphere material Because of the sintering processing, different sphere wall materials are possible. In order to study the influence of the sphere material on the macroscopic properties of MHSS, the sintered steel alloy is replaced by sintered aluminium. Within the scope of the FE analysis, this substitution is easily achieved by modifying the material model of the sphere material. The mechanical properties of the sample of sintered aluminium are given in Table 4. In order to restrict the complexity of the investigation, only the sphere wall thickness $t = 0.075$ mm is considered.

In Figure 47 the stress relations of partial aluminium MHSS are plotted. For reasons of comparison, two curves representing MHSS with sintered steel spheres are added. It should be noted here that the average densities $\overline{\rho}$ of the structures are different, but their geometric dimensions of the hollow spheres and connecting elements are identical in all cases. It can be observed that the joining technology, namely sintering or adhesive bonding, has only a minor impact on the material behaviour of the aluminium MHSS Al/Al and Al/Ep. Only within the elastic area can a small deviation be observed. The steel structures St/St and St/Ep exhibit significantly higher stress levels than the aluminium MHSS. This behaviour is reflected in the material

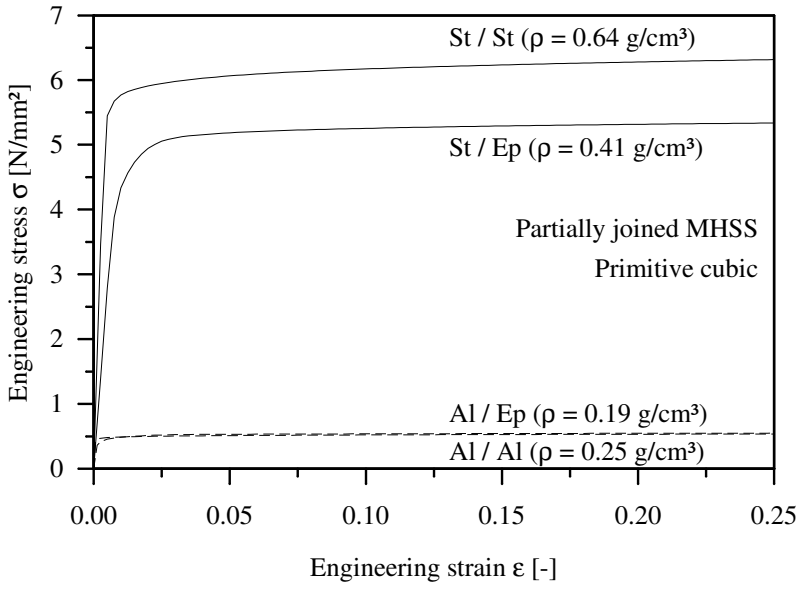

Figure 47: Stress-strain relations of partial aluminium MHSS.

parameters. Figure 48 displays the dependence of Young's modulus E on the average density $\overline{\rho}$ for partial MHSS. In the following figures, the results of steel MHSS are included and drawn by dashed lines in order to directly compare the different sphere wall materials. Sintered and adhesively bonded aluminium structures are considered. Since the material parameter E is plotted versus the average density, structures with high specific stiffness are located in the top left area. Accordingly, the sintered Al/Al

- structures exhibit the highest specific stiffness. The explanation is the high specific stiffness of sintered aluminium which exceeds the value of sintered steel by approximately 30 %. The better performance of the sphere wall material also improves the mechanical behaviour of the structure. In the case of adhesively bonded structures, the influence of the sphere wall material is small and the values for E lie within the range of adhesively bonded steel structures. Here, the low Young's modulus of the epoxy resin limits the stiffness of the structure. The results of the finite element anal-

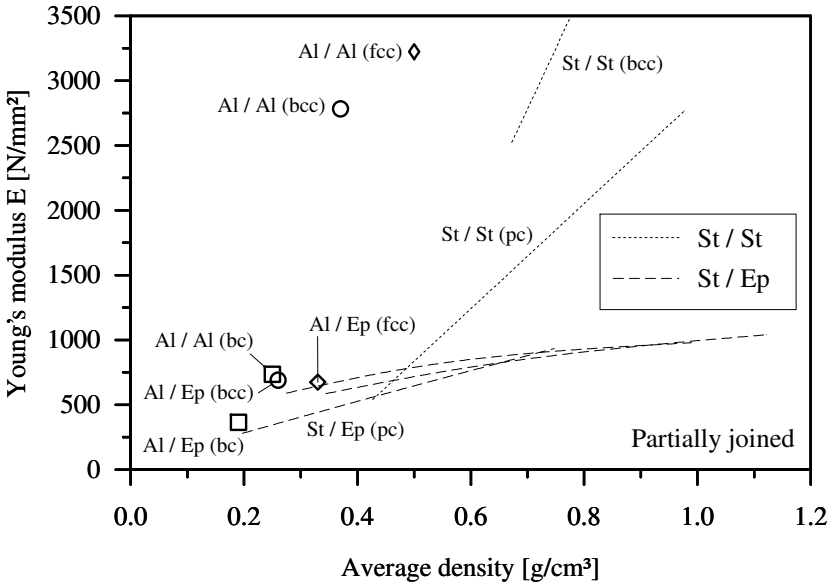

Figure 48: Influence of the sphere material on Young's modulus of partial MHSS (Dashed lines taken from Fig. 40 a), dotted lines taken from Fig. 45 a)).

ysis of aluminium MHSS are summarised in Table III in Appendix A. There, it can be seen that the second elastic parameter, Poisson's ratio ν, only slightly changes after substituting the sphere wall material. This can be explained by the similar Poisson numbers of the compared sphere materials (Al: $\nu = 0.34$, St: $\nu = 0.3$).

In Fig. 49 the initial yield stresses k_t and k_c of partial MHSS are plotted versus the average density. The results of partial steel MHSS are added from Figs. 41 and 46 a). Significantly lower values are obtained for aluminium MHSS. The explanation is the low yield stress of the sintered aluminium. With $k = 24$ N/mm^2, its yield stress reaches only 8% of the corresponding value of the sintered steel. This deviation also distinctly decreases the yield stresses of the structure. Due to the low yield stress of the sintered aluminium, plastification always starts inside the aluminium spheres and not inside the anisotropic epoxy matrix. Therefore, no dependency on the loading direction is observed.

Similar results are obtained for syntactic morphology. Analogous to the partial MHSS, the stress-strain relations (cf. Fig. 50) show higher stress levels for the steel

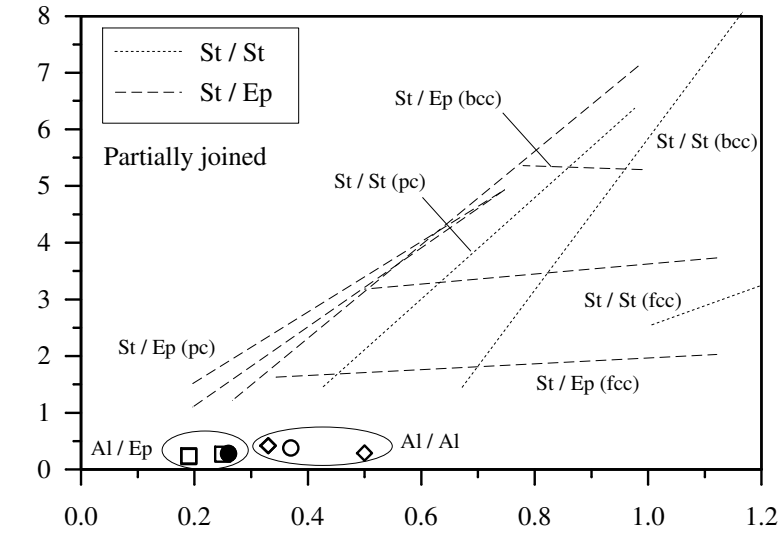

Figure 49: Influence of the sphere material on the initial yield stresses of partial MHSS (Dashed lines taken from Fig. 41, dotted lines taken from Fig. 46 a)).

structures. However, the higher yield stress of the adhesive ($k_t = 61.5$ N/mm^2) in comparison to the aluminium ($k_t = 24$ N/mm^2) improve the mechanical properties of the adhesively bonded aluminium MHSS (Al/Ep) and similar results as for the St/Ep (steel: $k_t = 300$ N/mm^2) structure are obtained.

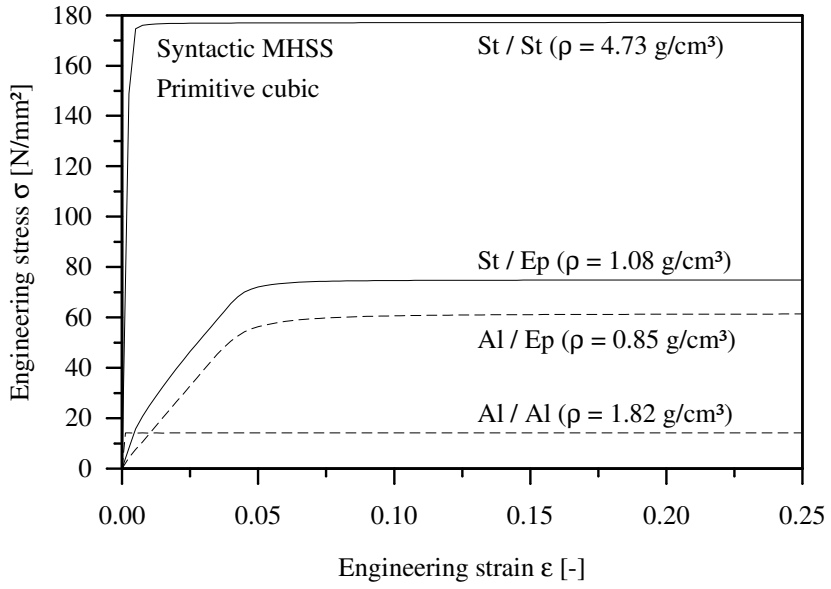

Figure 50: Stress-strain relations of syntactic aluminium MHSS.

Figure 51 shows Young's modulus E plotted versus the average density $\overline{\rho}$. The data of the syntactic steel MHSS is added from Figs. 40 and 45. As already observed

for partial MHSS, higher specific values are obtained for the homogeneous Al/Al-structures. The adhesively bonded Al/Ep-structures exhibit similar stiffness as the adhesively bonded steel MHSS. Poisson's ratio exhibits no clear dependence on the sphere wall material (cf. Appendix A). Analogous to the partial MHSS, the low yield

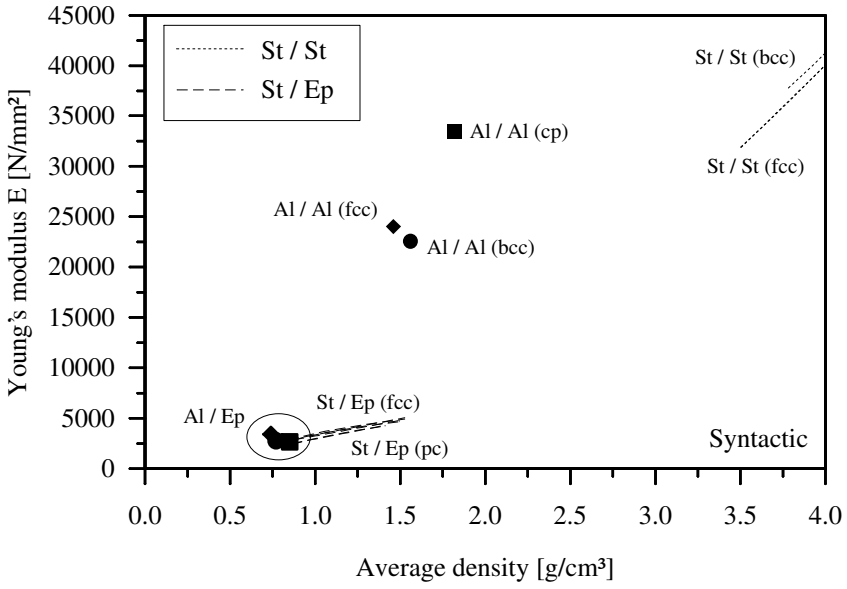

Figure 51: Influence of the sphere material on Young's modulus of syntactic MHSS (Dashed lines taken from Fig. 40 b), dotted lines taken from Fig. 45 b)).

stress of the sintered aluminium significantly decreases the yield stresses k_c and k_t. Figure 52 shows that the specific values of the aluminium structures lie well below the results of the steel MHSS.

In conclusion, MHSS show a strong dependence on the applied sphere material. High specific values of this material are reflected in improved mechanical performance of the whole structure. Only in the case of adhesively bonded MHSS, is the stiffness widely independent of the sphere wall material. Here, the low Young's modulus of the epoxy resin is the limiting factor for the stiffness of the compound.

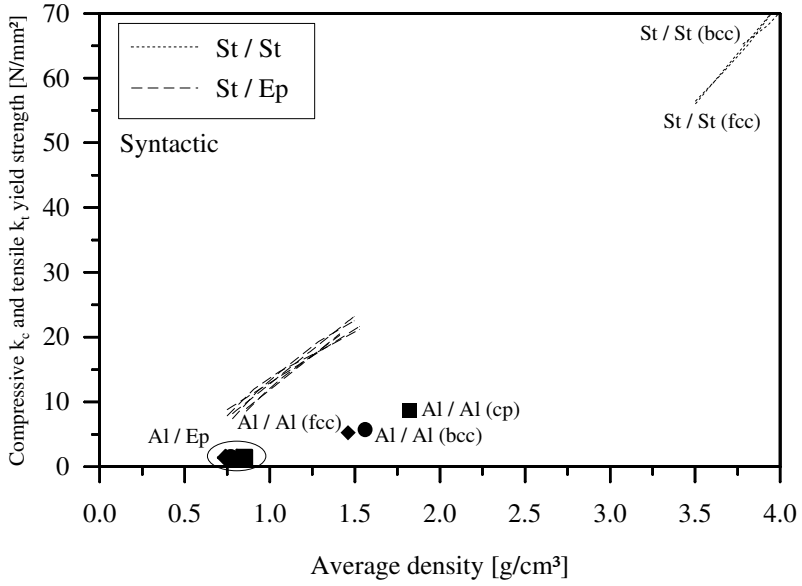

Figure 52: Influence of the sphere material on the initial yield stress of syntactic MHSS (Dashed lines taken from Fig. 41, dotted lines taken from Fig. 46 b)).

Yield surface Figures 9 and 10 show the yield surfaces of the VON MISES and modified VON MISES yield condition. The VON MISES (or TRESCA) yield condition is usually utilised to describe the flow behaviour of classical dense metallic materials. In contrast to the VON MISES yield condition, the yield surfaces of porous materials exhibit a dependency on the hydrostatic stress state [116]. In the following, the shape of the yield surface of adhesively bonded steel MHSS inside the principal stress space will be determined under the assumption of isotropic material behaviour of the steel alloy and the epoxy resin. In order to consider the investigated MHSS structures (cf. Figs. 21 a) and 23 a)) which reveal cubic symmetries despite their principally orthotropic characteristic as an isotropic solid, normal stresses need to be applied in the same principal material system. For our studies, the 0°-coordinate system (cf. Fig. 7 a)) has been chosen (another possibility would be a principal system which can be obtained by rotating all axes by 45°, cf. Fig. 7 b)). By applying the normal stress states only in the same principal material system, the classical relationships for isotropic solids (e.g. that the shear modulus can be calculated from Young's modulus and Poisson's ratio) remain valid [23]. Two primitive cubic geometries with the sphere wall thickness $t = 0.075$ mm and a minimum distance $d_{\min} = 0.18$ mm between neighboring spheres are considered. The average densities of the structures are $\overline{\rho} = 0.49$ g/cm^3 (partial) and $\overline{\rho} = 1.27$ g/cm^3 (syntactic).

To determine the shape of the yield surface, multiaxial stress states are simulated by modifying the boundary conditions shown in Fig. 25. The reflective boundary conditions are replaced by time dependent displacements $u_i(t)$ which allow the simultaneous loading of the structure in three perpendicular loading directions. In Fig. 53 the shape of the yield surface in the corresponding deviatoric plane is drawn according to the following transformation which projects a principal stress state first in the octahedral plane (angle of transformation: $\cos\vartheta = 1/\sqrt{3}$) and then to the Cartesian coordinate system (x, y).

$$y = \frac{2}{\sqrt{6}} \cdot (\sigma_I - 0.5(\sigma_{II} + \sigma_{III})) \ , \tag{69}$$

$$x = \frac{1}{\sqrt{2}} \cdot (\sigma_{III} - \sigma_{II}) \ . \tag{70}$$

Here, it is now essential whether the plastic behaviour is pressure sensitive, i.e. depends on J_1^{o}, or not. If there is no dependency on J_1^{o}, i.e. a constant shape along the hydrostatic axis, then all evaluated stress states can be drawn in a single octahedral plane. However, if one can expect a dependency on the hydrostatic stress, then only stress states with the same hydrostatic stress are allowed to be represented in the same octahedral plane where $J_1^{\mathrm{o}} = \text{const}$ holds. As a result, e.g. uniaxial tensile ($J_1^{\mathrm{o}} = \sigma_I$) and pure shear tests ($J_1^{\mathrm{o}} = 0$) cannot be represented in the same octahedral plane.

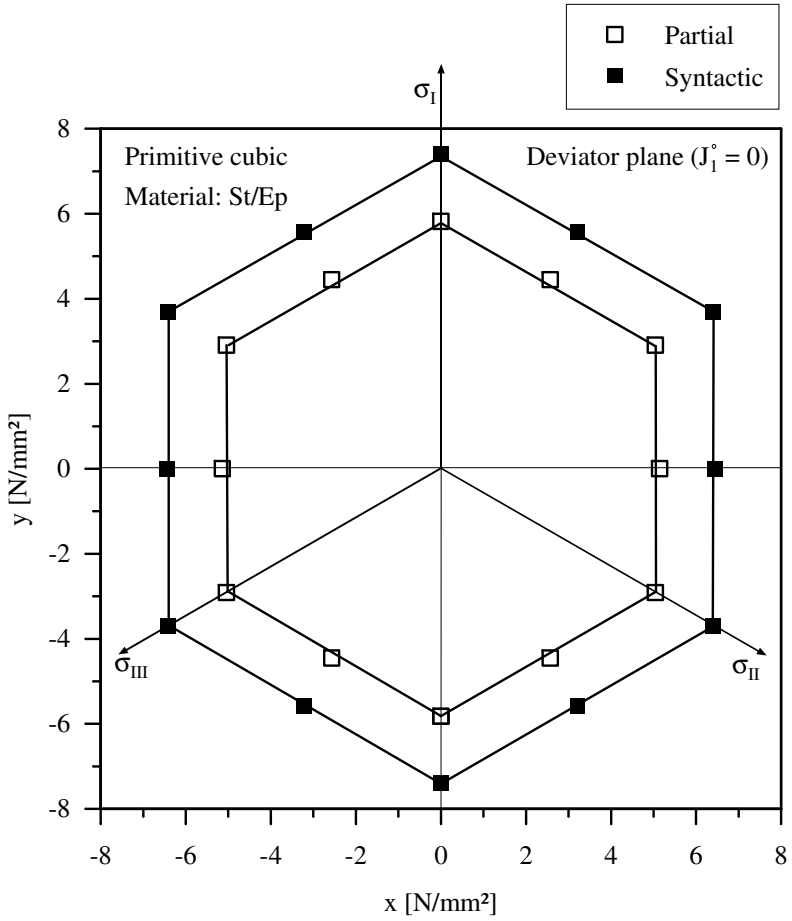

Figure 53: Cross section of the yield surfaces of a primitive cubic MHSS in the deviatoric plane.

In order to draw the shape of the yield surface for the pressure sensitive material under consideration, differing multiaxial stress states with $J_1^o = 0$, e.g. $\sigma_I = -\sigma_{II}$ ($\sigma_{III} = 0$) or $\sigma_I = -2 \cdot \sigma_{II} = -2 \cdot \sigma_{III}$ ($\sigma_I > 0 \vee \sigma_I < 0$), are realised and the corresponding yield stresses are drawn in the deviatoric plane, cf. Fig. 53. These regular hexagons correspond to the outer bound of a convex yield condition in the octahedral plane, [76]. The points indicated by filled squares ■ in Fig. 53 result from the finite element simulation of syntactic MHSS, whereas the □ symbols indicate the result of partial structures. The larger area enclosed by the yield surface of the syntactic MHSS indicates higher yield stresses of this material. It should be noted here that these shapes change only their size along the hydrostatic axes but remain similar in a mathematical sense.

To clarify the influence of the hydrostatic stress on the yield surface, sectional views through planes along the hydrostatic axis for $\theta = 0° \vee 60°$ are presented in Fig. 54. In this figure, the so-called Haigh-Westergaard coordinates $J_1^o - \sqrt{2J_2'}$ are applied

in order to investigate the convexity of the yield surfaces (i.e. a direct consequence of DUCKER's stability postulate). In such a coordinate system, a straight line is obtained for partial MHSS and an approximately parabolic curve for syntactic MHSS. Consequently, the convexity condition is fulfilled. By comparing the sectional views of the yield surfaces, it becomes clear that partial MHSS exhibit a distinct dependency of the yield stress on the hydrostatic pressure. However, syntactic structures also show a dependence on the hydrostatic stress state and therefore e.g. the VON MISES yield condition is not suitable for the modelling of the material behaviour of MHSS under multiaxial stress states.

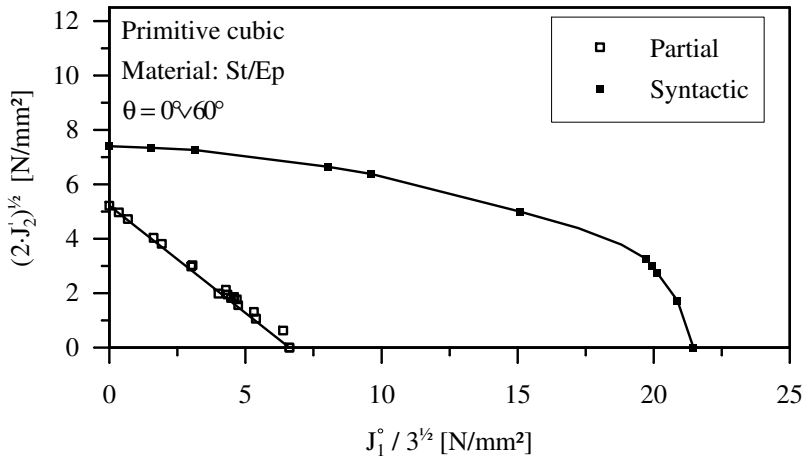

Figure 54: Dependency of the yield surfaces of primitive cubic MHSS on the hydrostatic stress state.

Figure 55 illustrates the shape of the yield surface of the partial MHSS in the principal stress space. The surface corresponds to a double-sided pyramid which is generated by twelve plane surfaces. In comparison to the yield surface of the syntactic structure (cf. Fig. 56), the circumference of the partial MHSS is smaller. These observations correspond to the findings of the numerical and experimental analyses of the uniaxial testing, where the syntactic MHSS show higher yield stresses at the same sphere geometry.

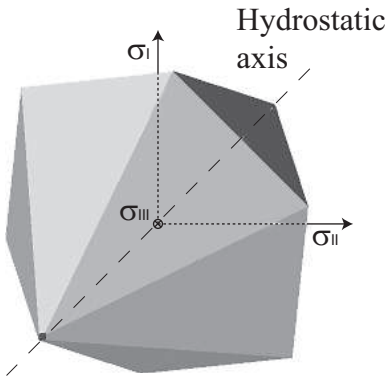

Figure 55: Yield surface of a primitive cubic partial MHSS.

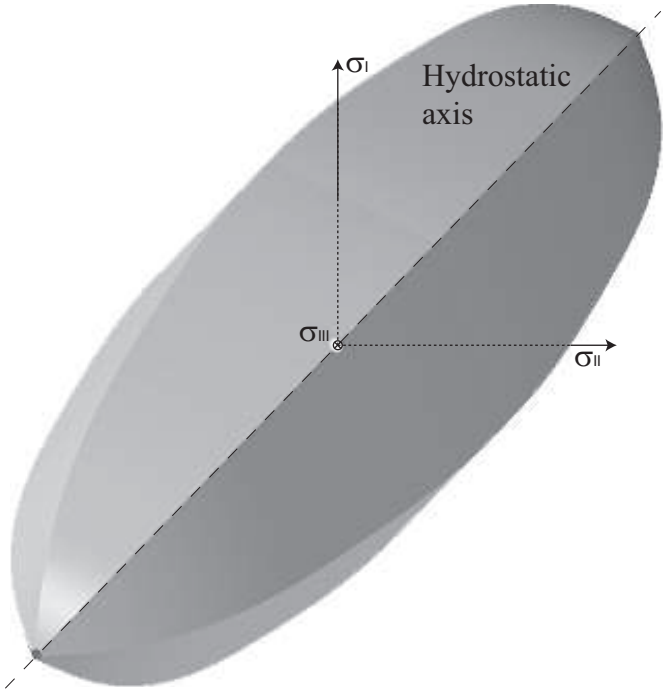

Figure 56: Yield surface of a primitive cubic syntactic MHSS.

Investigation of the isotropy Up to this point, all forces are applied in the same principal material coordinate system and Young's modulus E, Poisson's ratio ν and the initial yield stresses k_c and k_t were determined. In Section 2.1.1 it is shown that the complete formulation of the elasticity tensor of cubic symmetrical geometries requires the incorporation of a third elastic constant G^{45^o}. For isotropic materials, this third elastic constant can be calculated based on Young's modulus and Poisson's ratio according to $G = G^{45^o} = E/(2 + 2 \cdot \nu)$. In the case of geometries exhibiting cubic symmetry, a second set of finite element models is required where two of the loading planes are rotated by an angle of 45^o about e.g. the y-axis [74] (cf. Figs. 7, 22 and 24). Compressive testing is simulated and the elastic parameters E^{45^o} and ν^{45^o} of these models are determined. The results will be shown for the example of adhesively bonded structures, but similar results are obtained for sintered and casted MHSS.

First, partial MHSS are considered. The elastic parameters of the default (0°) and rotated (45°) loading planes are plotted versus the average density in Fig. 57. Young's modulus is represented by the full line and no significant dependence on the loading direction can be observed. In the case of Poisson's ratio a small deviation is visible at low densities. However, this deviation disappears quickly with increase of density.

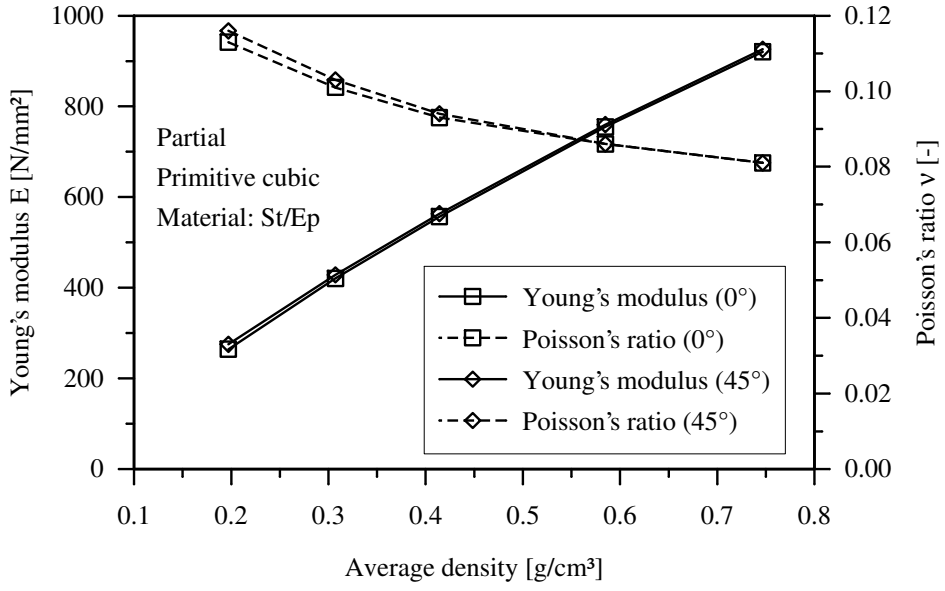

Figure 57: Elastic properties for different orientations of the loading planes (partial).

Based on these numerical findings, the shear moduli G and G^{45^o} are determined according to $G = E/(2 \cdot (1 + \nu))$. The ratio G/G^{45^o} can be interpreted as an indicator for the anisotropy of the material. A completely isotropic material will have a ratio of $G/G^{45^o} = 1$, any deviation from this value signals anisotropic behaviour. Based on the results shown in Table 7 it can be concluded that primitive cubic and partial MHSS can be regarded as isotropic within the linear-elastic range. Figure 58 shows

ρ [g/cm^3]	E [N/mm^2]	ν [–]	G (calc.) [N/mm^2]	E^{45^o} [N/mm^2]	ν^{45^o} [–]	G^{45^o} (calc.) [N/mm^2]	G/G^{45^o} [–]
0.20	264	0.113	119	275	0.116	123	0.967
0.31	420	0.101	191	428	0.103	194	0.985
0.41	557	0.093	255	563	0.094	257	0.992
0.58	754	0.086	347	760	0.086	350	0.991
0.75	921	0.081	426	926	0.081	428	0.995

Table 7: Elastic properties of partial MHSS (St/Ep) for different loading planes.

the initial yield stresses k_c and k_t for the two different loading directions. Slightly higher results are obtained for the default 0^o loading planes, but again the material can be considered as isotropic to a good approximation.

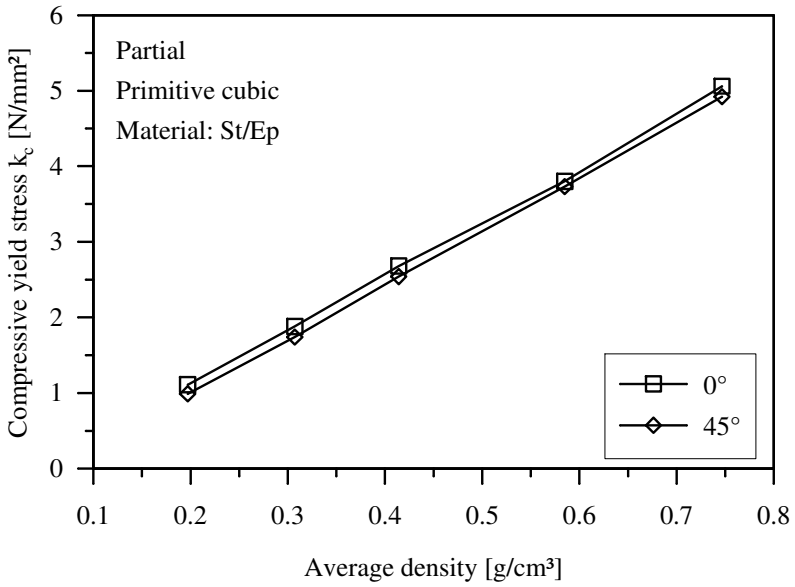

Figure 58: Initial compressive yield stresses for different orientations of the loading planes (Partial).

The same analyses are repeated for a syntactic morphology. The numerical findings for the elastic properties are plotted in Fig. 59. The full and dashed lines for both loading directions representing Young's modulus and Poisson's ratio respectively coincide. Table 8 shows that the material shows isotropic linear-elastic behaviour.

The same result is obtained for the initial compressive yield stress k_t. In the case of the lowest density, a very small deviation is observed, but for higher densities the two curves merge.

Based on these numerical findings it can be concluded that MHSS with a primitive cubic arrangement of spheres can be considered as isotropic in relation to their

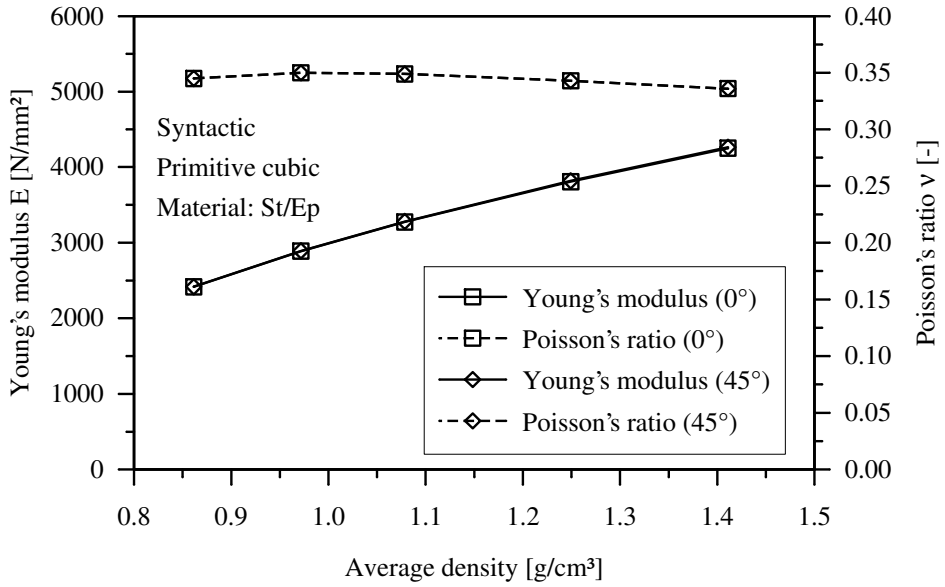

Figure 59: Elastic properties for different orientations of the loading planes (Syntactic).

ρ [g/cm^3]	E [N/mm^2]	ν [–]	G (calc.) [N/mm^2]	$E^{45°}$ [N/mm^2]	$\nu^{45°}$ [–]	$G^{45°}$ (calc.) [N/mm^2]	$G/G^{45°}$ [–]
0.86	2416	0.345	898	2417	0.345	898	1.00
0.97	2888	0.350	1070	2892	0.350	1071	1.00
1.08	3274	0.349	1213	3280	0.349	1216	1.00
1.25	3807	0.343	1417	3817	0.343	1421	1.00
1.41	4250	0.336	1591	4263	0.336	1595	1.00

Table 8: Elastic properties of syntactic MHSS (St/Ep) for different loading planes.

linear-elastic behaviour and uniaxial yield stresses. This result is independent of the morphology or material composition of the structure. It should be mentioned here that this conclusion cannot be transferred to other cubic symmetrical topologies. However, the primitive cubic topology exhibits the highest deviation of the distance of spheres in the dependence on the loading direction. Accordingly, it is likely that body centred cubic and face centred cubic structures behave at least approximately isotropic.

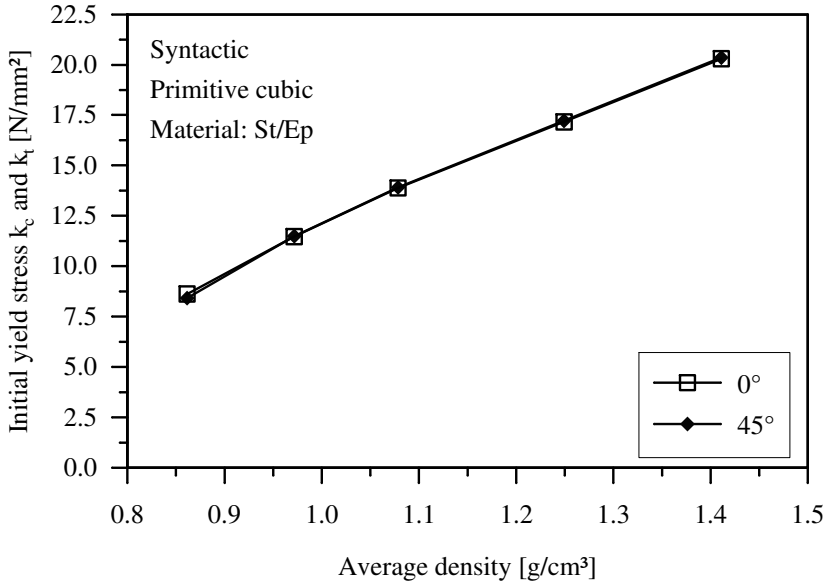

Figure 60: Initial compressive yield stress k_c for different orientations of the loading planes (Syntactic).

4.1.2 Mechanical Properties: Experimental findings

In addition to the numerical analyses, experimental tests on adhesively bonded MHSS are performed. Compressive testing is used to determine Young's modulus E, the plateau stress σ_{pl} and the hardening behaviour of these structures.

Partial MHSS Partial samples with two average densities $\overline{\rho}$ are investigated. The difference in density is caused by varying densities of the sintered sphere wall material; the samples were provided by the German enterprise GLEICH GMBH, Dresden, Germany. Figure 61 shows the stress-strain relation of the MHSS with the lowest density $\overline{\rho} = 0.3$ g/cm^3. The curve exhibits the typical characteristics of a porous material. A linear elastic area is followed by a stress plateau, before the stress rises exponentially during the densification of the structure. The gradient of the curve inside the linear elastic area is equal to YOUNG's modulus E and the elastic zone is confined by the stress peak $\sigma_{\max}$. Within the stress plateau, the stress level is approximately constant and indicated by the plateau stress σ_{pl}. After reaching the densification strain ε_{D} the porosity in the MHSS decreases rapidly and the stress increases. In addition to the experimental data, the Fig. 61 contains results of the finite element analysis. The best agreement between numerical and experimental data is found for the primitive cubic arrangement of spheres. This finite element model corresponds to a structure with an average density $\overline{\rho} = 0.31$ g/cm^3.

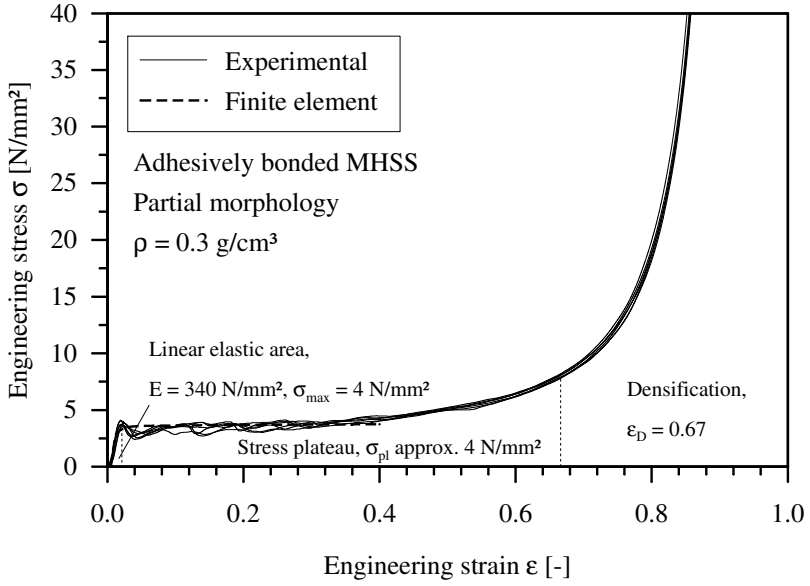

Figure 61: Stress-strain relation of low density partial MHSS.

However, the numerical analysis requires several simplifications which do not allow for the incorporation of all physical effects that occur in the experimental tests. In

contrast to the results of the finite element analysis, the measured stresses inside the plateau are not constant and oscillate around the plateau stress. Furthermore, the experimental curves exhibit an initial stress peak $\sigma_{\max} > \sigma_{\mathrm{pl}}$ at the end of the linear elastic area. This behaviour is caused by the failure mechanism in partial MHSS. The plastic deformation is concentrated inside bands which collapse after a critical strain is exceeded, each time coinciding with a macroscopic stress oscillation. Thereby, the weakest hollow spheres collapse first and initiate the collapse band. The majority of these bands form an angle of approx. 30-40^o with the loading direction as shown in Fig. 62. The first collapse band weakens the structure so that the plateau stress σ_{pl} is distinctly smaller than the initial stress peak $\sigma_{\max}$. This effect is not observed in the numerical analysis, since the symmetry boundary conditions do not allow for the formation of collapse bands.

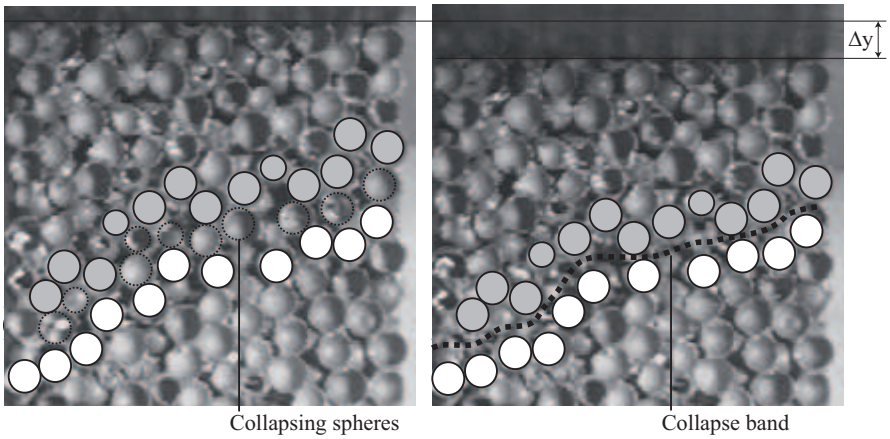

Figure 62: Collapse bands in a partial MHSS.

Figure 63 shows the result of the experiments with high density partial MHSS ($\overline{\rho} = 0.6$ g/cm^3). The figure exhibits the same characteristics as the low density material, but distinctly higher stress levels can be observed. Young's modulus increases from 340 to 730 N/mm^2, the initial stress peak $\sigma_{\max}$ from 4 to 11 N/mm^2 and the plateau stress from 4 to 9 N/mm^2. Only, the densification strain ε_{D} remains approximately constant.

In Table 9 the experimental results are compared to the numerical findings. Based on the average density $\overline{\rho}$ of the experimental specimens the finite element models with similar densities are chosen. Good agreement is found for primitive cubic and body centred cubic topologies. The numerical results of the face centred cubic MHSS exceed the experimental values.

Syntactic MHSS The syntactic MHSS specimens are manufactured at the University of Aveiro, Portugal, by pouring single hollow spheres into a mould and adding an epoxy resin to the fill. Two types of hollow spheres with differing densities of the

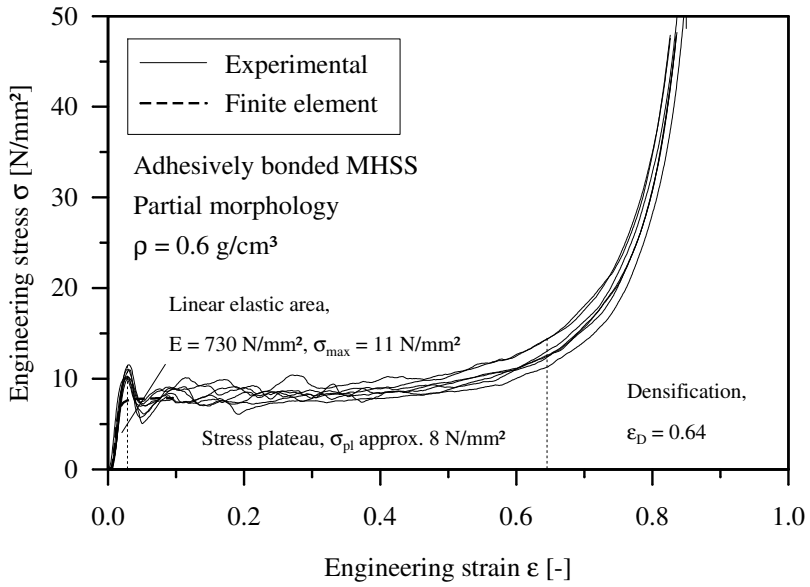

Figure 63: Stress-strain relation of high density partial MHSS.

Parameter	Density [g/cm^3]	Experimental	Finite Element Method		
			pc	bcc	fcc
Young's	$\overline{\rho} \approx 0.3$	340 N/mm^2	380 N/mm^2	580 N/mm^2	570 N/mm^2
modulus	$\overline{\rho} \approx 0.6$	750 N/mm^2	750 N/mm^2	830 N/mm^2	830 N/mm^2
Plateau	$\overline{\rho} \approx 0.3$	4 N/mm^2	3.7 N/mm^2	4.6 N/mm^2	7.0 N/mm^2
stress	$\overline{\rho} \approx 0.6$	8 N/mm^2	7.9 N/mm^2	9.8 N/mm^2	14 N/mm^2

Table 9: Comparison of experimental and numerical results.

sintered steel are used. The higher density spheres exceed the density of the epoxy resin and consequently remain at the bottom of the mould after the epoxy resin is added. In comparison, the manufacturing process for the low density spheres is more complex, since the hollow spheres float in the epoxy resin. Accordingly, a stopper at the top of the mould is required in order to press the spheres into the epoxy resin. This procedure carries the risk of creating air cavities inside the epoxy matrix which would deteriorate the macroscopic properties. Besides, a denser packing of the spheres can be observed for this manufacturing technique. The obtained syntactic MHSS blocks are first cut with a band-saw and then machined on a CNC-machine to their final dimensions.

The results of the low density syntactic MHSS ($\overline{\rho} = 0.75$ g/cm^3) are shown in Fig. 64. The characteristics of the curve are similar to Figs. 61 and 63. In contrast to the partial specimens, the observed Young's modulae and stress levels are distinctly higher. Furthermore, because of the lower porosity of syntactic MHSS the densification starts at slightly lower strains ε_{D}. The comparison of the numerical and experimental

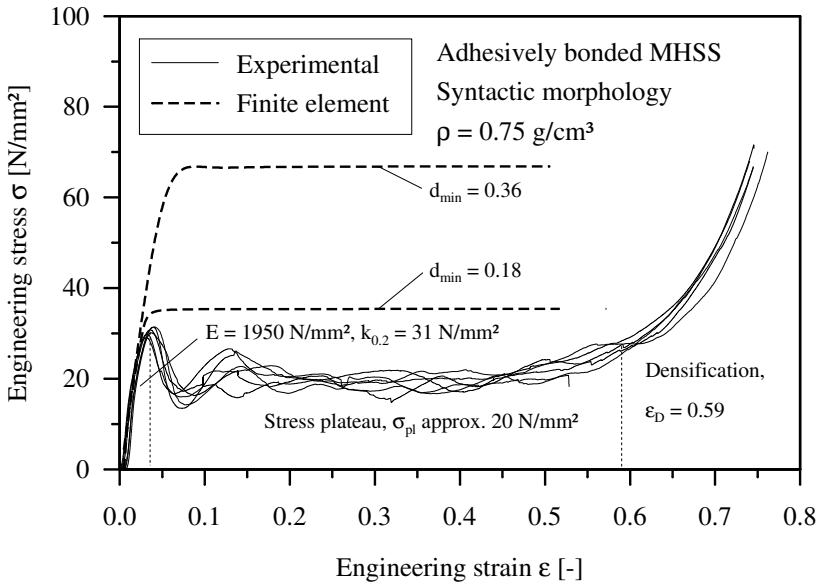

Figure 64: Stress-strain relation of low density syntactic MHSS.

findings yields poor agreement for the default minimum distance $d_{\min}$ between two neighboring spheres (cf. Section 3.1.2) of 0.36 mm. The numerical results show distinctly higher stress levels than observed in the experimental tests. As mentioned above, the required manufacturing process for the low density spheres causes a denser packing of the spheres and decreases the distance between the spheres. Accordingly, a special finite element model with a reduced minimum distance $d_{\min} = 0.18$ mm is generated ($\overline{\rho} = 0.78$ g/cm^3) for the primitive cubic topology. The comparison of the numerical results of this model with the experimental findings still only yields good agreement at small strains. At higher strains, the stress of the numerical solution remains constant whereas the real stresses drop towards the plateau stress σ_{pl}. The explanation for this deviation is the failure mechanism in syntactic MHSS which cannot be captured in the numerical model. In Fig. 65 a low density syntactic specimen is shown under compressive loading at two different strains. After reaching a critical strain, the geometry shears along a sliding band which forms an angle of approx. 45^o with the loading direction. The simulation of this phenomenon in the numerical investigation requires the modelling of the whole geometry and exceeds the capacity of the available computer hardware.

The increase of the average density of syntactic MHSS from $\overline{\rho} = 0.75$ g/cm^3 to $\overline{\rho} = 1.2$ g/cm^3 yields a rise of Young's modulus E to 2320 N/mm^2. Furthermore, the initial stress peak $\sigma_{\max} = 60$ N/mm^2 and the plateau stress $\sigma_{\text{pl}} = 40$ N/mm^2 are doubled. The corresponding stress-strain relations are given in Fig. 66. In addition, the results of the finite element analysis are added for the primitive cubic topology and the default distance $d_{\min} = 0.36$ mm. Again, good agreement is found within the

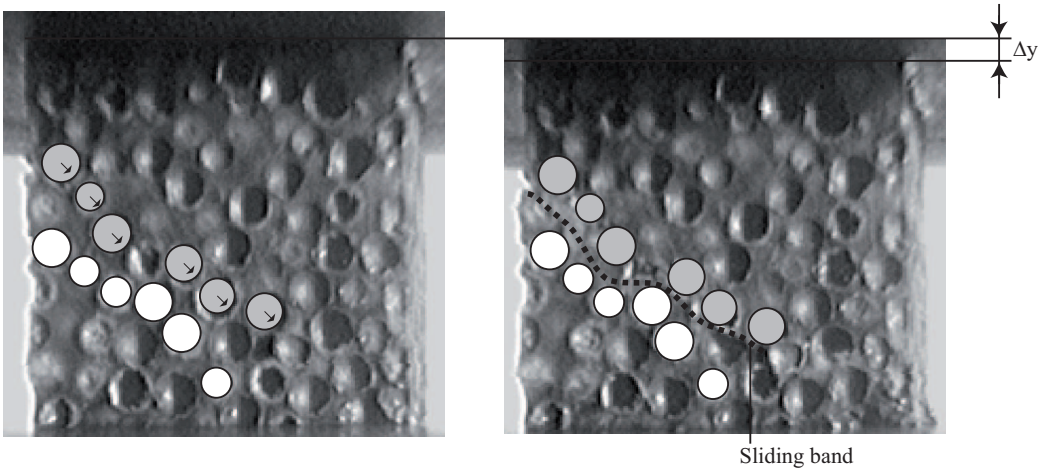

Figure 65: Sliding bands in a syntactic MHSS.

elastic range, but the decrease of the stresses from $\sigma_{\max}$ to σ_{pl} due to sliding is not captured by the finite element model.

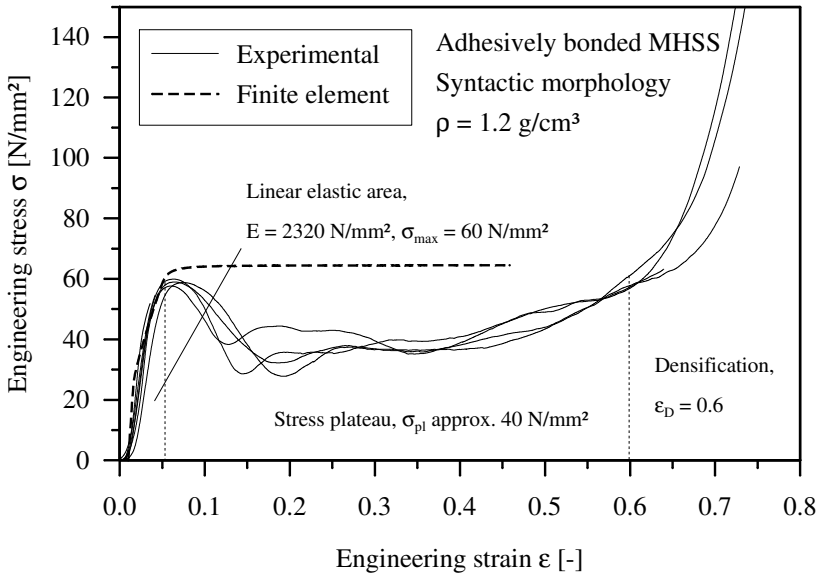

Figure 66: Stress-strain relation of high density syntactic MHSS.

Interpretation of the experimental findings In Fig. 67 the experimental results of all specimens are plotted. In accordance to the numerical findings, the stiffness and stress levels increase with the average density $\overline{\rho}$. The densification strain decreases for syntactic morphology. This phenomenon is caused by the lower porosity of the syntactic MHSS.

Within the field of lightweight construction, specific material properties (in the

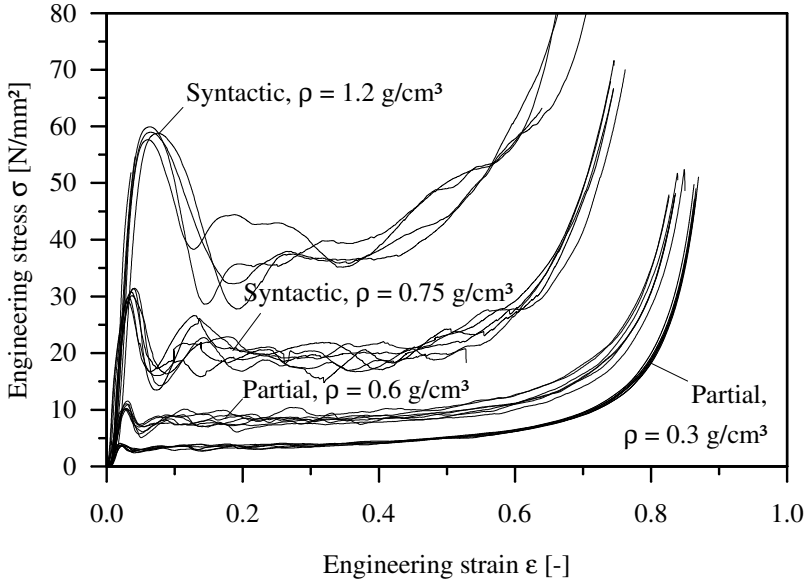

Figure 67: Stress-strain relation of high density syntactic MHSS.

following indicated by the superscript symbol *) are of great interest. Thereby, the respective material parameter is divided by the average density $\overline{\rho}$ of the structure. Table 10 shows these values for partial and syntactic MHSS. The maximum specific stiffness E^* can be observed for the syntactic MHSS with the density $\overline{\rho} = 0.75$ g/cm^3. The specific stiffness of partial MHSS shows only a weak dependence on the density. In the case of the specific stresses $\sigma^*_{\max}$ and σ^*_{pl}, the maximum values are observed for the high density syntactic MHSS. In conclusion, the syntactic MHSS outperform the partial structures concerning the specific properties. It should be mentioned here, that these specific values are only valid for compressive loading and must be investigated separately for different loading conditions.

	Partial MHSS		Syntactic MHSS	
	$\overline{\rho} = 0.3$ g/cm^3	$\overline{\rho} = 0.6$ g/cm^3	$\overline{\rho} = 0.75$ g/cm^3	$\overline{\rho} = 1.2$ g/cm^3
$E^* = E/\overline{\rho}$	1130	1216	2600	1930
$\sigma^*_{\max} = \sigma_{\max}/\overline{\rho}$	13.3	18.3	41.3	50
$\sigma^*_{\mathrm{pl}} = \sigma_{\mathrm{pl}}/\overline{\rho}$	13.3	15	26.7	33.3

Table 10: Specific material properties of MHSS [N·mm/kg].

4.1.3 Mechanical Properties: Impact Behaviour

Cellular materials have a characteristic stress-strain relationship under compressive loading, which can be divided into four main areas (cf. Fig. 68): (i) linear-elastic

response, (ii) transition zone, (iii) stress plateau and (iv) densification. After initial quasi-linear elastic response (Young's modulus E), where the elastic deformation of the cell walls occurs, the cellular materials first experience buckling, plastic deformation and collapse of intercellular walls in the transition zone, started by k_c. Under further loading the mechanism of buckling and collapse becomes even more pronounced, which is manifested in large strains at almost constant stress. The stress σ_{pl} indicates the beginning of this plateau and the gradient of the stress plateau is denoted by the plateau modulus P. After reaching a critical strain ε_{D}, the high compression of the porous material causes a densification of the structure and the stress level increases exponentially. A similar behavior can be observed under impact loading. During the

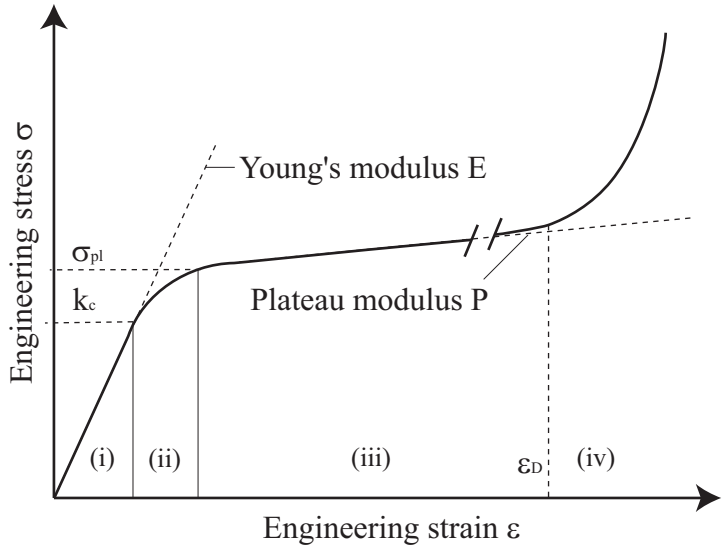

Figure 68: Schematic drawing of the stress-strain behaviour of porous materials under impact loading.

loading process the cellular material is able to accumulate a significant amount of the impact energy through its deformation, which is represented by the area under the strain-stress curve. The absorbed energy is a sum of the energy accumulated during elastic deformation and the energy absorbed by the plastic deformation. The latter is very important for crash energy absorption. It is important to note that energy absorption is strain-rate dependent (cf. Fig. 11). Generally, the capability of impact energy absorption increases with increasing strain-rate sensitivity ($m > 0$). However, according to Shim et al. [117, 118] the energy absorption capacity is decreased if the cells are damaged.

Within the scope of the finite element computational analysis three different geometries with cubic symmetries were considered. The primitive cubic (pc), body centred cubic (bcc) and face centred cubic (fcc) finite element models are visualised in Fig. 21. The MHSS behaviour under uniaxial impact loading conditions was analysed using

the explicit finite element code LS-DYNA [83, 77, 119, 120] and boundary conditions according to Fig. 25 were prescribed. Additionally, the pore surface elements were defined as one contact group to account for self-contact at very large deformations. The coefficient of friction was set to 0.1. As described in Section 2.1, a linear-elastic / ideal-plastic (VON MISES yield condition) material model is employed for the definition of the material properties. Thereby, the metallic shells are sintered steel and the matrix simulates the epoxy resin. Furthermore, the strain rate effects of the plastic behavior were also considered by implementing the COWPER-SYMONDS constitutive relation (21). The accounted COWPER-SYMONDS parameters for steel and adhesive were set as C = 40.4 s^{-1}, p = 5 and C = 1050 s^{-1}, p = 3.7 respectively [84, 120].

In the following, the results of the parametric finite element computational simulations using the above described models are discussed. The behaviour of composite hollow sphere structures with primitive cubic and body centred cubic arrangement under compressive loading is represented in Fig. 69. The deformation of the structures is visualised for five different engineering strains $\varepsilon = 0, 0.15, 0.30, 0.45$ and 0.6. Bending of the spherical shells is predominant at low strains ($\varepsilon < 0.15$). With increasing strain ($\varepsilon \approx 0.30$) the cell walls start to buckle. In the case of face centred cubic structures, a distinct shear deformation within the adhesive matrix can be observed. This deformation is concentrated in the centre of the outer surfaces of the geometries shown, whereas the rest of the matrix remains almost undeformed. Further increase of the strain triggers a collapse of the cell walls ($\varepsilon \approx 0.45$). At large strains ($\varepsilon > 0.50$) the inner surfaces of the metallic shells touch and the stiffness of the structure distinctly increases (compared to Fig. 68, area (iv)). It is clear that the contact area of the face centred cubic arrangement is much larger in comparison to primitive cubic arrangements. This explains the sudden increase of the stress as shown in Figs. 72 and 73.

First, primitive cubic MHSS and a strain rate of $\mathrm{d}\varepsilon/\mathrm{d}t = \dot{\varepsilon} = 1000\ s^{-1}$ are considered. Strain rates of approximately 10 to 500 s^{-1} are typical for high velocity automotive impacts, higher strain rates occur e.g. in aircraft crashes or caused by explosions. In Fig. 70 three curves related to different sphere wall thicknesses t are plotted. The stress-strain behaviour of the composite exhibits a typical characteristic of a porous material. The initial linear-elastic behaviour is followed by a transition zone which yields into the stress plateau. Oscillations of the stress plateau due to sphere walls buckling are observed at the strain $\varepsilon \approx 0.25$. At the critical strain $\varepsilon_D = 0.53$ the inner surfaces of the spherical shell touch and the stress increases. Increase of the sphere wall thickness results in rise of the stress level. Figure 71 shows the strain rate dependency of primitive cubic MHSS. The maximum strain rate $\dot{\varepsilon} = 1000\ s^{-1}$ coincides with the highest observed stresses within the plastic range. Decrease of the strain rate results in decrease of these stresses. Therefore, it can be concluded that the MHSS capability of energy absorption increases with the strain rate and therefore promises

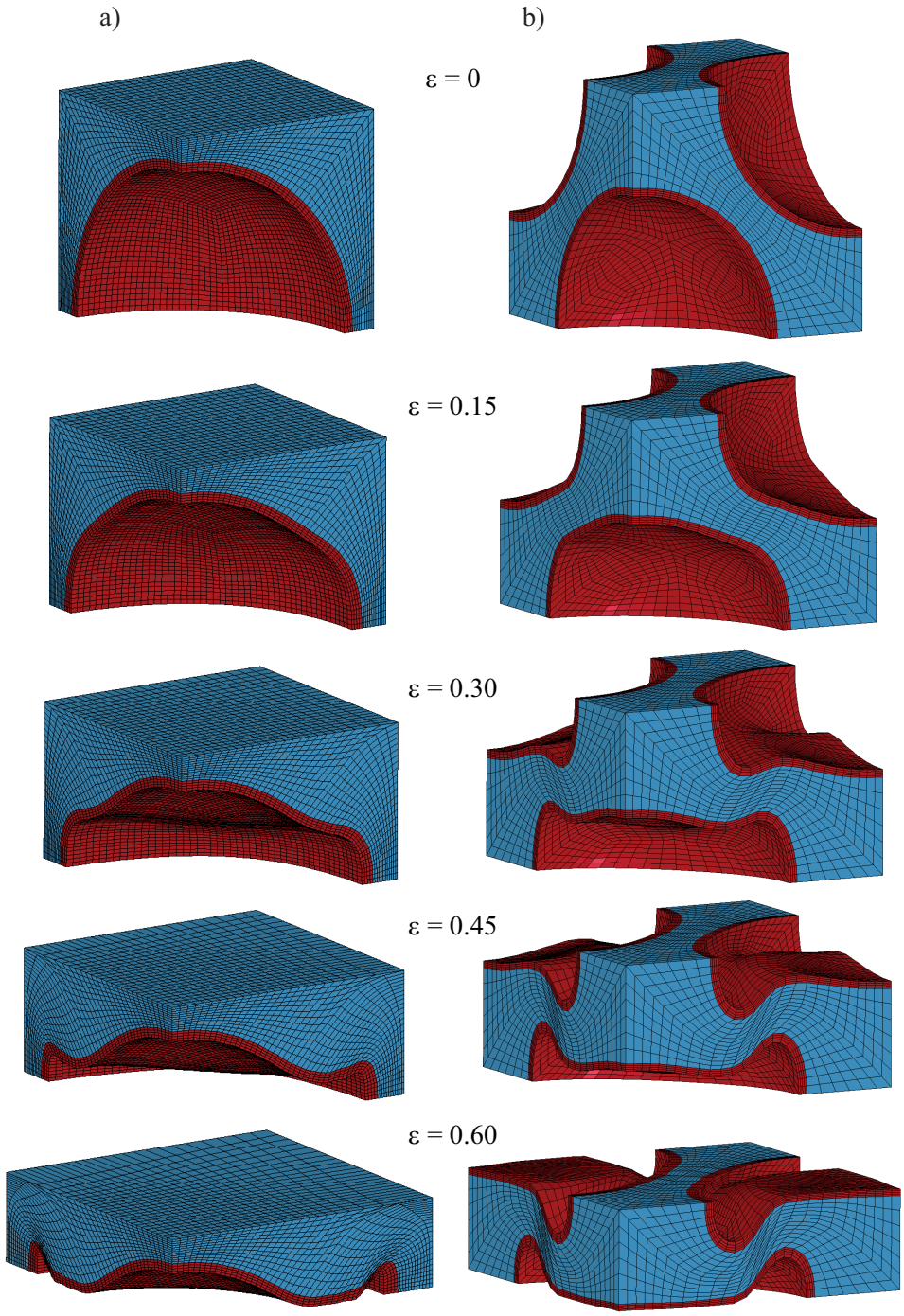

Figure 69: Deformation of composite hollow sphere structures under compressive dynamic loading: a) primitive cubic, b) face centred cubic.

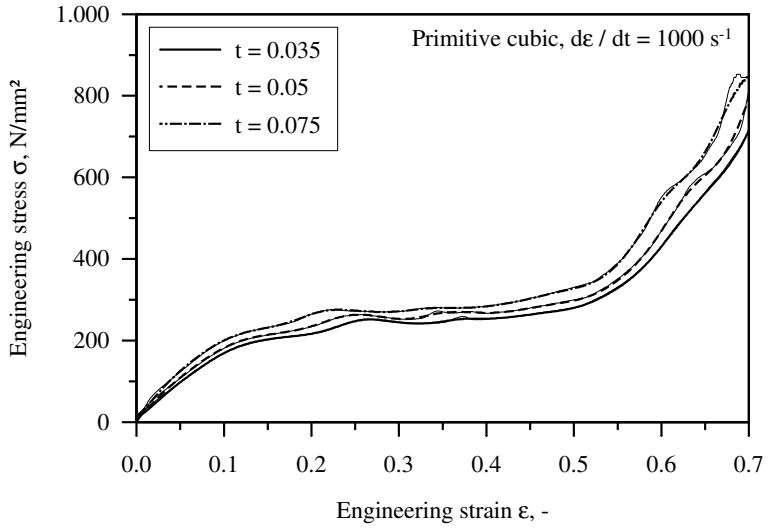

Figure 70: Macroscopic stress-strain relations of primitive cubic MHSS.

to be a suitable application in for example automotive engineering as a material for crash energy absorption to increase the passive safety level.

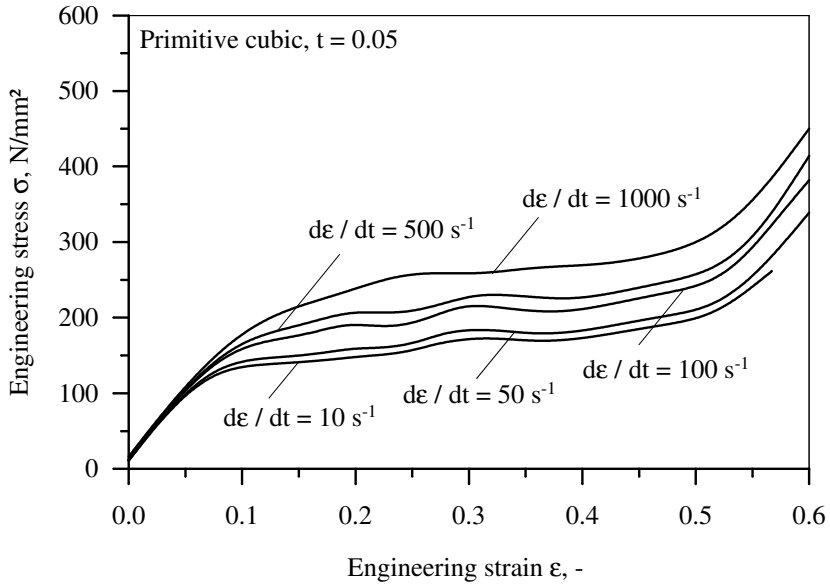

Figure 71: Influence of the strain rate on macroscopic stress-strain response of primitive cubic MHSS.

Next, the body centred cubic and face centred cubic topologies were investigated. In Fig. 72 the stress-strain relations are plotted for the three different shell thicknesses t and the strain rate $\dot{\varepsilon} = 1000\ \mathrm{s}^{-1}$. As observed for the primitive cubic topology, the curves exhibit the typical characteristics of MHSS and stresses as well as the capability

of impact energy absorption increase with the shell thickness t. In the case of the face

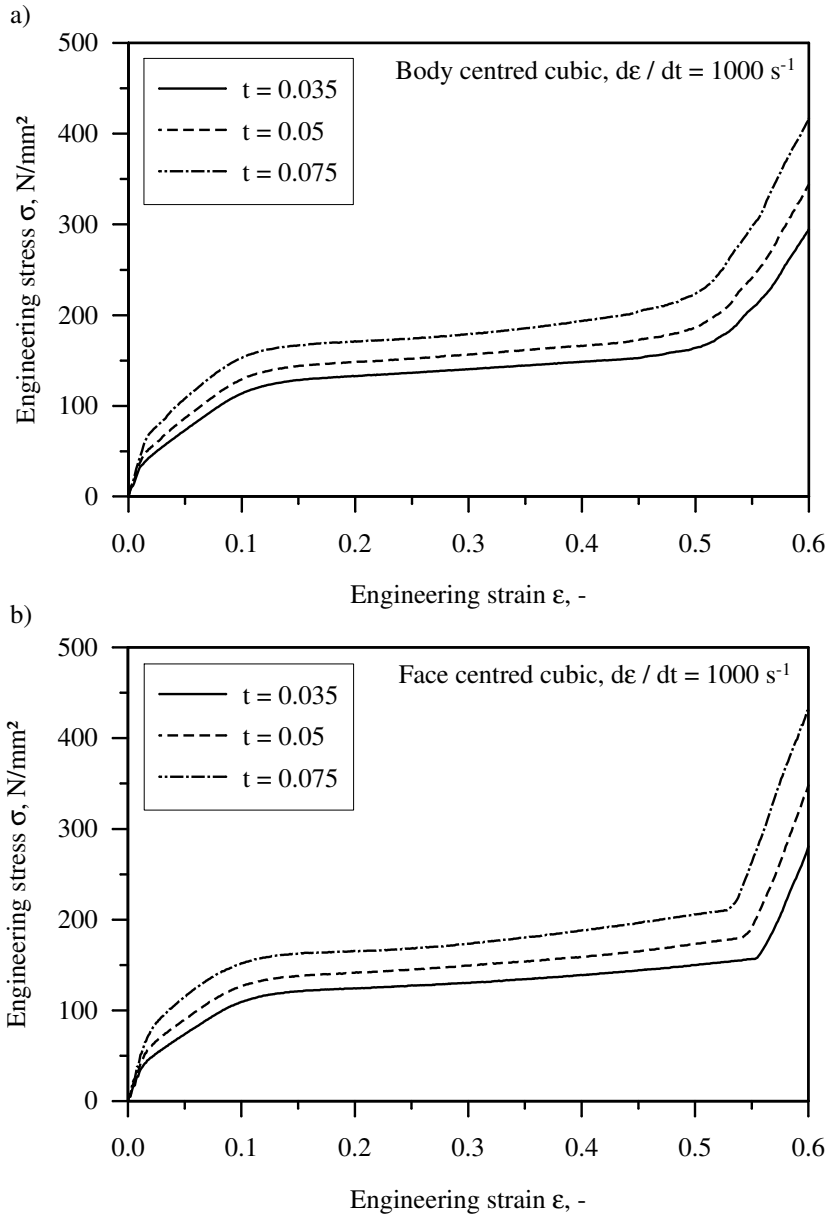

Figure 72: Macroscopic stress-strain relations of MHSS for (a) body centred cubic and(b) face centred cubic topologies.

centred cubic arrangement, the stress level suddenly increases at the beginning of the densification (ε_{D}). This phenomenon is caused by the simultaneous contact of four sphere surfaces per analysed model. This contact response is more pronounced in comparison to the body centred cubic arrangement, where only two sphere surfaces per analysed model are present, and the primitive cubic arrangement, where only one sphere surface per analysed model is present.

The material parameters of primitive cubic, body centred cubic and face centred cubic topologies of composite hollow sphere structure are summarised in Table 11. With increasing the sphere wall thickness the macroscopic Young's modulus, yield stress, plateau stress and plateau modulus increase. From the results it can also be observed that there is a very low influence of the sphere thickness on the densification strain ($\varepsilon = \pm 0.01$) which ensures large plateau regions. In addition to these values, the porosity of the MHSS is given which is defined as the volume of the spherical inclusions per unit cell.

	t [mm]	Porosity [-]	Density [g/cm^3]	E [N/mm^2]	k_c [N/mm^2]	σ_{pl} [N/mm^2]	P [N/mm^2]	ε_{D} [-]
Primitive cubic	0.035	0.335	0.972	1340	19.7	205	194	0.52
	0.05	0.320	1.078	1540	21.1	218	233	0.53
	0.075	0.295	1.249	1830	26.2	237	288	0.53
Body centred cubic	0.035	0.435	0.924	3380	14.3	127	95	0.48
	0.05	0.415	1.063	3770	21.2	142	114	0.49
	0.075	0.383	1.285	5190	32.1	165	151	0.49
Face centred cubic	0.035	0.474	0.906	3430	23.4	118	85	0.53
	0.05	0.452	1.057	3630	26.2	135	99	0.54
	0.075	0.417	1.298	4660	31.1	160	122	0.55

Table 11: Material parameters of MHSS at $\dot{\varepsilon} = 1000$ s^{-1}.

Figure 73 shows a direct comparison between the different topologies ($t = 0.05$, $\dot{\varepsilon} = 1000$ s^{-1}). It is visible that the primitive cubic structure exhibits the highest stresses. This phenomenon can be explained by the low porosity of this topology. In comparison, the porosity in the body centred cubic MHSS and in the face centred cubic MHSS is 1.31 and 1.43 times higher, respectively.

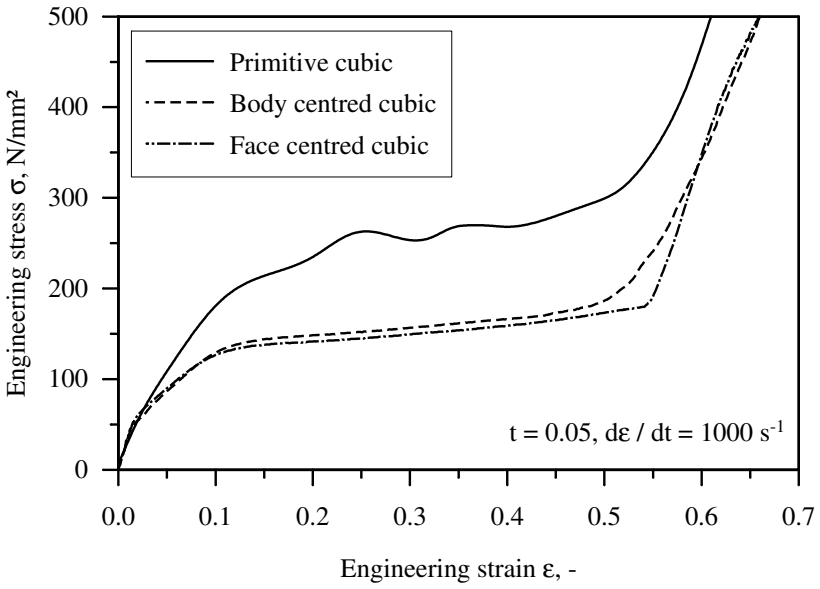

Figure 73: Comparison of the stress-strain relations of different MHSS arrangements.

4.1.4 Thermal Properties

In the following, the results of the finite element analysis for the effective thermal conductivities λ_{eff} of MHSS will be discussed. The influence of the joining technique, morphology, topology and temperature dependent material properties will be analysed.

Influence of the Morphology and Joining Technique Within the scope of the investigation of the influence of the morphology and the joining technique on the effective thermal properties of MHSS, only primitive cubic arrangements of the spheres are analysed. Depending on the considered joining technique, different morphologies and material combinations are generated. Sintering yields a homogeneous and partial structure, whereas adhesive joining results in a heterogeneous (metal/epoxy) structure with varying morphology. Finally, a homogeneous syntactic structure can be achieved by applying casting technologies.

Figure 74 shows the influence of different morphologies for *homogeneous* steel structures. The effective thermal conductivity is plotted versus the sphere wall thickness t. As a result of the higher volume fraction of the matrix, the syntactic MHSS exhibit a significant higher thermal conductivity. In comparison, the partial structures show only low values, especially for a small sphere wall thickness t.

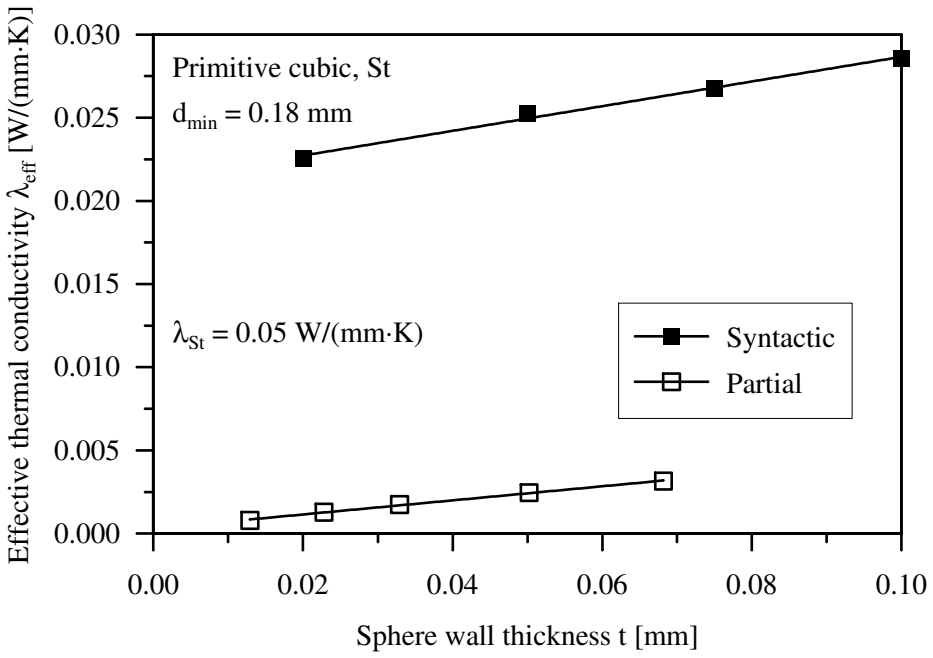

Figure 74: Influence of the morphology of homogeneous MHSS on the effective thermal conductivity.

In Fig. 75, the influence of the morphology on the thermal properties of *heterogeneous*, i.e. adhesively bonded, structures is visualised. Again, due to the higher

volume fraction of the matrix, the thermal conductivity of syntactic MHSS exceeds the values of the partial morphology. However, the deviation is smaller in comparison to the homogeneous structures. This phenomenon can be explained by the low thermal conductivity of the adhesive matrix. Increase of the volume fraction of the matrix therefore only slightly increases the effective conductivity of the structure.

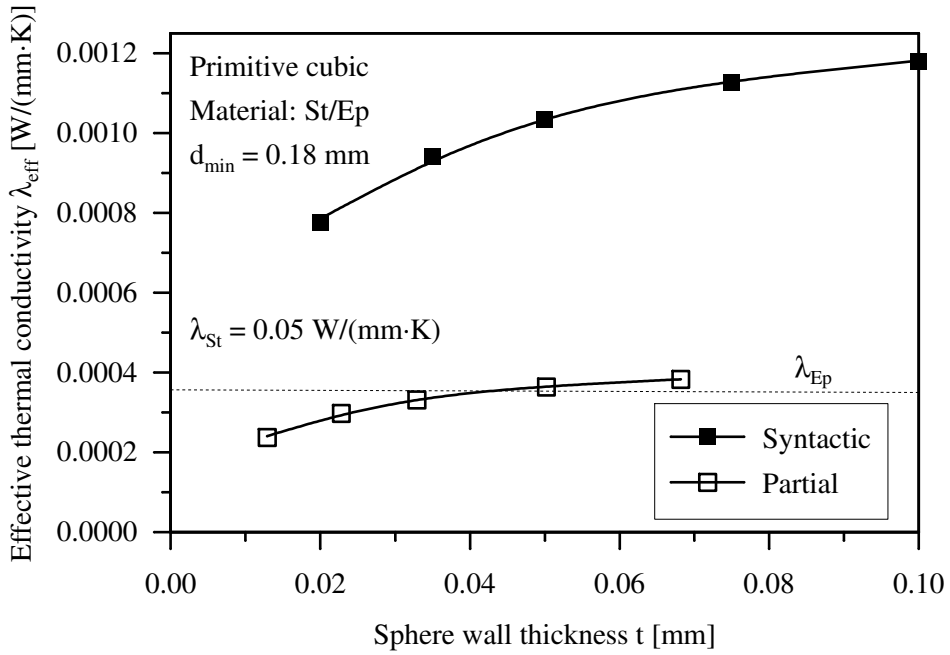

Figure 75: Influence of the morphology of heterogeneous MHSS on the effective thermal conductivity.

Next, two different joining techniques for partial MHSS are compared. Figure 76 shows the results obtained for a sintered and an adhesively bonded structure dependence on the sphere wall thickness t. The effective thermal conductivities λ_{eff} of sintered structures are higher compared to the adhesively bonded MHSS and linearly increase with the thickness t. The low thermal conductivity of adhesively bonded structures lies within the range of the thermal conductivity of the adhesive.

The comparison of syntactic MHSS exhibiting different material combinations (cf. Fig. 77) yields large deviations. The explanation is the high volume fraction of the matrix for syntactic morphology in combination with the strongly different thermal conductivities of the base materials steel and epoxy resin (cf. Tab. 6). Therefore, the cast structure exhibits a much higher thermal conductivity than the adhesively bonded MHSS.

Influence of the Topology Three different topologies, namely primitive cubic (■), body centred cubic (●) and face centred cubic (♦) arrangements of spheres (cf.

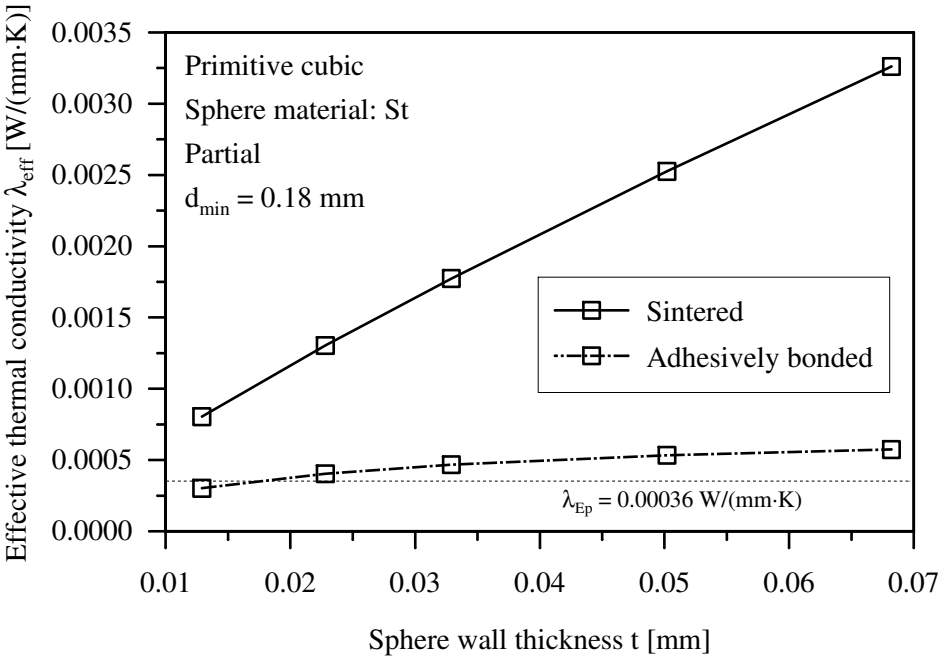

Figure 76: Influence of the joining technique of partial MHSS on the effective thermal conductivity.

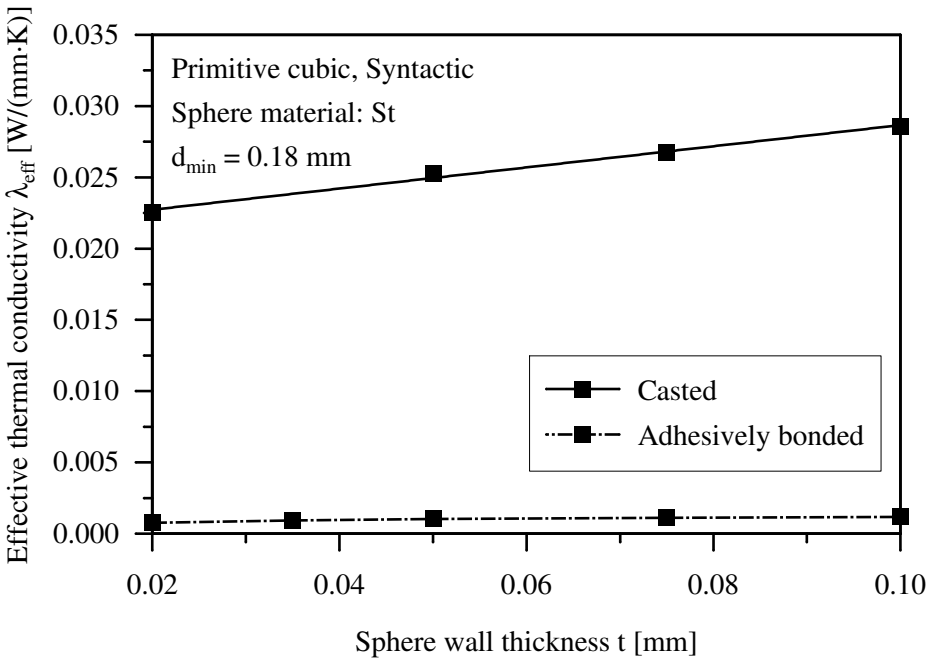

Figure 77: Influence of the joining technique of syntactic MHSS on the effective thermal conductivity.

Fig. 19), are considered. All analyses are performed for a syntactic morphology and two different material combinations (St and St/Ep) are investigated.

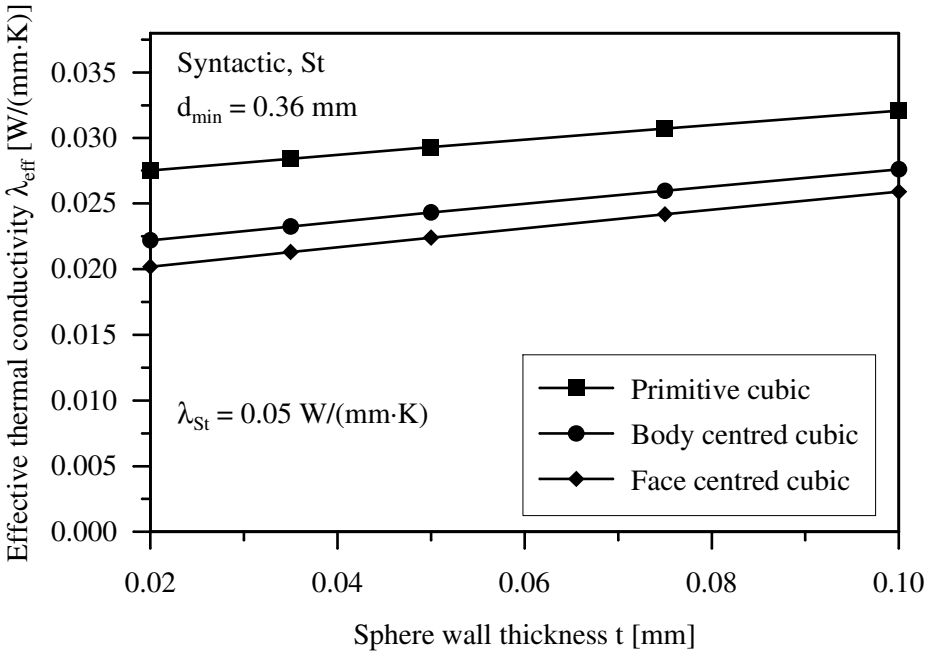

Figure 78: Influence of the topology on the thermal conductivity of homogenous MHSS.

Figure 78 shows the results obtained for *homogeneous* steel structures. For all topologies, a linear characteristic of the effective thermal conductivity λ_{eff} depending on the sphere wall thickness t can be observed. The primitive cubic structures exhibit the maximum thermal conductivity λ_{eff} for a particular shell thickness t. However, by plotting the thermal conductivities versus the free volume $V_{\text{i}}/V_{\text{u}}$, a different picture emerges. The free volume is equal to the volume of the spherical inclusion V_{i} divided by the volume of the unit cell V_{u}.

In Fig. 79 it is clear that all values lie on one straight line. Therefore, the thermal conductivity of homogeneous syntactic MHSS can be described purely by the dependence on the free volume. A linear fit based on the numerical data yields

$$\lambda_{\text{eff}}(V\text{i}/V\text{u}) = [-0.0581 \cdot (V\text{i}/V\text{u}) + 0.0479] \cdot \frac{\text{W}}{\text{mm} \cdot \text{k}}, \tag{71}$$

or with the thermal conductivities λ_{b} of an arbitrary base material

$$\lambda_{\text{eff}}(V\text{i}/V\text{u}) = [-1.16 \cdot (V\text{i}/V\text{u}) + 0.958] \cdot \lambda_{\text{b}}. \tag{72}$$

Figure 80 shows the thermal conductivities of *adhesively bonded* syntactic MHSS. Although the thermal conductivity raises with increasing sphere wall thickness, the

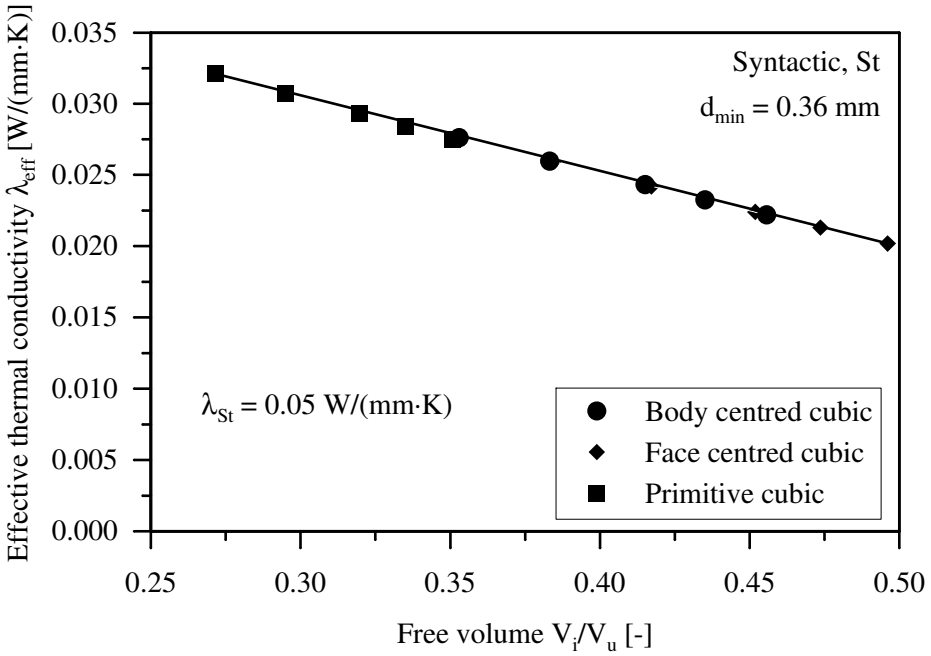

Figure 79: Thermal conductivity of homogeneous MHSS plotted versus the free volume.

gradient of the curve continuously decreases. The explanation is the high thermal resistance of the adhesive matrix between neighboring spheres. Enhancement of the volume fraction of the high thermally conducting sphere wall material therefore only slightly increases the overall thermal conductivity of the structure.

Analogous to the homogeneous structures, λ_{eff} is plotted versus the free volume $V_{\text{i}}/V_{\text{u}}$ in Fig. 81. It can be observed that the face centred cubic arrangement of spheres yields the maximum thermal conductivity for a particular value of the free volume. The explanation is the cubic densest packaging of this topology which causes the highest volume fraction (total volume of the metallic shell divided by the volume of the unit cell) of the metallic sphere wall material. The high thermal conductivity of the metal increases the effective thermal conductivity of the structure. Consequently, the primitive cubic topology which exhibits the lowest volume fraction of the metallic sphere wall material shows the minimum thermal conductivity.

Temperature Dependent Material Properties The determination of the effective thermal conductivity of MHSS incorporating temperature dependent material properties requires the identification of two different cases. First, a low temperature gradient where the temperature is approximately constant within one unit cell, and second, a high temperature gradient, where the changing temperature dependence of the base materials of the structure inside a single unit cell has to be accounted for.

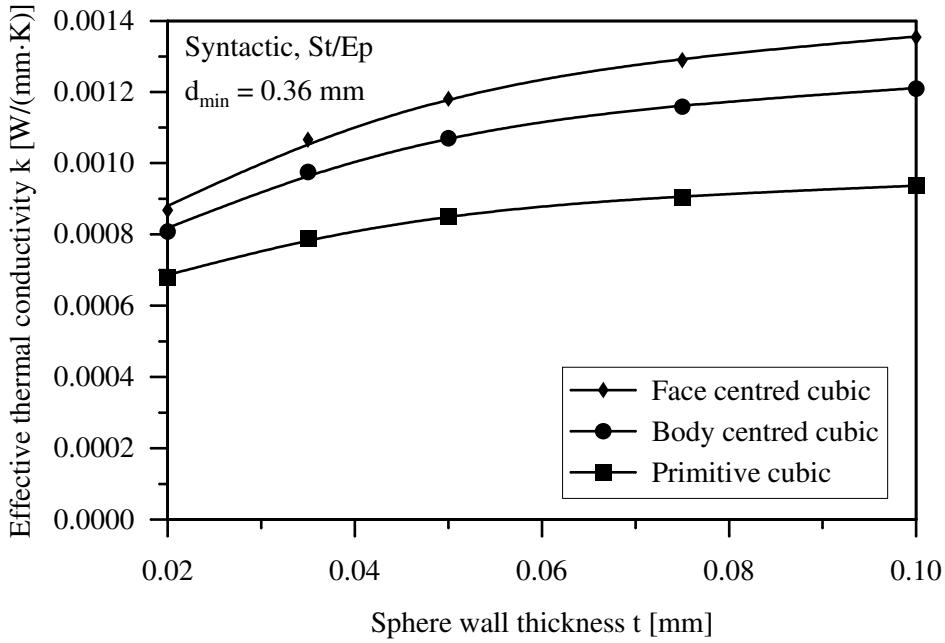

Figure 80: Influence of the topology on the thermal conductivity of heterogeneous MHSS.

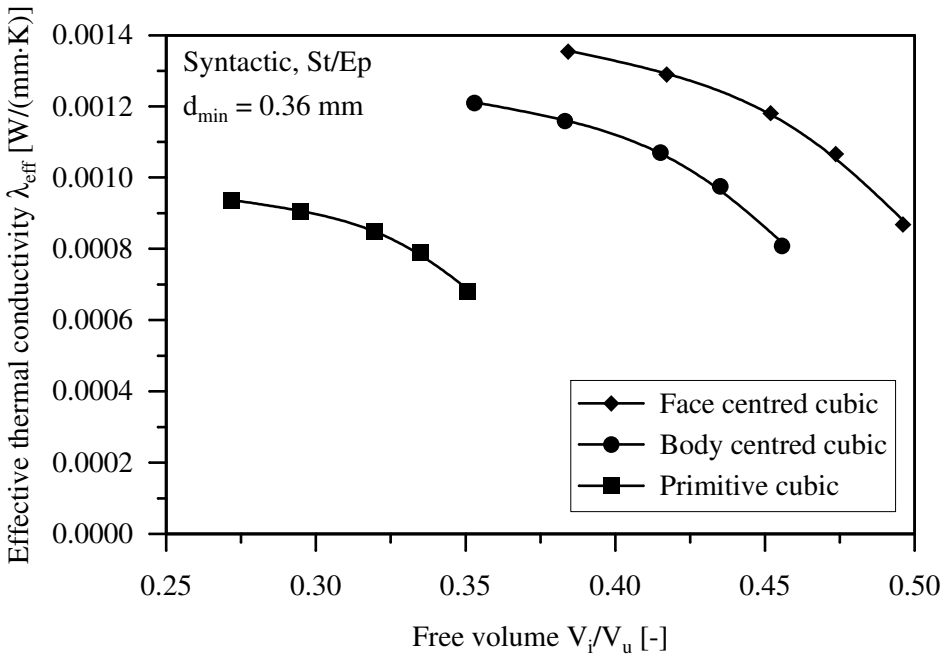

Figure 81: Thermal conductivity of heterogeneous MHSS dependence on the free volume.

Low temperature gradient In the case of a low temperature gradient, the temperature inside one unit cell can be regarded as approximately constant. Ac-

cordingly, the thermal conductivity of the MHSS can be determined only dependent on this temperature. The temperature boundary conditions (cf. Fig. 26) are $T_1 = T_i + 0.01$ K and $T_2 = T_i - 0.01$ K for $T_i = 293, 303, ...433$ K and the results of these calculations are summarised in Figs. 82 and 83.

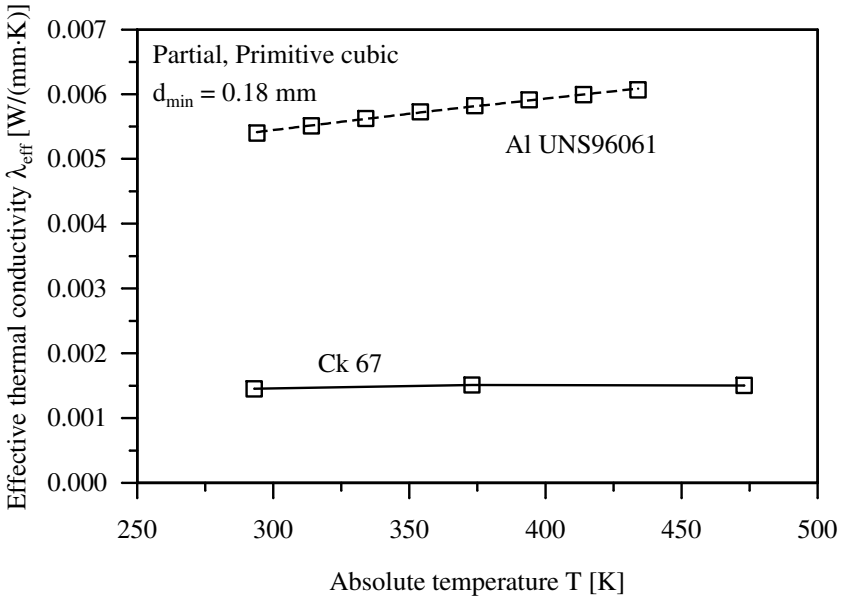

Figure 82: Effective thermal conductivity of sintered MHSS incorporating temperature dependent base material parameters for low temperature gradients.

Figure 83 shows the temperature dependence of the thermal conductivity of adhesively bonded MHSS. In comparison to the results of sintered structures (cf. Fig. 82), the values of adhesively bonded MHSS are lower. The adhesively bonded structures exhibit a maximum in the conductivity at ca 340 K (Al/Hysol), respectively 390 K (Ck67/Hysol). The conductivity of the sintered structures rises linearly with absolute temperature within the given range. The high thermal conductivity of the aluminium alloy (cf. Fig. 29) also increases the thermal conductivity of MHSS. In comparison, the utilisation of CK67 as the sphere wall material decreases the thermal conductivity of the structure.

High temperature gradient In contrast to the simplification in the previous section, high temperature gradients require the consideration of the temperature distribution inside the unit cell. Due to the temperature dependence of the thermal conductivities of the base materials (cf. Fig. 29), the thermal conductivity of the unit cell depends on the absolute values of both temperatures T_1 and T_2 and can therefore not be determined for particular temperatures. In order to confine the complexity of this investigation, the temperature T_1 is fixed at the constant temperature 298 K

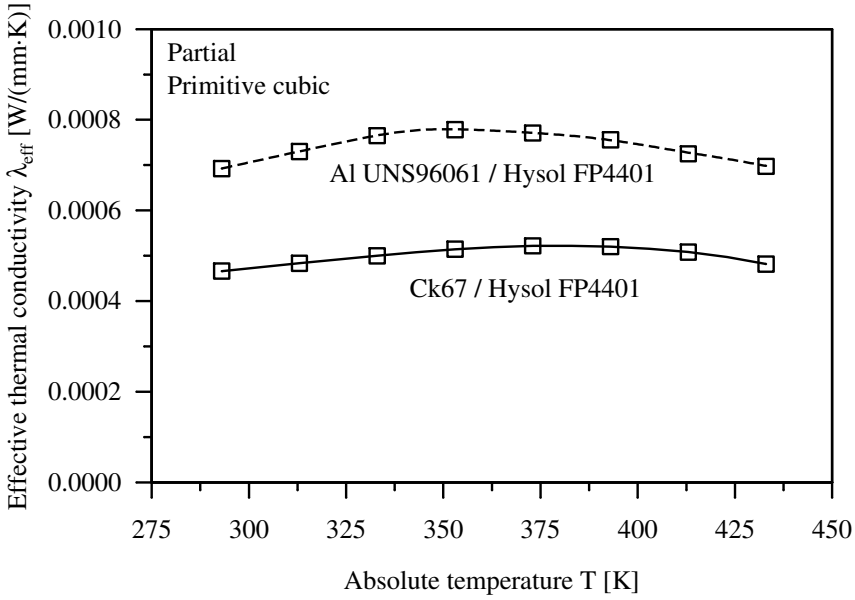

Figure 83: Effective thermal conductivity of adhesively bonded MHSS incorporating temperature dependent base material parameters for low temperature gradients.

(approximately room temperature) and only the temperature T_2 is varied between $323, 348..., 423$ K (glass transition temperature of the considered exopy resin is 433 K [121]). The results are obtained for the unit cell as well as for a homogenised model of the MHSS. The homogenised model is assembled by planar rectangular elements and exhibits the thermal properties obtained in the previous section 'Low Temperature Gradient' for the MHSS.

Figure 84 shows the results of both analyses. In the case of low temperature gradients (e.g. $T_2 = 323$ K $\rightarrow \Delta T/\Delta y = 25$ K/2.12 mm), the results obtained for both models almost coincide. However, also for the maximum temperature difference of 125 K the deviation between the results for the unit cell and the homogenised model reach only 0.93 %.

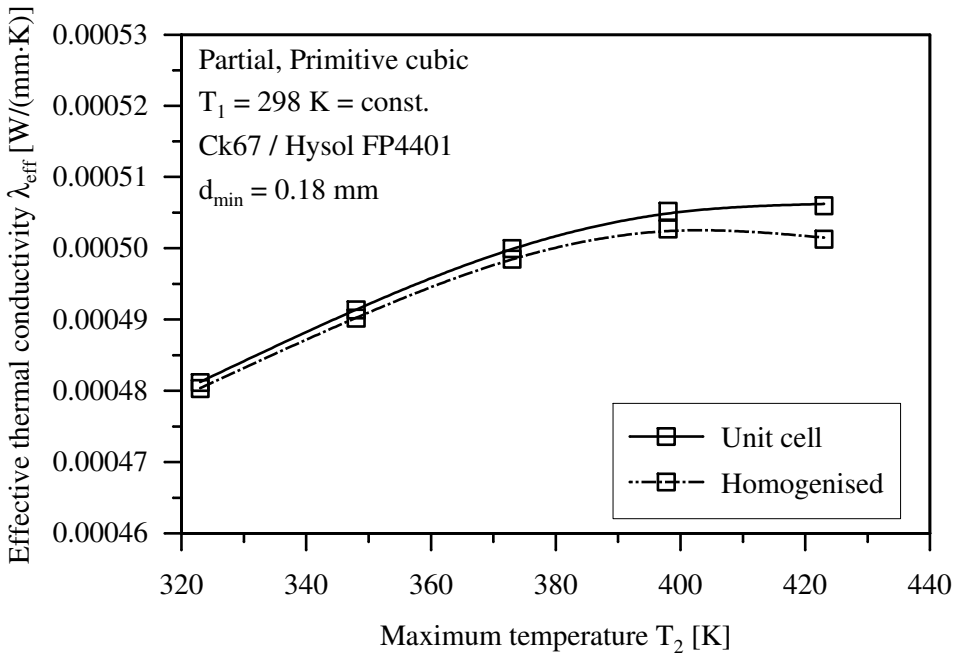

Figure 84: Effective thermal conductivity incorporating temperature dependent base material parameters for high temperature gradients.

Experimental findings In addition to the numerical analysis, the transient plane source (TPS) method is applied to measure the effective thermal conductivity of MHSS. Two samples with partial ($\overline{\rho} = 0.59$ g/cm^3) and syntactic morphology ($\overline{\rho} = 1.26$ g/cm^3) are considered.

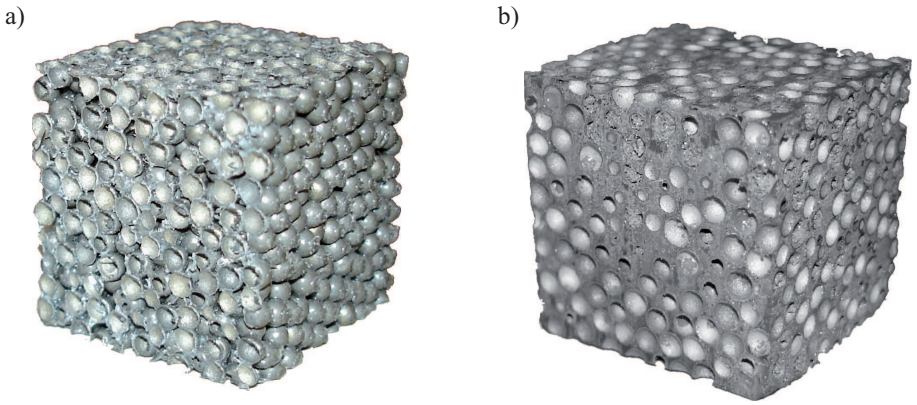

Figure 85: MHSS samples for thermal measurements: a) Partial MHSS, b) Syntactic MHSS.

In order to compare the findings of the experimental analysis with the numerical results, the geometrical dimensions for the corresponding finite element models need to be determined. The averaged minimum distance $d_{\min}$ between two neighboring spheres varies with the morphology and is found to be 0.18 mm for partial and 0.36 mm for syntactic MHSS. Furthermore, the outer radius R of the hollow spheres is 1.5 mm and the shell thickness t is 0.1 mm. Due to the small minimum distance $d_{\min}$ of the partial morphology, only a primitive cubic arrangement of the spheres is considered. The meshing of the body centred or face centred cubic topology for this value of $d_{\min}$ yields strongly distorted elements which reduce the accuracy of the results. The thermal conductivities λ of the base materials are defined according to Section 3.1.4 (Thermal material properties) and the results of the TPS method and the numerical analysis are given in Table 12. It is clear that the results of both approaches are in good agreement.

Morphology	Experimental results	Numerical results
Partial	0.57 ± 0.05 W/(m·K)	0.51 W /(m·K)
Syntactic	1.01 ± 0.05 W/(m·K)	1.09 W /(m·K)

Table 12: Experimental findings of the thermal conductivity of MHSS.

4.2 Sandwich Structures

Within the scope of this work the applicability of novel MHSS as core materials in sandwich structures is investigated. Therefore, the mechanical and thermal properties of sandwich compounds with different core materials are numerically and experimentally determined. The results of these analyses are compared in order to evaluate the performance of the different core materials.

4.2.1 Mechanical Properties: Experimental Findings

In the following, the results of three-point bending tests on sandwich structures with different core materials are shown. In total, five different core materials, each in groups of three specimens, are tested. These cores are enclosed by two Al5005 aluminium face sheets with a constant thickness $t = 1$ mm. The geometric dimensions and the material compositions of these specimens are given in Table 13.

ID	Core material	Core density [g/cm^3]	Span d_s [mm]	Width w [mm]	Height c [mm]	Height h [mm]	Length l [mm]
#1		0.38	250	17.7	29.4	31.4	280
#2	Alporas®	0.32	250	17.7	29.6	31.6	280
#3		0.32	250	17.7	29.5	31.5	280
#4		0.21	250	30.5	30.6	32.6	280
#5	M-Pore®	0.22	250	30.8	30.7	32.7	280
#6		0.20	250	30.6	30.8	32.8	280
#7		0.10	250	31.5	20	22	350
#8	Honeycomb	0.10	250	31	20	22	350
#9		0.09	250	30.5	20	22	350
#10		0.35	250	30.3	29.5	31.5	280
#11	Part. MHSS	0.34	250	30.3	30.1	32.1	280
#12		0.34	250	30.3	30.3	32.3	280
#13		1.26	250	29.9	30	32	270
#14	Synt. MHSS	1.25	250	30	30	32	270
#15		1.25	250	30	29.8	31.8	270

Table 13: Material composition and geometric dimensions of the sandwich specimens.

Two material parameters, namely the flexural stiffness E_{Str} and the maximum load before failure $F_{\max}$, are determined for each specimen. Furthermore, the failure mode is compared for the different core materials. In order to minimise the influence of different geometries on these results, all specimens are of similar geometry. The width of all specimens is $w \approx 30$ mm, only in the case of the Alporas® core material the dimensions of the raw material only allowed for a maximum width of 17.7 mm. Preliminary numerical analysis and evaluation of the analytical Equations (57) ff.

show that within the considered range, the width w does not influence the flexural stiffness E_{Str} of a sandwich panel. However, the maximum load $F_{\max}$ must be linearly corrected in order to compare this value to the other geometries ($F_{\max} = 30$ mm /17.7 mm $\cdot F^{\#}_{\max}$). A similar problem emerged with the honeycomb cores. The dimensions of the raw material in conjunction with its highly anisotropic properties only allowed for the manufacturing of specimens with a core height $c = 20$ mm. According to Equation (67) the change of the height from 30 mm to 20 mm significantly affects the flexural stiffness. A rough estimation of this dependency can be achieved by neglecting the contribution of the core and the face sheets around their local bending axis. If only STEINER'S theorem is considered Equation (67) yields

$$E_{\mathrm{Str}} \approx \frac{6 \cdot E_f \cdot t \cdot s^2}{h^3} \approx \frac{6 \cdot E_f \cdot t \cdot h^2}{h^3} \tag{73}$$

and accordantly $E_{\mathrm{Str}} \sim 1/h$. However, the evaluation of the experimental data according to Equations (64) and (57) compensates for the influence of different heights h. Unfortunately, a simple linear correction of the maximum force $F_{\max}$ like in the case of different widths w is not possible. The failure mode of the structure depends on the ratio of height h and span d_s (e.g. [69]). Accordingly, a different height of the honeycomb sandwich might change the failure mode and consequently the maximum force.

In addition, the span d_s of the experimental setup has a significant impact on the three-point bending test. The span determines the ratio between bending and shear loading and also influences the failure mode of the specimens. Accordingly, the span d_s of the experimental setup is constant 250 mm. Differences in the overall length l of the samples have no impact on the experimental results, since preliminary numerical analyses have shown, that changes in the overhang $d_o = (l - d_s)/2$ have no influence on the three-point bending tests. Failure due to core shear and respective dependencies of the shear deformation on the overhang d_o as described e.g. in [69, 122] could not be observed within these analyses.

The result of the three-point bending tests are force-displacement curves. Figure 86 shows a characteristic force-displacement curve of a sandwich compound with a metallic cellular core. Three different areas can be distinguished: Within this elastic range, the curves exhibit a linear characteristic and the ratio F/u is constant. The determination of the flexural stiffness E_{Str} is based on the force-displacement values of the elastic range. In the plastic range, the gradient of the curve decreases. Plastification might occur in the core material and/or in the face sheets. In addition, the failure of the sandwich can be initiated, for example by the generation of a crack inside the core material. Finally, after reaching the critical load $F_{\max}$ the structure fails. Depending on the failure mode, the force decreases slowly and continuously (e.g. core indentation) or spontaneously drops to a low value (e.g. delamination).

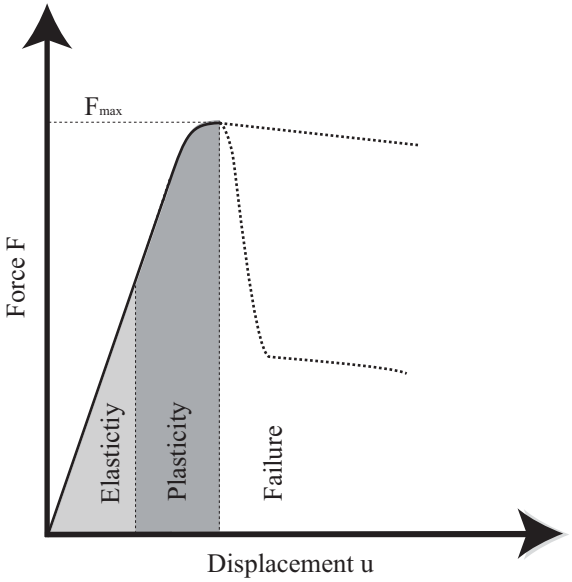

Figure 86: Schematic force-displacement relation of a three-point bending test.

Sandwich compounds can also act as energy absorbing structures, e.g. crash elements. The ability to absorb energy can be quantified by calculating the absorbed energy W_{tot} which is equal to the area under the force-displacement curve. Within this work, only the energy before the failure of the structure is considered. The elastic energy W_{el} theoretically can be released after unloading of the sandwich structure and should be subtracted in order to obtain the plastic energy W_{pl} (dark grey area in Fig. 86). However, the elastic energy is typically much smaller in comparison to the plastic energy and therefore the introduced error is very small.

Flexural stiffness In the first step, the flexural stiffness E_{Str} of the sandwich structures listed in Table 13 is analytically and experimentally determined. The analytical solution is obtained by applying Equation (67). For the evaluation of the experimental data, two different methods are used. First, Equation (64) is applied where the shear modulus of the sandwich structure is estimated based on the structural flexural stiffness E_{Str}. However, this method is only accurate for isotropic materials and in the case of anisotropic sandwich compounds, where the flexural stiffness for bending about the z-axis is much higher than the shear modulus inside the yz-plane (cf. e.g. Fig. 27), only rough approximations of E_{Str} can be obtained. On the other hand, the obtained result is perfectly suited for the evaluation of the inherent stability of the sandwich structure, if no distinction between flexural and shear deflection is required. It only must be taken into account that the obtained material parameter is not equal to Young's modulus in the equation of the bending line (53).

Additionally, an alternative evaluation method is used where the shear deflection

is calculated in dependence on the shear modulus G_c of the core material. Thereby, the shear modulus G_c is estimated based on Young's modulus E_c of the core material according to $G_c = E_c/3$. The measured deflection is then corrected by subtracting the shear deflection and Eq. (57) (corrected) can be employed for the determination of the structural flexural stiffness E_{Str}.

ID	Core material	Flexural stiffness E_{Str}			$\overline{\delta}$
		Analytic (67) [N/mm^2]	Exp. (64) [N/mm^2]	of Exp. (57) (cor.) [N/mm^2]	Exp. (64) [%]
#1	Alporas® $E_c = 1100$ N/mm^2	13400	6210	12100	8.1
#2			5280	9300	
#3			5760	10500	
#4	M-Pore® $E_c = 85$ N/mm^2	12400	2250	-	33.5
#5			3350	-	
#6			4300	-	
#7	Honeycomb	12400	10000	-	4.7
#8			10900	-	
#9			10000	-	
#10	Part. MHSS $E_c = 750$ N/mm^2	12800	4520	11200	13.5
#11			4270	9800	
#12			3520	8500	
#13	Synt. MHSS $E_c = 2320$ N/mm^2	14200	9200	14000	4.5
#14			9500	15200	
#15			10000	16100	

Table 14: Flexural stiffness E_{Str} of sandwich structures with different core materials.

The results of this analysis are shown in Table 14. The analytical solution (67) only weakly depends on Young's modulus E_c of the core material. The maximum value 14200 N/mm^2 is observed for the syntactic MHSS, the minimum value for M-Pore® still reaches 12400 N/mm^2. Adequate agreement can be found by comparing the analytical solutions to the experimental results according to Equation (57) (corrected). Accordingly, the analytic relation is a suitable tool for the estimation of the flexural stiffness of sandwich structures. The experimental evaluation method according to Eq. (57) (corrected) cannot be applied for M-Pore® and honeycomb cores. In the case of the M-Pore® core material, a correction of the measured deflection is not possible, since the calculated shear deflection exceeds the measured value. Possible explanations are exaggerated anisotropic elastic properties or strong scattering of the shear modulus G_c of this core material. The strong deviation between the calculated and measured Young's modulus in [100] indicates the problematic determination of this material parameter for M-Pore® structures. In the case of the honeycomb structure, the strong anisotropy of the core material does not allow for a simple correction of the deflection.

For the analytic estimation (67) of the flexural stiffness E_{Str}, Young's modulus of the honeycomb core in longitudinal beam direction is assumed to be zero. Due to these restrictions, a direct comparison between the different core materials can only be done after applying Equation (64). The maximum flexural stiffness E_{Str} is obtained for honeycomb cores, closely followed by syntactic MHSS. The M-Pore® sandwich structures show minimum values which reach only about 25 % of the maximum results. In order to quantify the scattering of the obtained results, the normalised standard deviation $\overline{\delta}(E_{\mathrm{Str}})$ (cf. Appendix E) is calculated for each group of different core materials. Here the syntactic MHSS show a minimum value of 4.4 % which indicates low scattering. As expected, also the honeycomb structures possess constant material properties ($\overline{\delta} = 4.7\%$). The highest normalised standard deviation $\overline{\delta} = 33.5\%$ is observed for the M-Pore® structures. It must be mentioned here that the investigated number of three samples per core material is insufficient for the derivation of statistical data and the above values should therefore be interpreted with caution.

Figure 87 shows the flexural stiffness according to Eq. (64) plotted versus the density of the core material. High specific values are located in the top left area of the graph. Accordingly, sandwich structures containing honeycomb cores exhibit a significantly higher specific flexural stiffness than the other compounds. Alporas® cores yield the highest specific values among the irregular cellular core materials. The specific stiffness of the adhesively bonded MHSS (partial and syntactic) is reduced by the low Young's modulus of the adhesive. Improved performance can be expected from e.g. sintered MHSS.

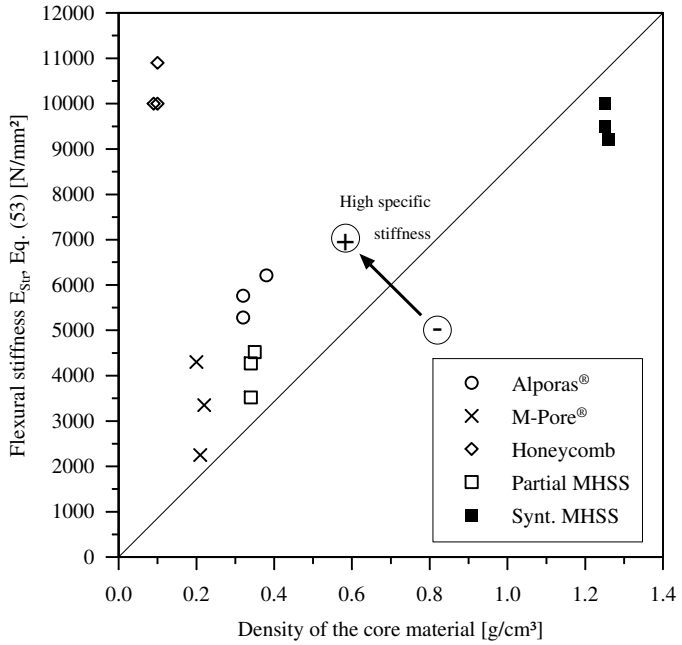

Figure 87: Flexural stiffness E_{Str} of sandwich structures according to Eq. (64).

Load-Carrying Capacity Besides the flexural stiffness, the load-carrying capacity of sandwich compounds is of great interest. This attribute can be quantified with the maximum load $F_{\max}$ that the structure can bear. The results are shown in Table 15.

ID	Core material	Maximum load [N]	Average value [N]	Norm. stand. dev. $\overline{\delta}$ [%]
#1	Alporas®	2090 (cor.)	1700	20.2
#2		1560 (cor.)		
#3		1440 (cor.)		
#4	M-Pore®	630	700	23.1
#5		880		
#6		580		
#7	Honeycomb	1020	940	9.1
#8		940		
#9		850		
#10	Partial MHSS	2280	2100	17.7
#11		2340		
#12		1670		
#13	Synt. MHSS	3070	3300	6.1
#14		3470		
#15		3300		

Table 15: Maximum load $F_{\max}$ of sandwich structures with different core materials.

Minimum absolute values are obtained for the M-Pore® sandwich compounds. Also the honeycomb structures exhibit low results for $F_{\max}$. However, it must be taken into consideration that due to the smaller core height c of the honeycomb specimens, the values cannot be directly compared to the other structures. The decrease of the core height c distinctly decreases the flexural rigidity and therefore also the maximum force. Accordingly, higher values of $F_{\max}$ are expected for honeycomb sandwich structures with default geometric dimensions. The maximum force $F_{\max}$ of the Alporas® sandwich compounds is corrected by multiplication by the factor 30 mm / 17.7 mm in order to account for the smaller width w of these specimens. In comparison to the M-Pore® aluminium foam, a high maximum load with an average value of 1700 N is obtained. This value is only exceeded by the partial and syntactic MHSS core material. The syntactic MHSS exhibit the highest absolute load carrying capacity (3300 N) among the investigated core materials.

In Fig. 88 the maximum force is plotted versus the average density. The highest specific values can be observed for honeycomb and partial MHSS cores. It again should be highlighted that for the default geometry, the specific values of the honeycomb sandwiches are likely to further increase.

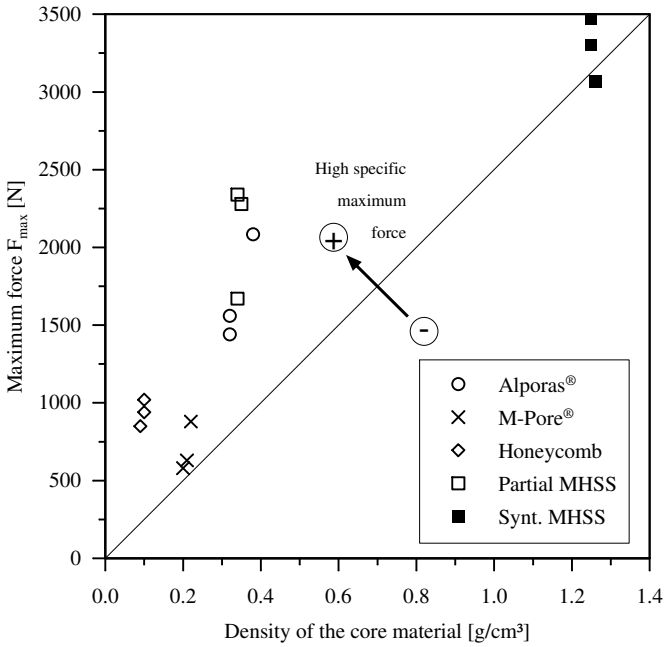

Figure 88: Maximum force $F_{\max}$ of sandwich structures.

Failure Modes The failure of sandwich structures can be categorised according to different failure modes. In the literature, the most important failure modes face yield, face wrinkling, core indentation (cf. Fig. 89) and core shear are well documented [21, 69, 66, 123]. In the following, the failure modes of the different core materials and the corresponding force-deflection curves will be shown. It is important to note that the failure mode is also dependent on the geometric dimensions of the sandwich structure and therefore the results given are only valid for the geometries listed in Table 13.

Alporas® Figure 90 shows the force-deflection curve of the Alporas®-core sandwich compounds. The curves fit the schematic drawing displayed in Fig. 86. In the elastic range the curves rise linearly. At the displacement $u \approx 0.5$ mm the core material begins to deform plastically and the gradient of the curve decreases. To the author's knowledge, no simple measurement technique exists to exactly determine the onset of the plastic yield inside the core material. In order to determine the onset of the plastic yield inside the face sheets, a strain gauge is attached to one of the specimens at the lower face sheet opposite the pressure stamp where the maximum stresses occur. The longitudinal and transverse strains are measured and plotted in Fig. 91. In the case of elastic material behavior of the aluminium face sheets, the ratio of longitudinal and transverse strain is constant and the graph lies on the dashed line. At the deflection $u \approx 2.9$ mm, the beginning of plastic flow in the face sheet is indicated by the change of this ratio. The structures fail due to indentation of the pressure stamp into the core material (cf. Fig. 89 a)). This failure mechanism cannot be related to

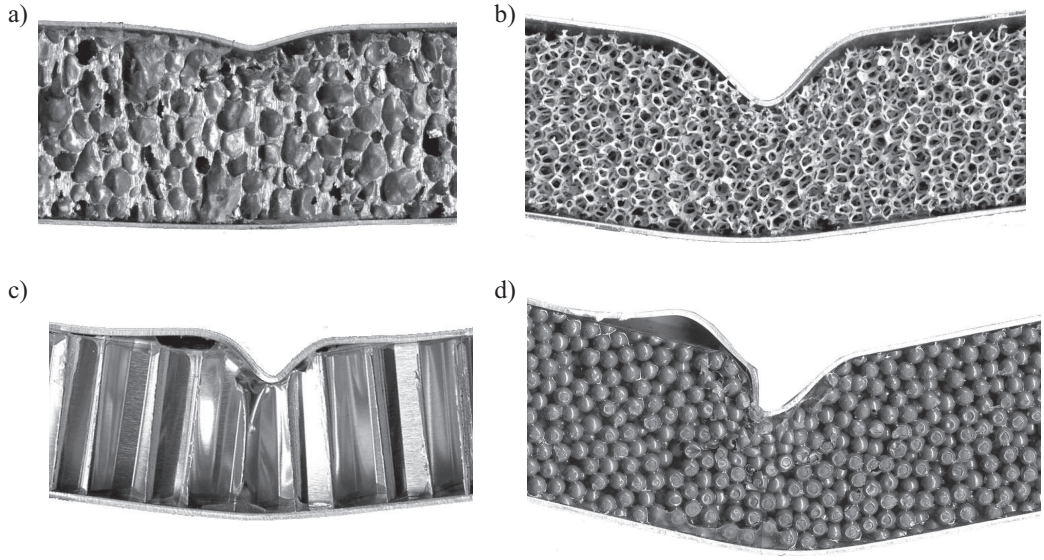

Figure 89: Core Indentation: a) Alporas®, b) Metfoam®, c) Honeycomb structure , d) Partial MHSS.

a specific deflection or load, but continuously decreases the bearable load F of the sandwich. Consequently, this failure mode is potentially safe, since the load-bearing capacity decreases slowly and a catastrophic collapse of the structure is unlikely.

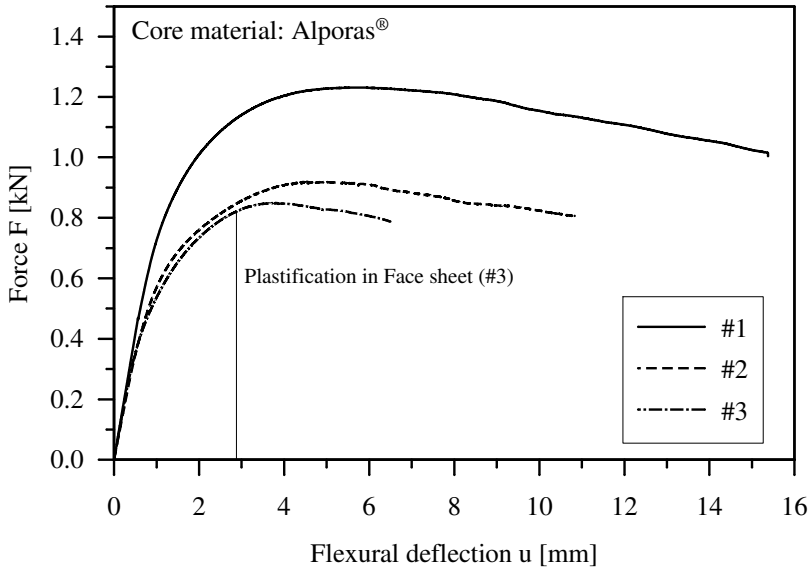

Figure 90: Flexural force-deflection curves of sandwich structures with Alporas® cores (ID number refers to Table 13).

M-Pore® Figure 89 b) shows that sandwich structures with M-Pore® cores also fail due to core indentation. The force-deflection curves are shown in Fig. 92. In

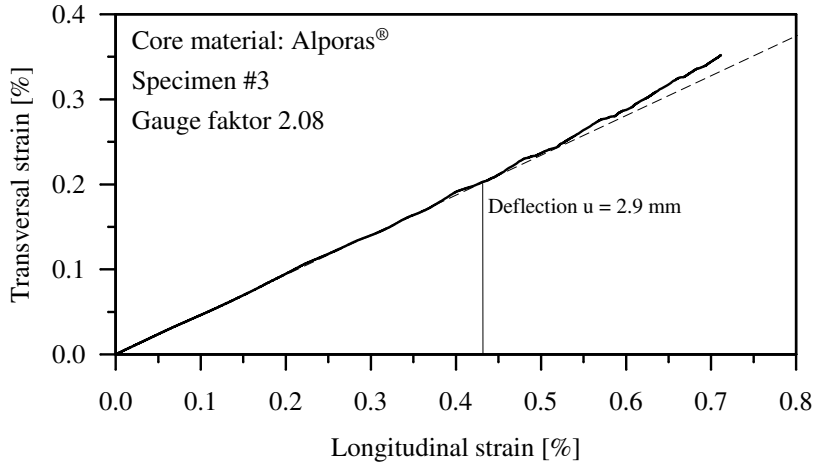

Figure 91: Local strains in the centre of the lower face sheet of a sandwich structure with an Alporas® core.

comparison to the Alporas® sandwich structures, the observed forces F are smaller. Furthermore, the force remains approximately constant after reaching the maximum load $F_{\max}$. This behaviour is typical for the uniaxial compression of cellular metals and in conjunction with the low forces indicates that the core material is too weak to transfer the shear loads between the face sheets. Instead, the M-Pore® cores merely collapse under the compressive loading applied by the pressure stamp. In [66] this failure mode is also named 'core crushing'. The onset of the plastic flow inside the aluminium face sheets is again determined by a strain gauge and is preceded by plastic deformation inside the core material.

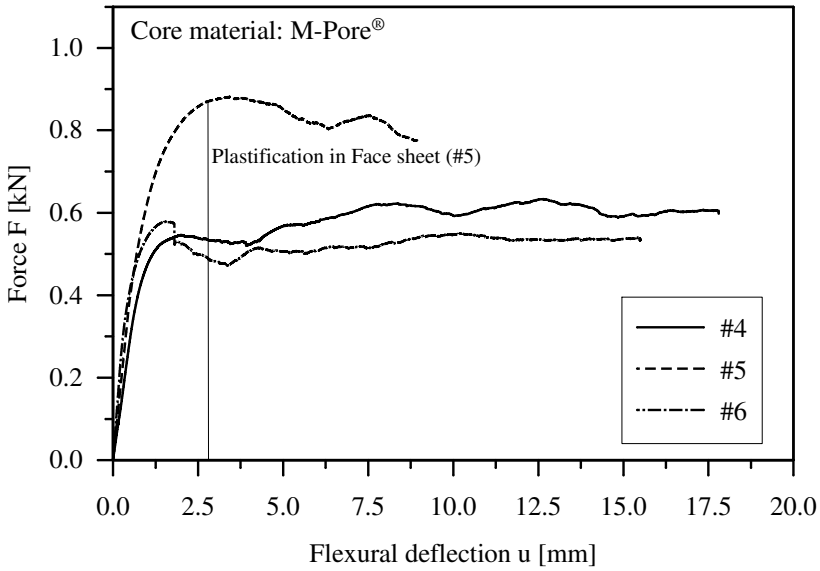

Figure 92: Flexural force-deflection curves of sandwich structures with M-Pore® cores.

Honeycomb Figure 93 shows the force-displacement data of the honeycomb-core sandwich structures. For this type of sandwich compound, two different initial failure modes are observed. Specimens #7 and #8 fail due to local delamination of the face sheets from the core in the area under the pressure stamp. This delamination coincides with a sudden decrease of the force F and is followed by the indentation of the pressure stamp into the core material (cf. Fig. 89 c)). Specimen #9 shows a slightly different failure behavior: the indentation of the pressure stamp precedes the local delamination of the face sheets. Accordingly, after the maximum force $F_{\max}$ is reached the force F only slowly decreases. The spontaneous decrease of the bearable force due to delamination (#7, #8) is potentially critical for safety relevant applications, since a sudden collapse of the sandwich panel might be triggered.

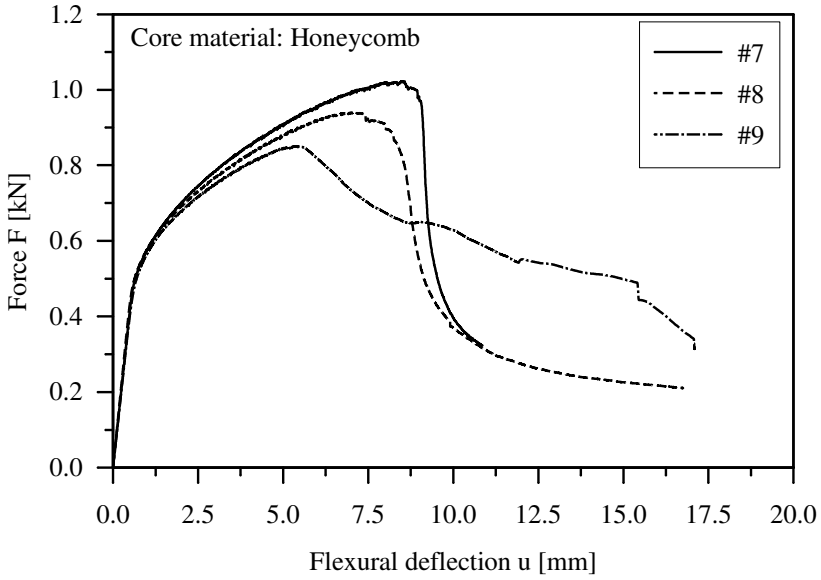

Figure 93: Flexural force-deflection curves of sandwich structures with honeycomb cores.

Partial MHSS The force-deflection curves of sandwich compounds with partial MHSS cores are shown in Fig. 94. In comparison to the earlier discussed core materials, distinctly higher forces F can be observed. For all specimens, the initial failure mode is face yield. However, the plastification of the face sheet has only a low impact on the macroscopic force-deflection curve of the sandwich compounds. The catastrophic failure of the structure causing a spontaneous decrease of the load-carrying ability is effected by subsequent failure mechanisms. Specimen #10 fails due to core fracture (cf. Fig. 95 a)), immediately followed by the delamination of the lower face sheet. This failure mode is characterised by a spontaneous decrease of the bearable force to zero. A similar behaviour is observed in the case of specimen #11 where core

fracture and delamination are preceded by a fractional indentation of the pressure stamp in the partial MHSS core. The force-deflection curve of Specimen #12 shows a different behavior where the force remains approximately constant after failure. No core fracture is observed and the sample fails due to core indentation and subsequent local delamination of the upper face sheet (cf. Fig. 89 d)). It can be concluded that this material combination in conjunction with the geometric dimensions of the specimens (cf. Table 13) lies in the transition zone of failure due to core indentation and failure due to face yield / core fracture.

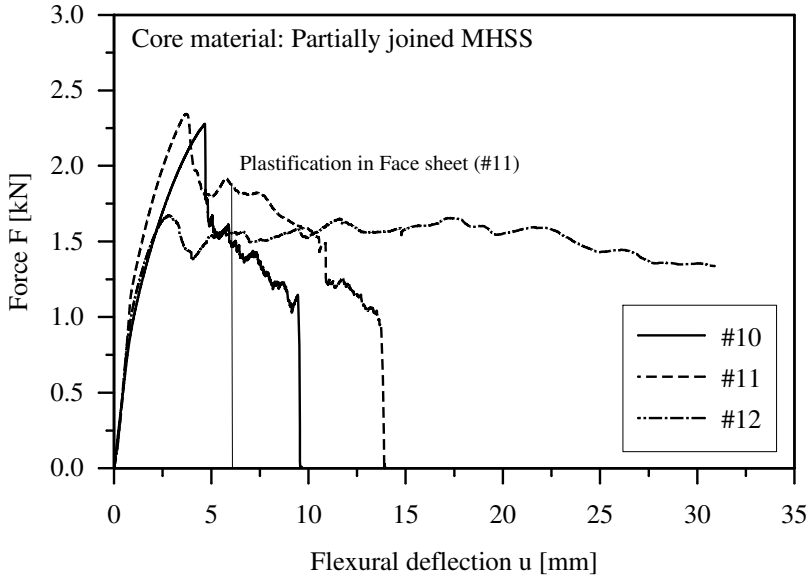

Figure 94: Flexural force-deflection curves of sandwich structures with partial MHSS cores.

The core fracture (#10, #11) is localised in the centre of the sandwich core, close to the lower face sheet where the maximum tensile stresses occur. Thereby, the crack propagates solely through the adhesive joints that connect neighboring hollow spheres. In contrast to core fracture, core indentation exhibits the advantage that the load-carrying ability of the sandwich compound does not suddenly drop to zero and the structure is able to absorb energy even after the maximum force is reached. In order to shift the failure mode from core fracture to core indentation, e.g. a stronger adhesive bonding of the spheres is required.

Syntactic MHSS Figure 96 shows the results of the three-point bending test of sandwich compounds with syntactic MHSS cores. The highest forces among the investigated sandwich structures can be found. Within the elastic range, the force-deflection curve rises linearly. At the deflection $u \approx 0.4$ mm, plastic deformation starts inside the syntactic MHSS core. The measurement of the longitudinal and transverse

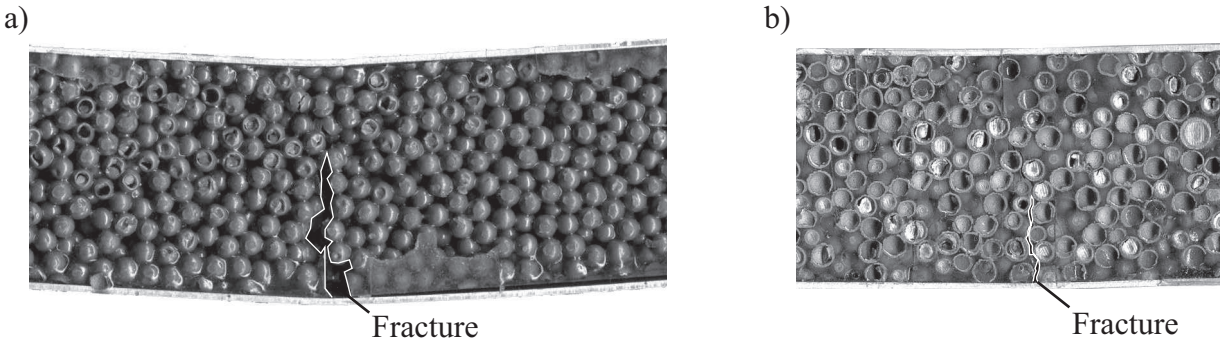

Figure 95: Core Fracture: a) Partial MHSS, b) Syntactic MHSS.

strains at the centre of the lower face sheet (#15) show that at $u \approx 0.6$ mm also the aluminium face sheet starts to flow plastically (initial failure mode: face yield). After reaching the maximum force $F_{\max}$, core fracture occurs (cf. Fig. 95 b)) and the load-carrying capacity is reduced by approximately 60%. Despite further growth of the crack, the force transitionally stabilises around this reduced value if the deflection is further increased.

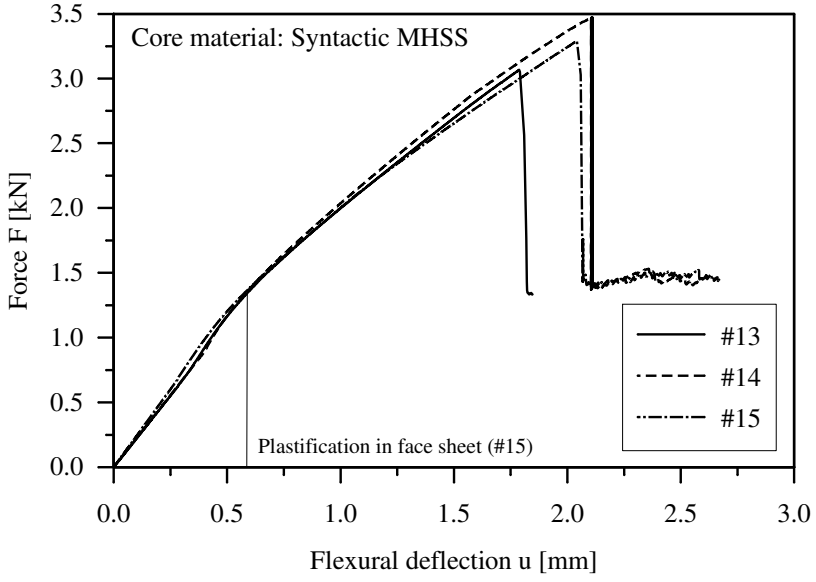

Figure 96: Flexural force-deflection curves of sandwich structures with syntactic MHSS cores.

Failure Maps The failure mode of sandwich panels under three-point bending loading can be predicted in dependence on their material composition and geometric dimensions. In the literature [21, 66, 69] formulae for critical loads F_{cr} where failure is initiated are provided. Four different failure modes are identified. The critical

failure loads for face yield are compared in Table 16. The estimation provided by Mohan and colleagues [69] refers to the fracture of brittle face sheet materials. Since ductile aluminium face sheets are used in the experimental three-point bending tests, this equation cannot be applied. Ashby et al. [21] determine the critical failure load F_{crit} by equating the maximum bending moment within the sandwich structure to the plastic collapse moment of the section. The second term on the right-hand side of Ashby and colleagues equation describes the contribution of the core material to the plastic collapse moment. However, a cellular metallic core under tensile loading typically exhibits a low-ductility and will fracture almost as soon as it yields causing catastrophic failure (core fracture). Accordingly, it is safer to neglect the contribution of the core material and Ashby's formula becomes identical with Steeve and colleagues [66] estimation of the failure load. It is mentioned earlier that face yield alone does not cause catastrophic failure of the sandwich compound. However, face yield precedes core fracture as observed for the MHSS cores. Therefore, the critical failure loads in Table 16 can be used to predict the occurrence of core fracture.

Ashby et al. [21]	Mohan et al. [69]	Steeves et al. [66]
$\frac{4 \cdot w \cdot t \cdot (c+t)}{d_s} k^{\text{f}} + \frac{w \cdot c^2}{d_s} k^{\text{c}}$	$\frac{2}{3} \cdot \frac{w \cdot t^3 + 3 \cdot w \cdot t \cdot (c+t)^2}{d_s \cdot (2 \cdot t + c)} k^{\text{f}}$	$\frac{4 \cdot w \cdot t \cdot (c+t)}{d_s} k^{\text{f}}$

Table 16: Critical failure loads F_{cr} for face yield / core fracture.

The second failure mode, face wrinkling, is only considered by the research group around Steeves et al. [66] and the corresponding critical failure load can by estimated by the relation

$$F_{\text{cr}} = \frac{2 \cdot w \cdot t \cdot (c+t)}{d_s} (E_f E_c G_c)^{1/3}.$$

Table 17 shows that Mohan and Steeves use identical formulae for the estimation of the failure load F_{cr} preceding core indentation. These relations are preferred to the rough estimation by Ashby et al. which does not incorporate the stiffness of the face sheets and detailed geometric dimensions.

Ashby et al. [21]	Mohan et al. [69]	Steeves et al. [66]
$\approx 2wt\sqrt{k^{\text{c}} \cdot k^{\text{f}}}$	$wt(\frac{\pi^2 \cdot (t+c) \cdot E_f \cdot (k^{\text{c}})^2}{3 \cdot d_s})^{1/3}$	$wt(\frac{\pi^2 \cdot (t+c) \cdot E_f \cdot (k^{\text{c}})^2}{3 \cdot d_s})^{1/3}$

Table 17: Critical failure loads F_{cr} for core indentation.

The formulae for the estimation of the critical failure loads F_{cr} for core shear are shown in Table 18. Steeves et al. do not account for the influence of the face sheets and

are therefore disregarded. Ashby and Mohan and their colleagues use similar formulae for the failure load F_{cr} which only slightly vary in the weighting of the contribution of the face sheets. In the following, the relation provided by Mohan et al. is used since it yields slightly lower failure loads and therefore offers additional safety in the estimation. The formulae refer to the core shear collapse mode A (cf. e.g. [21]) which occurs for small overhangs d_o in relation to the span d_s.

Ashby et al. [21]	Mohan et al. [69]	Steeves et al. [66]
$\frac{2 \cdot w \cdot t^2}{d_s} k^{\mathrm{f}} + 2wc\tau^{\mathrm{c}}(1 + \frac{2 \cdot d_o}{d_s})$	$\frac{4 \cdot w \cdot t^2}{3 \cdot d_s} k^{\mathrm{f}} + 2wc\tau^{\mathrm{c}}(1 + \frac{2 \cdot d_o}{d_s})$	$2w(c+t)\tau^{\mathrm{c}}$

Table 18: Critical failure loads F_{cr} for core shear ($d_o \ll d_s$).

Based on the selected formulae in Tables 16, 17 and 18, so called failure maps can be constructed. Thereby, variables of interest are varied inside a specific range whereas the remaining parameters are constants. In general, these variables can be geometric dimensions or material properties. In order to compare the formulae with the experimental findings, the material properties of the core material are varied. Analysis of the equations yields that the failure loads are dependent on the yield strength k^{c} and the shear strength τ^{c} of the core material. Furthermore, the onset of face wrinkling is also dependent on the stiffness E_{c} of the core material. A small stiffness of the core material favours the occurrence of this failure mode. However, preliminary analysis and the experimental findings show that the failure loads for face wrinkling are distinctly higher in comparison to competing failure modes. Accordingly, the yield strength of the core k^{c} is varied between 0.1 and 20 N/mm^2 and the shear strength of the core τ^{c} between 0.1 and 10 N/mm^2. The Young's modulus E_c of the core material is set to the minimum value of 85 N/mm^2 (M-Pore®) and the material properties of the aluminium face sheets are taken from Table 4. The geometric dimensions of the sandwich structure and of the experimental setup of the three-point bending test are the default values shown in Table 13 ($d_s = 250$ mm, $w = 30$ mm, $c = 30$ mm, $h = 32$ mm and $d_o = (l - d_s)/2 = 15$ mm).

Figure 97 shows a three dimensional plot of the competing failure loads F_{cr} in dependence on the variables core shear strength τ^{c} and core yield strength k^{c}. Each failure mode is represented by one surface and the z-coordinate of any point inside these surfaces is equal to the critical force F_{max}. The construction of the failure map requires only the minimum critical load at a particular point in the τ^{c} - k^{c} stress space. Therefore, simply the viewing direction is altered as indicated by the arrow in Fig. 97. As the result, the failure map shown in Fig. 98 is obtained. This graph can be used in order to identify the failure mode in dependence on the material properties of the core material. The different sandwich structures of the experimental analysis are marked by circular symbols (**O**). The shear strength of the core materials is generally

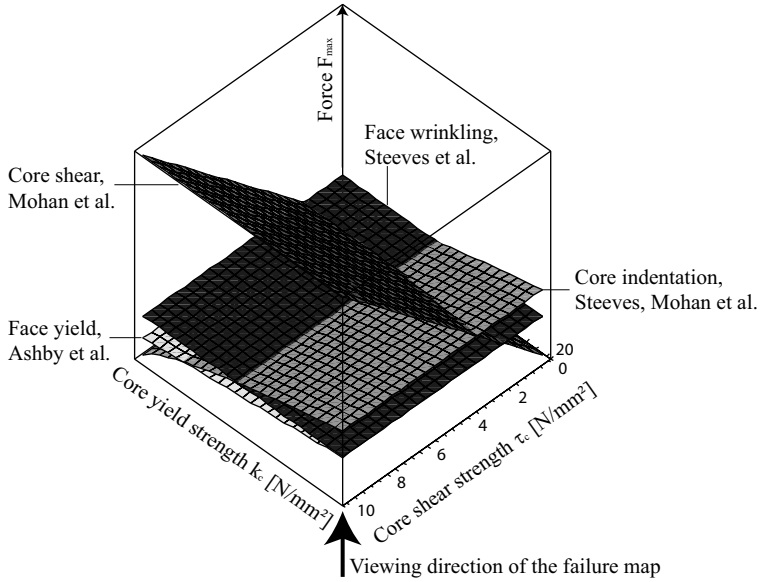

Figure 97: Three dimensional representation of the critical failure loads F_{cr} dependence on the core material.

unknown, but can be roughly estimated based on the yield strength by using the von Mises yield condition ($\tau_c = \sigma_c/\sqrt{3}$). Since the yield strength of the Alporas® and M-Pore® aluminium foams are identical, also their positions in this failure map coincide. The predicted failure mechanism core indentation is in agreement with the experimental results. The scaling of the failure map is adjusted so that all relevant failure mechanisms can be easily identified. Therefore, the position of the syntactic MHSS sandwich compound cannot by plotted in Fig. 98. However, the corresponding value lies clearly within the face yield / core fracture field of the failure map which is confirmed by the experimental findings. Finally, the partial MHSS sandwich structures are positioned in the transition zone between core indentation and core fracture. Again, this is in excellent agreement with the experimental results, where the specimens partially failed to core indentation (#12), core fracture (#10) or a combination of both mechanisms (#11).

Table 19 shows the quantitative comparison of predicted failure loads and experimental values. Poor agreement is found for the cellular metals Alporas® and M-Pore®. The predicted failure loads for partial MHSS are only slightly higher than the averaged experimental value. The estimation of the failure load for syntactic MHSS is based on a reduced tensile yield strength $k_t = 15$ N/mm^2 of the core material (cf. Section 4.2.2). The predicted values are in good agreement with the experimental findings. It can be concluded that the estimations shown in Tables 16, 17 and 18 can be applied for a qualitative prediction of the failure mode but are in general not suitable for a quantitative estimation of the failure load.

Fig. 98 is only valid for the earlier mentioned default geometric dimensions and

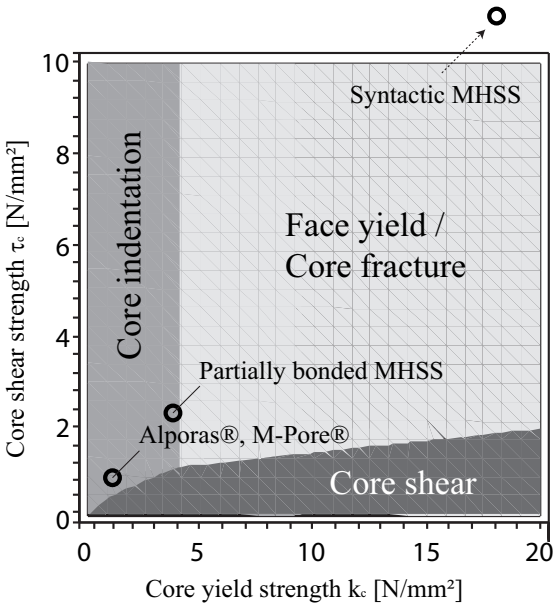

Figure 98: Failure map in dependence on the core material.

Core material	Estimation		Experimental results
	Core indentation [21]	Core fracture [66]	
	[N]	[N]	[N]
Alporas®	1248	-	1700
M-Pore®	1248	-	700
Partial MHSS	2298	2320	2100
Syntactic MHSS	-	3400	3300

Table 19: Estimated and experimental failure loads.

face sheet material Al5005. The dependence of the failure mode on the geometric dimensions total height h and length of the span d_s is shown in Fig. 99. All remaining geometric and material parameters exhibit their default values, i.e. face sheet thickness $t = 1$ mm. The considered case is a sandwich compound with an adhesively bonded MHSS core (partial morphology). The material properties of this low density core material are taken from Fig. 61 ($E = 340$ N/mm^2, $\sigma_c = 4$ N/mm^2) and the shear strength is calculated by using the VON MISES yield condition ($\tau_c = \sigma_c/\sqrt{3} = 2.3$ N/mm^2). It becomes clear that face wrinkling is not a relevant failure mechanism for this type of sandwich structures. For small spans d_s and small heights h core shear is the predominant failure mode. Increase of the height h favours the occurrence of core indentation, whereas a longer span d_s leads to face yield possibly followed by core fracture.

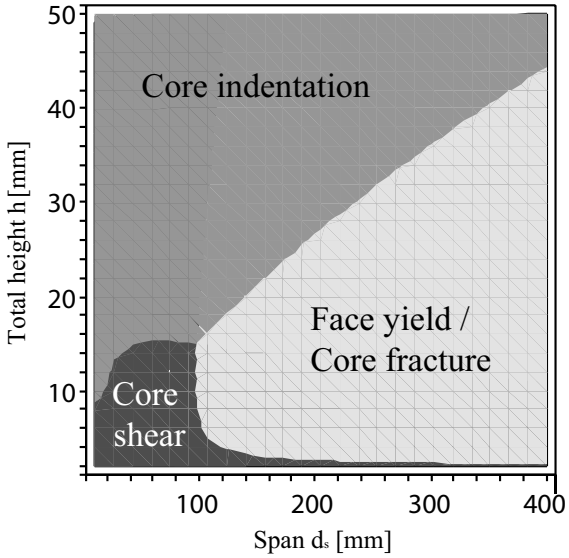

Figure 99: Failure map for varying geometric dimensions of a sandwich structure.

Energy absorption Due to the ability of cellular metals to absorb energy at constant and defined stress levels, their application in sandwich compounds is interesting for energy absorbing structures. Therefore, the energy absorption ability of the sandwich structures in Table 13 is determined and compared for quasi-static loading. The absorbed energy $W_{ab} = \int F \cdot \mathrm{d}u$ is equal to the areas under the force deflection curves in Figs. 90, 92, 94 and 96. Thereby, only the elastic and plastic ranges, confined by the maximum force $F_{\max}$, are considered (cf. Fig. 86). The results are shown in Table 20, where the $^+$ symbols indicate failure due to core indentation. In contrast to core fracture, this failure mode is non-catastrophic, i.e. the force does not suddenly decrease after reaching the maximum force $F_{\max}$. Therefore, these structures are able to absorb further energy if no kinematic constraints or global collapse prevent further deflection of the sandwich compounds.

As a consequence of the low forces in Fig. 92, the M-Pore®-aluminium foam sandwich structures absorb the smallest amount of energy. The Alporas® foam and the syntactic MHSS exhibit the second lowest average value of 3.7 N/mm^2. By comparing these two core materials, it must be considered that the Alporas® compounds fail due to core indentation and are able to absorb additional energy after failure initialisation. The syntactic MHSS structures show the minimum scattering of the material properties ($\overline{\rho} = 17\%$) and therefore higher predictability of impact behavior. The partial MHSS exhibit the second highest average value and a relatively low scattering (37%) in comparison with the other cellular metals Alporas® and M-Pore®. The scattering is mainly caused by the differing failure modes core fracture (#10, #11) and core indentation (#12) which is caused by the geometric dimensions of the sandwich structure (cf. Fig. 98). Based on these findings, the partial MHSS is potentially able to compete

ID	Core material	Absorbed Energy W_{tot} [J]	Average value [J]	Norm. stand. dev. $\overline{\delta}$ [%]
#1	Alporas®	2.3 +	3.7	47
#2		3.2 +		
#3		5.7 +		
#4	M-Pore®	0.8 +	1.3	71
#5		2.3 +		
#6		0.7 +		
#7	Honeycomb	7.4 +	5.8	30
#8		6.0 +		
#9		4.0 +		
#10	Partial MHSS	7.1	5.4	37
#11		6.0		
#12		3.2 +		
#13	Synt. MHSS	3.0	3.7	17
#14		3.9		
#15		4.2		

Table 20: Energy absorption W_{tot} of sandwich structures with different core materials.

with the honeycomb core material which exhibits the highest energy-absorbing ability among the materials investigated.

4.2.2 Mechanical Properties: Finite element approach

Finite element simulations of three-point bending tests are carried out. The used finite element models and boundary conditions are described in Section 3.1.3. The analysed sandwich structures are assembled by two Al5005 aluminium face sheets (for material properties cf. Table 4) which enclose partial or syntactic MHSS cores (for material properties cf. Appendix A). In addition to the linear-elastic ideal-plastic material model, a Fortran® user subroutine is programmed in order to simulate collapse or fracture inside the MHSS core material. Based on experimental findings, collapse of the hollow spheres is assumed, if the equivalent plastic strain $\varepsilon_{\text{eff}}^{\text{pl}}$ (15) exceeds a threshold of $\varepsilon_{\text{eff}}^{\text{pl}} \geq 0.06$ and that the first hydrostatic invariant J_1^o is negative (compressive stress state). Thereby, the plastic strain $\varepsilon_{\text{eff}}^{\text{pl}} = 0.06$ corresponds to the initial peak in the macroscopic stress-strain relations in Fig. 67. The finite elements which fulfill this criterium are deactivated, i.e. are erased from the stiffness matrix. A similar approach is applied for the simulation of core fracture. Under the condition that the first hydrostatic invariant J_1^o is positive (tensile stress state), fracture is simulated if the equivalent plastic strain exceeds $\varepsilon_{\text{pl}} > 0$. This condition simulates the brittle behaviour of the MHSS cores under tensile loading. The third competing failure mode

for MHSS cores, core shear, is not incorporated. The failure map Fig. 99 shows that this failure mechanism only occurs for small geometries and has therefore only little relevance for potential applications.

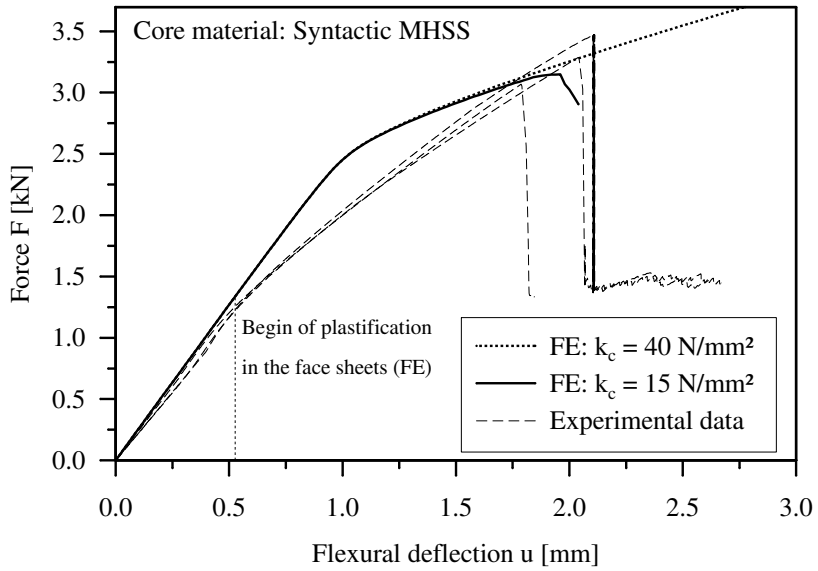

Figure 100: Numerical results of the three-point bending test of a sandwich structure with syntactic MHSS core.

In order to compare the numerical results to experimental findings, three dimensional finite element models with symmetric boundary conditions modelling the geometric dimensions shown in Table 13 are used. First, syntactic MHSS cores are considered. Figure 100 shows the force-displacement curves of the finite element analysis and the experimental tests. Good agreement is found within the linear elastic range. However, at the deflection $u \approx 0.5$ mm the gradients of the experimental curves decrease. Though the numerical results also show the onset of plastic deformation inside the aluminium face sheets at $u = 0.54$ mm, the numerical curve further increases linearly and the gradient only slowly decreases at higher deflections. This deviation of the numerical results is probably caused by neglecting the influence of the hydrostatic stress state on the yield strength of the core material, high strains and deformations and slightly inaccurate material data of the aluminium face sheets. Within the scope of the finite element analysis, different yield strength k of the syntactic core material are considered, whereas all remaining material parameters remain unchanged. For $k = 40$ N/mm^2 (experimental value k_c for compressive testing) no failure can be observed within the designated range. Therefore, the yield strength is varied and further analyses are carried out. The best agreement with the experimental data of the three-point bending test is found for $k = 15$ N/mm^2. It should be noted that the yield strength of the core material does not affect the characteristics of the curve but only the occurrence of failure, which is indicated by decrease of the force

$F_{\max}$. Figure 101 shows the distribution of the the equivalent VON MISES stress after core fracture.

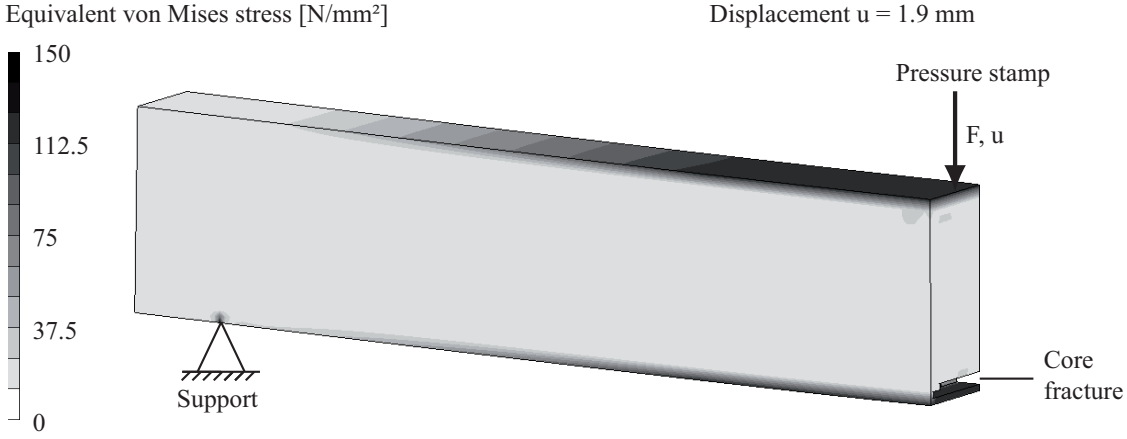

Figure 101: Distribution of the equivalent VON MISES stress in a sandwich panel with syntactic MHSS core after fracture ($k = 15$ N/mm^2).

The numerical three-point bending test is repeated for sandwich structures with partial MHSS cores. The corresponding force-displacement relations are shown in Fig. 102. The finite element analysis shows failure due to core indentation followed by core fracture and is in good agreement with the experimental findings. Also the force-displacement curves of numerical and experimental testing show good agreement, in particular in respect to specimen #12 which failed due to core indentation. The

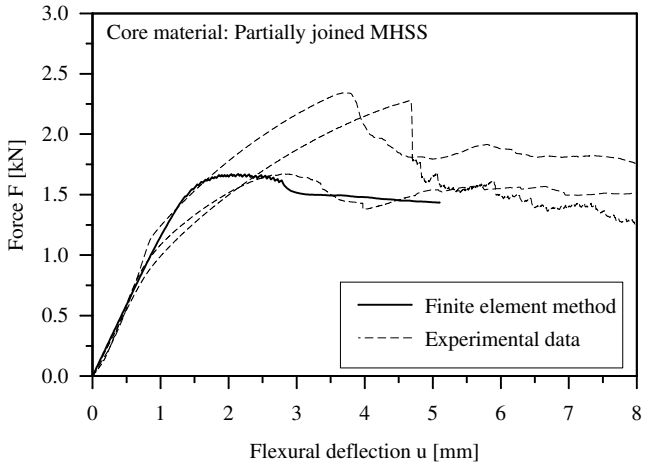

Figure 102: Numerical results of the three-point bending test of a sandwich structure with partial MHSS core.

distribution of equivalent VON MISES stress at the beginning of core indentation is shown in Fig. 103. A local concentration of stresses in the face sheets in the centre of the specimen can be observed.

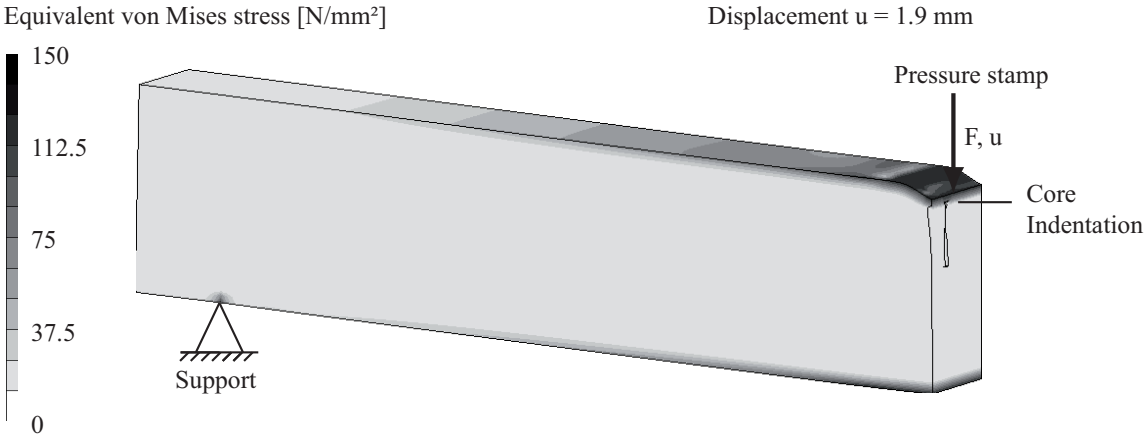

Figure 103: Equivalent VON MISES stress in a sandwich panel with partial MHSS core during core indentation.

In conclusion, it can be noted that the finite element models can be used to predict the failure mode and approximate force-displacement behavior of sandwich structures with MHSS cores. However, complex mechanisms in the microstructure of the core material, such as buckling of the spheres or local delamination of matrix and metallic spheres, are difficult to incorporate in the numerical model. The suggested deactivation of 'failed' elements only gives qualitative information of the mechanical behaviour of the structure after failure, but cannot be used to predict quantitative results. Therefore, the numerical results of the three-point bending test should be merely interpreted as design guidelines which need to be verified by experimental testing.

4.2.3 Minimum weight design

In the following section, some general guidelines for the minimum weight design of sandwich structures with MHSS cores under three-point bending loading are developed. Minimum weight design can be considered as an optimisation problem. The performed optimisation process depends on two variables; the face sheet thickness t and the core height h. The remaining geometric dimensions are constants ($d_s = 250$ mm, $d_o = 15$ mm, $w = 30$ mm). The material properties of the Al5005 face sheets are shown in Table 4 and the mechanical properties of the MHSS are taken from the experimental results.

The aim of the optimisation is to find the minima of the mass function

$$m = 2 \cdot \rho_{\mathrm{f}} \cdot w \cdot (d_s + 2 \cdot d_o) \cdot t + \rho_{\mathrm{c}} \cdot w \cdot (d_s + 2 \cdot d_o) \cdot h, \tag{74}$$

while certain constraints are fulfilled. Two different type of constraints can be identified. First the sandwich structure must be able to support a minimum load $F_{\min}$. This load is typically the expected maximum load multiplied by a safety factor.

All relevant failure loads F_{cr} of the structure must exceed this minimum load $F_{\min}$. Accordingly, the following constraints must be fulfilled:

$$\begin{aligned}
&\text{Core fracture [21]:} && F_{\mathrm{cr}} = \tfrac{4 \cdot w \cdot t \cdot (c+t)}{d_s} k^{\mathrm{f}} \geq F_{\min} \\
&\text{Core indentation [69, 66]:} && F_{\mathrm{cr}} = w \cdot t (\tfrac{\pi^2 \cdot (t+c) \cdot E_f \cdot (k^{\mathrm{c}})^2}{3 \cdot d_s})^{1/3} \geq F_{\min} \\
&\text{Core shear [69]:} && F_{\mathrm{cr}} = \tfrac{4 \cdot w \cdot t^2}{3 \cdot d_s} k^{\mathrm{f}} + 2wc\tau^{\mathrm{c}}(1 + \tfrac{2 \cdot d_o}{d_s}) \geq F_{\min}
\end{aligned} \tag{75}$$

In addition, an upper limit for the deflection $u_{\max}(F_{\min})$ can be prescribed. The largest deflection of the sandwich structure under three-point bending loading occurs in the centre at $x = 0$ (cf. Fig. 34). This deflection can be estimated based on Eq. (56), after replacing the flexural rigidity of a homogeneous material $D_h = E_{\mathrm{Str}} \cdot I_{zz}$ by the flexural rigidity D_{Str} of a sandwich structure (66). Now, the evaluation of the equation at the point $x = 0$ yields the deflection constraint

$$\frac{F_{\min} \cdot d_s^3}{4 \cdot w \cdot (8 \cdot E_f \cdot t^3 + 6 \cdot E_f \cdot t \cdot c^2 + 12 \cdot E_f \cdot t^2 \cdot c + E_c \cdot c^3)} \leq u_{\max}(F_{\min}). \tag{76}$$

The solution of the optimisation problem is achieved using the commercial software Maple 9.5. In this software, the function *NLPSolve* is used to compute the local minima of non-linear problems [124], i.e. for non-linear constraints (75), (76). The results for sandwich structures with partial MHSS cores ($E^{\mathrm{c}} = 340$ N/mm^2, $k^{\mathrm{c}} = 4$ N/mm^2, $\tau^{\mathrm{c}} \approx k_c/\sqrt{3} \approx 2.3$ N/mm^2, $\overline{\rho}_c = 0.3$ g/cm^3) are shown in Fig. 104. The face sheet thicknesses t of the minimum weight designs are plotted versus the core heights h. Three cases are shown. The line with circular symbols represents optimised sandwich structures which are only constrained by their failure loads (75) and where no deflection constraint is defined ($u_{\max} =$ infinite). The result show a linear dependence between the face sheet thickness and core height that passes through the origin and has a gradient $\Delta t/\Delta h = 0.0625$. All the optimum weight designs fail due to the failure mode face yield / core fracture.

Furthermore, two lines for the constant limit loads $F_{\min} = 500, 1000$ N/mm^2 are drawn, where additional deflection constraints $u_{\max}(F_{\min})$ are defined. It is found that for small values of $u_{\max}$, the results for both limit loads lie on a straight line that passes through the origin and has a gradient $\Delta t/\Delta c = 0.0290$. By investigating the minimum load constraints (75) it becomes apparent that the values on the left side of the inequalities are higher than the required minimum force ($F_{\mathrm{cr}} > F_{\min}$). Therefore, the structures are over-dimensioned in relation to their load carrying ability and the minimum mass is limited by the deflection constraint (76) alone. If the maximum possible deflection $u_{\max}(F_{\min})$ is increased, the data points enter the transition zone which

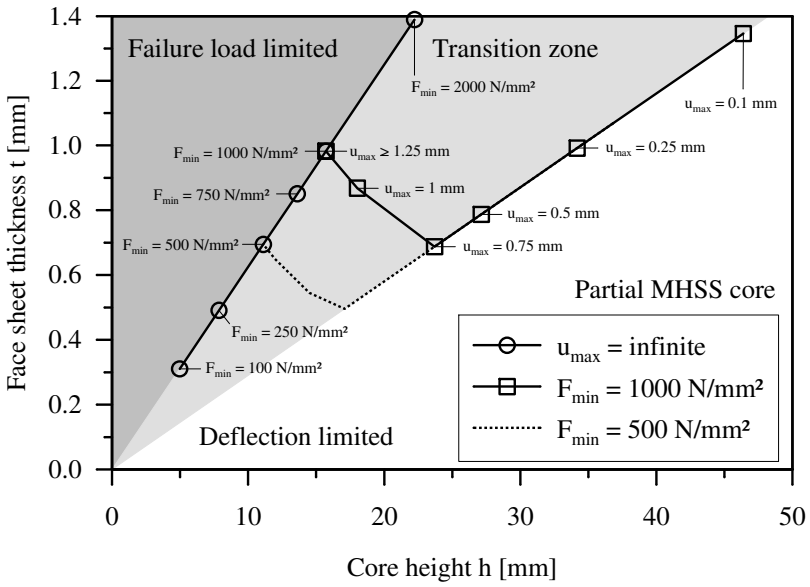

Figure 104: Minimum weight design for sandwich structures with partial MHSS cores and Al5005 face sheets.

is shown as a light grey area (e.g. $\square$, $u_{\max}(1000\ \mathrm{N/mm^2}) = 1$ mm) in Fig. 104. Within this area, the geometry of the sandwich structure is constrained both by the minimum load and the maximum deflection and no corresponding constant ratio $\Delta t/\Delta c$ for an optimum design can be derived. However, if $u_{\max}(F_{\min})$ exceeds a threshold (e.g. $u_{\max}(1000\ \mathrm{N/mm^2}) \gtrsim 1.25$ mm), the deflection constraint becomes too weak to influence the solution of the optimisation problem. The results become identical to the first reference case ($u_{\max} = \infty$) and are therefore only limited by their failure loads.

Figure 105 shows the masses of the minimum weight designs plotted against the load constraint $F_{\min}$ or the deflection constraint $u_{\max}$ if it is defined. The curve between the blank an the shaded region shows how the optimisation behaves under only minimum load constraints (75) with imposed values of $F_{\min}$. It can be observed that the mass is only slightly increased by increasing the required minimum load-carrying capacity $F_{\min}$. Furthermore, the graphs for the minimum loads $F_{\min} = 1000\ \mathrm{N/mm^2}$ (dash-dotted line) and $F_{\min} = 500\ \mathrm{N/mm^2}$ (dotted line) are drawn versus the maximum tolerable deflection $u_{\max}$. When the deflection constraint $u_{\max}$ is small, a large mass of the sandwich structure is required to fulfill the condition. However, if the deflection constraint is increased, the total mass shown in Fig. 105 required to achieve sufficient structural stiffness tends to the curve for $u_{\max} \to \infty$ for the respective minimum load $F_{\min}$.

Based on these findings, it is possible to derive design guidelines for minimum weight requirements for sandwich structures. When only the failure load is critical

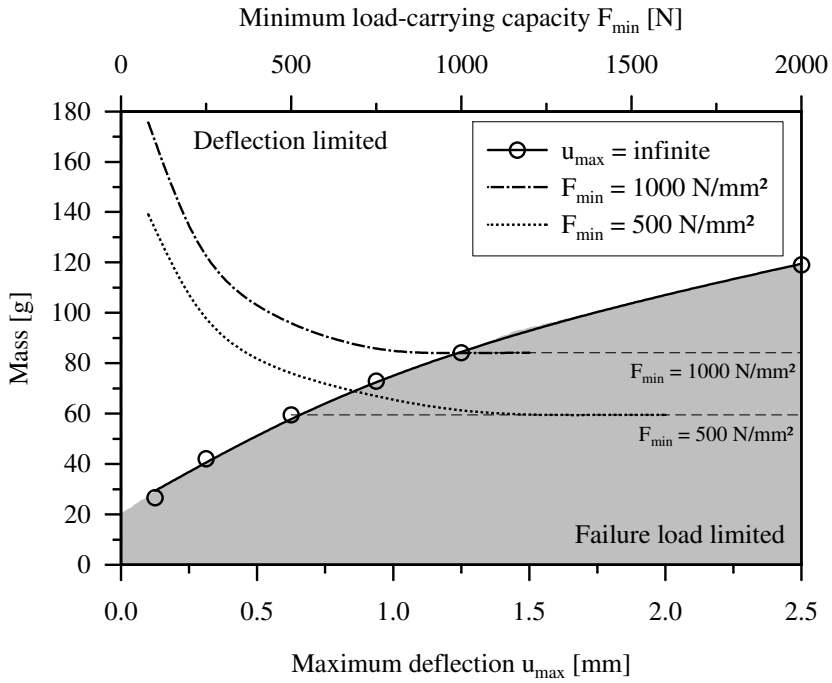

Figure 105: Minimum masses of sandwich structures with partial bond MHSS core and Al5005 face sheets.

and no deflection constraint is required, a ratio of $t/c = 0.0625$ yields the optimum solution. The condition for core fracture in Eqs. (75) can be used to calculate the values for the face sheet thickness t and the core height c. If additionally a deflection constraint is defined, the ratio $t/c = 0.0290$ should be chosen instead. The core height c and face sheet thickness t can then be calculated with the deflection constraint (76). In the next step, it is essential to ensure that the obtained minimum weight design fulfills all load constraints in Eqs. (75). If the particular sandwich structure lies within the transition zone or a different failure mode than core fracture is predominant, this procedure cannot be used. Furthermore, this guideline is only valid for the geometric dimensions defined above and combination of face sheet and core material. Therefore, it is advantageous to apply the described optimisation algorithm using suitable software (e.g. MAPLE) in order to determine the optimum geometry of arbitrary sandwich structures under three-point bending.

4.2.4 Thermal Properties of sandwich structures

In the following, sandwich panels with MHSS cores acting as a thermal insulating layer are considered. The effective thermal conductivity is determined in the direction of the normal vector of the face sheets. The temperatures prescribed at the upper and lower surfaces are 293 K and 433 K respectively. The microstructure of the

MHSS is homogenised and therefore represented by plane rectangular elements in order to reduce the required calculation time. As shown in section 4.1.4, the deviation introduced by this simplification is small. Figure 106 summarises the results of this investigation. The effective thermal conductivity is plotted versus the normalised face sheet thickness. This ratio is equal to the varying thickness t of the face sheets divided by the constant total height $h = 30$ mm of the structure and is defined for values between 0 (pure core material) and 0.5 (no core material, face sheets merge).

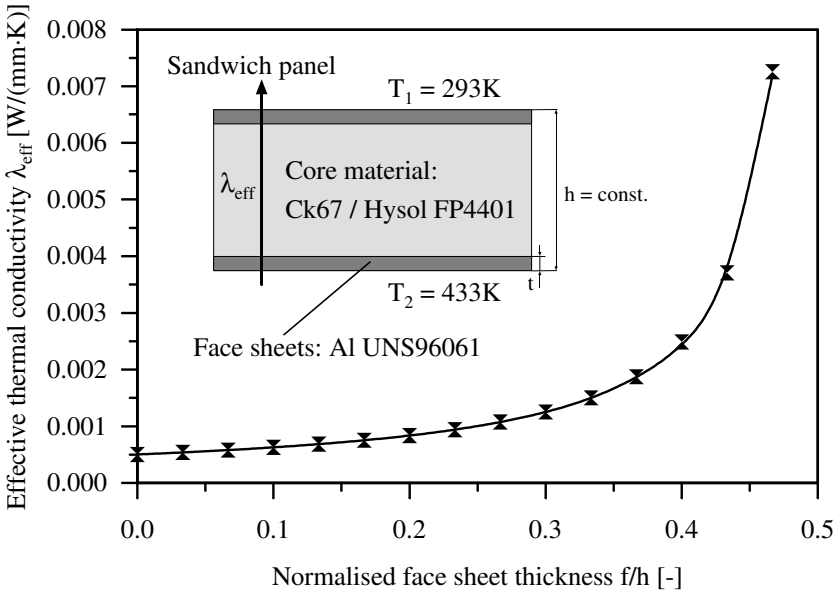

Figure 106: Thermal conductivity of sandwich panels with MHSS-cores in dependence on the normalised face sheet thickness.

The thermal conductivity of the sandwich structure increases with increasing relative thickness of the face sheets. This phenomenon can be explained with the high thermal conductivity of the aluminium alloy (cf. Fig. 29) in comparison to the insulating MHSS core material. Even in the case of very thin insulating layers ($t/h = 0.4$), the thermal conductivity of the sandwich panel only reaches ca. 1.5 % of the values of the face sheet material. However, for further decrease of the thickness of the core, the thermal conductivity of the structure grows exponentially.

Next, the adhesive layers joining face sheets and core material are incorporated in the numerical simulation. The overall height h of the structure is 30 mm and the face sheet thickness t is 1 mm. Two different adhesive interface layers with a thickness t_{adh} of 0.25 and 0.5 mm are considered. These interface layers exhibit the thermal properties of Hysol FP4401 which is multiplied by a scale factor $s = 0.8$, 1.0, 1.2 in order to account for a change of the material properties due to chemical reactions. The findings are shown in Table 21.

It can be seen that the influence of the interface layer on the overall thermal

t_{adh}	Scale factor s			Without interface layer
	0.8	1	1.2	
0.25 mm	0.582 W/(mm · K)	0.584 W/(mm · K)	0.585 W/(mm · K)	0.581 W/(mm · K)
0.5 mm	0.583 W/(mm · K)	0.587 W/(mm · K)	0.590 W/(mm · K)	0.581 W/(mm · K)

Table 21: Thermal conductivities of sandwich structures with adhesive interface layers.

conductivity is low. This result can be explained by the similar thermal conductivities of the adhesively bonded hollow sphere structure and the adhesive. The influence slightly increases with growing thickness t_{adh} of the adhesive interface layer.

5 Conclusions

The motivation of this work was the investigation of the performance of novel MHSS in sandwich panels. Numerical and experimental analysis of their mechanical and thermal properties were performed. In the first part of this thesis, the properties of single MHSS were determined. The second part addressed the mechanical and thermal properties of sandwich panels with MHSS cores.

Single metallic hollow sphere structures

Numerical and experimental quasi-static compressive tests of MHSS showed that their macroscopic stress-strain behaviour exhibits typical porous material characteristics. A linear-elastic range and a short elastic-plastic transition zone are followed by a stress plateau, where stress oscillations due to sphere walls buckling can be observed. At high strains, the inner surfaces of the spherical shells touch and the stress level quickly increases. Numerical analyses of the dependencies of the material parameters of MHSS on the morphology, topology and material composition yielded the following results:

- Partial MHSS exhibit superior specific material properties at low densities. At high densities, syntactic MHSS outperform the partial morphology. This transition occurs at the densities $\overline{\rho} \approx 0.65$ g/cm^3 for adhesively bonded MHSS and $\overline{\rho} \approx 1.1$ g/cm^3 for homogeneous MHSS.

- The material properties of adhesively bonded structures show only a weak dependence on the topology. In contrast, cast and sintered MHSS exhibit a strong dependence on the arrangement of spheres.

- The application of different sphere materials influences the macroscopic properties of MHSS. Higher specific properties of the sphere wall material are reflected in improved performance of MHSS. The substitution of sintered steel by sintered aluminium increases the specific stiffness, but decreases the specific initial yield stress

- The shapes of the yield surfaces of primitive cubic and adhesively bonded MHSS in the principal stress space were determined. Thereby, a strong dependency on the hydrostatic stress state was found. Consequently, the analysis of MHSS under complex multi-axial stress states requires the application of adjusted plasticity models.

- The isotropy of the linear-elastic behaviour of primitive cubic MHSS was demonstrated. It was found that primitive cubic partial MHSS exhibit only a weak dependence on the loading direction. The mechanical properties of primitive cubic syntactic MHSS proved to be independent of the loading planes.

In addition to the quasi-static tests, numerical analyses of the impact behaviour of syntactic MHSS were performed. Within these simulations, large deformations were simulated and strain rate effects of the metallic shells and the epoxy matrix were considered. Higher strain rates result in higher structure stiffness and corresponding stress levels. The MHSS capability of energy absorption thus increases with strain rate increase. Computational simulations show that it is possible to achieve different responses of MHSS when subjected to dynamic loading. The MHSS topology, sphere wall thickness and strain rate sensitivity can be combined so that the composite structure response is adapted to a given engineering problem.

The comparison of quasi-static numerical and experimental results showed good agreement for Young's modulus and the maximum stress. However, it was found that the symmetric boundary conditions of the finite element analysis do not allow for the occurrence of macroscopic deformation mechanisms at higher strains. The uniaxial compression of partial MHSS causes the formation of collapse band which form an angle of 30^o to 40^o with loading direction, whereas sliding bands with an angle of 45^o with the loading direction can be observed for syntactic MHSS. These effects cannot be captured by the numerical models and therefore at high plastic strains, deviations with the experimental data were found.

Next to the mechanical analysis, the thermal properties of single MHSS were investigated. It was found that MHSS generally exhibit low thermal conductivities and act as thermal insulators. Partial morphology further decreases the effective thermal conductivity and minimum values were obtained for adhesively bonded structures. Here, the epoxy resin acts as thermal insulator within the MHSS due to its low thermal conductivity. In the scope of these thermal analyses, temperature dependent properties of the base materials were also considered. The comparison of the numerical results and experimental findings, obtained by the transient plane source method, yielded good agreement.

MHSS in sandwich structures

The second part of this thesis addressed the mechanical and thermal properties of MHSS in sandwich panels. The emphasis of the mechanical analyses was put on the experimental three-point bending test. Sandwich structures with adhesively bonded MHSS cores were compared with classical honeycomb sandwiches and panels containing Alporas® and M-Pore® cellular metal cores.

- The highest absolute flexural stiffness of 10300 N/mm^2 was found for honeycomb structures, closely followed by sandwich structures with syntactic MHSS scores (9600 N/mm^2).

- Sandwich panels with honeycomb cores also exhibit the maximum specific flexural stiffness. The corresponding values of the adhesively bonded MHSS sandwich

structures are low in comparison to the competing core materials due to the poor specific stiffness of the adhesive.

- Among the investigated core materials, syntactic MHSS, followed by partial MHSS, exhibit the highest absolute load-carrying capacity.

- The highest specific load-carrying capacity was observed for honeycomb cores and partial MHSS core materials.

- Two different failure modes of the sandwich specimens were found. Sandwich structures with Alporas®, M-Pore® and honeycomb cores fail due to indentation of the pressure stamp in the core material. Core indentation is characterised by a slow decrease of the bearable force after failure initiation and therefore potentially safe without triggering sudden collapse. Catastrophic failure due to core fracture and subsequent delamination was observed for syntactic MHSS cores. The partial MHSS cores were found to be in the transition zone between core indentation and core fracture. Increase of the tensile strength of the adhesive bonding of MHSS or change of the geometric dimensions of the sandwich structure can change the failure mode to core indentation.

- Sandwich panels with honeycomb cores absorb the largest amount of energy (5.8 J) before failure initiation. Partial MHSS cores showed the ability to absorb the second highest energy of 5.4 J.

In addition to these experimental analysis, finite element simulations of the three-point bending tests were carried out. The occurrence of fracture and collapse in the MHSS cores was incorporated in these numerical analyses. Good agreement between the numerically obtained force-displacement curves and the experimental data was found. Furthermore, it was shown that the finite element method can be applied in order to identify the relevant failure mode. To this end, failure maps can be used as an alternative approach. Based on formulae in the literature, a failure map was generated in dependence on the mechanical properties of the core material. The predictions of the failure map were in good agreement with the experimentally observed failure modes. The same formulae used for the construction of the failure map form the basis for the minimum weight design of sandwich panels. This optimisation problem delivers the required geometry of a sandwich structure having minimum weight while fulfilling certain load and deflection constraints. This procedure was successfully demonstrated for the example of adhesively bonded partial MHSS cores.

In order to analyse the thermal properties of sandwich compounds with MHSS cores, the effective thermal conductivity of a sandwich structure in the normal direction of the face sheets was determined by the finite element method. Thereby, the core material was an adhesively bonded partial MHSS and a homogenization technique was

applied in order to limit the complexity of the model. It was found that the thermal conductivity of the sandwich is significantly lower compared with the conductivity of the face sheets, even for relatively thin cores.

As a final conclusion, MHSS in sandwich structures show potential for novel multifunctional applications. In particular, MHSS with partial morphology exhibit a high specific load-carrying capacity which enables its application in lightweight constructions. The poor specific stiffness of MHSS is caused by the low stiffness of the adhesive and the numerical results suggest that the application of alternative joining technologies such as sintering are able to correct this shortcoming and improve also the load carrying-capacity of MHSS. The results of the three-point bending test also indicate that MHSS sandwich compounds exhibit less scattering of material properties than the competing cellular metals Alporas® and M-Pore® which was a crucial limiting factor for the use of cellular metals. However, further analysis with bigger samples sizes are required in order to obtain reliable statistical data. Finally, the thermal analysis showed the applicability of MHSS as thermal insulators.

6 Future research work

Based on the findings of this thesis stimulus for further research includes the following points:

- The numerical analysis of MHSS requires the analysis of more realistic geometries without cubic symmetry. Therefore, the use of complex finite element meshes on clusters of computer of the next generation is suggested. As an alternative approach, different methods such as the Monte Carlo Grid method can be applied.
- The results for adhesively bonded hollow MHSS indicate the necessity for improvement of the adhesive bonding of the single hollow spheres. Parallel, the alternate joining technology sintering should be explored. The mechanical properties of these MHSS can be determined in experimental compressive and tensile testing.
- These new MHSS need to be investigated separately as cores in sandwich structures. Three-point bending tests with increased numbers of samples are proposed in order to obtain reliable statistical data.
- Further three-point bending tests with varying geometric dimensions of the sandwich specimens are suggested. The results of these tests can be used to control the predictions of geometrical failure maps and the minimum weight design guideline.
- In addition to these quasi-static tests, three-point bending tests at high strain rates are suggested in order to investigate the energy absorption capacity of MHSS in sandwich construction under impact conditions.
- Different loading conditions of the sandwich structures, i.e. four-point bending testing, should be analysed. Thus, material data of different load cases can be compared and dependencies on particular loading conditions can be identified.
- This thesis exclusively addresses the mechanical and thermal properties of MHSS. However, also their vibro-acoustic properties are of great interest and require future research.

References

[1] Metal foam. *News Composites*, 2:11, 1971.

[2] H. Bray. Design opportunities with metal foam. *Engineering Materials and Design*, 16:19, 1972.

[3] R.R. Barton, F.W.S. Carter, and T.A. Roberts. Use of reticulated metal foam as flash-back arrestor elements. *Chemical Engineer*, 291:708, 1974.

[4] J. Hamer. Honeycomb structure and its application to the concorde rudder. *Composites*, 2:242–245, 1971.

[5] S. Wilson. A new face of aerospace honeycomb. *Materials & Design*, 11:323–326, 1990.

[6] S. Vijayakumar. Parametric based design of CFRP honeycomb sandwich cylinder for a spacecraft. *Composite Structures*, 65:7–12, 2004.

[7] L. J. Gibson and M.F. Ashby. *Cellular Solids. Structure and Properties.* Cambridge, second edition, 1999.

[8] J. Banhart. Manufacture, characterisation and application of cellular metals and metal foams. *Progress in Materials Science*, 46:559–632, 2001.

[9] J. Baumeister. Überblick - Verfahren zur Herstellung von Metallschäumen. *An overview - processes for the manufacturing of metal foams. Werkstoffe, Technische Mitteilungen*, 92:94–99, 1999.

[10] T. Furio and M. Zoccala. The future of ship doors - lattice block materials. *published online*, 2001.

[11] A.G. Evans, J.W. Hutchinson, and M.F. Ashby. Multifunctionality of cellular metal systems. *Progress in Materials Science*, 43:171–221, 1999.

[12] S. L. Lopatnikov, B. A. Gama, and J. W. Gillespie. Modeling the progressive collapse behavior of metal foams. *International Journal of Impact Engineering*, 34:587–595, 2007.

[13] S. Nemat-Nasser, W.J. Kang, J.D. McGee, W.G. Guo, and J.B. Isaacs. Experimental investigation of energy-absorption characteristics of components of sandwich structures. *International Journal of Impact Engineering*, 34:1119–1146, 2007.

[14] I.S. Golovin and H.R. Sinning. Damping in some cellular metallic materials. *Journal of Alloys and Compounds*, 355:2–9, 2003.

[15] I.S. Golovinand H.R. Sinning. Internal friction in metallic foams and some related cellular structures. *Materials Science and Engineering A*, 370:504–511, 2004.

[16] R. Neugebauer, T. Hipke, J. Hohlfeld, and R. Thümmler. *Cellular Metals and Polymers*, chapter Metal Foam as a Combination of Lightweight Engineering and Damping, pages 13–18. Trans Tech Publications, 2005.

[17] J. Hübelt and G. Bingel. Excellent sound absorption by metallic hollow sphere structures. Technical report, Cellmet-News 1, 2006.

[18] T.J. Lu and C. Chen. Thermal transport and fire retardance properties of cellular aluminium alloys. *Acta Materialia*, 47:1469–1485, 1999.

[19] J.W. Paek, B.H. Kang, S.Y. Kim, and J.M. Hyun. Effective thermal conductivity and permeability of aluminium foam materials. *International Journal of Thermophysics*, 21:453–464, 2000.

[20] C.Y. Zhao, T.J. Lu, H.P. Hodson, and J.D. Jackson. The temperature dependence of effective thermal conductivity of open-celled steel alloy foams. *Materials Science and Engineering A*, 367:123–131, 2004.

[21] M. Ashby, N. Fleck, H. Wadley, J. Hutchinson, and L. Gibson. *Metal Foams: A Design Guide*. Boston: Butterworh-Heinemann, 2000.

[22] D.S. Schwartz, D.S. Shih, A.G. Evans, and H.N.G. Wadley, editors. *Porous and Cellular Materials for Structural Applications*, volume 521, San Francisco, 1998. MRS Spring Meeting.

[23] T. Fiedler, A. Öchsner, J. Grácio, and G. Kuhn. Structure modelling of the mechanical behaviour of regular shaped cellular solids: open-cell structures. *Mechanics of Composite Materials*, 41:405–422, 2005.

[24] R. Krez, E. Hombergsmeier, and K. Eipper. Manufacturing and testing of aluminium foam structural parts for passenger cars demonstrated by example of a rear intermediate panel. In *Conference Proceedings Metal Foams and Porous Structures*, 1999.

[25] H. Yoshimura, K. Shinagawa, Y. Sukegawa, and K. Murakami. Metallic hollow sphere structures bonded by adhesion. In *Proccedings of the 4^th International Conference on Porous Metals and Metal Foaming Technology*, Kyoto, Japan, 21-23 September 2005. METFOAM 2005.

[26] Alm GmbH. Big afs test structure for ariana rocket v booster. *Cellmet News*, page 4, 2006.

[27] J. Banhart, J. Baumeister, and M. Weber. *Aluminium, Jahrg. 70, Nr 3/4*, chapter Metallschaum - ein Werkstoff mit Perspektiven. *Metal foam - a material with future.*, pages 209–212. 1994.

[28] U. Ramamurty and A. Paul. Variability in mechanical properties of a metal foam. *Acta Materialia*, 52:869–876, 2004.

[29] M. Jäckel. *German Patent 3 724 156*. 1987.

[30] M. Jäckel. *German Patent 3 210 770*. 1983.

[31] T. Studnitzky and O. Andersen. *Cellular Metals and Polymers*, chapter Control of the carbon content in metal hollow sphere structures by variation of the debindering conditions, pages 143–146. Trans Tech Publications, 2005.

[32] A. Rousset, J.P. Bonino, Y. Blottiere, and C. Rossignol. *French Patent 8 707 440*. 1987.

[33] H.P. Degischer and B. Kriszt, editors. *Handbook of Cellular Metals*. WILEY-VCH, Weinheim, 2002.

[34] *published online*. NPL National Physics Laboratory, Teddington.

[35] E. Baumeister. *Hohlkugelkomposit - Charakterisierung thermischer und mechanischer Eigenschaften eines neuen Leichtbauwerkstoffes. Hollow sphere composite - characterisation of thermal and mechanical properties of a new lightweight material.* PhD thesis, Otto von Guericke University of Magdeburg, 2004.

[36] E. Baumeister, S. Klaeger, and A. Kaldos. Lightweight, hollow-sphere-composite (hsc) materials for mechanical engineering applications. *Journal of Materials Processing Technology*, 155-156:1839–1846, 2004.

[37] K. Boomsma, D. Poulikakos, and F. Zwick. Metal foams as compact high performance heat exchangers. *Mechanics of Materials*, 35:1161–1176, 2003.

[38] W. Lu, C.Y. Zhao, and S.A. Tassou. Thermal analysis on metal-foam filled heat exchangers. part 1: Metal-foam filled pipes. *International Journal of Heat and Mass Transfer*, 49:2751–2761, 2006.

[39] J.K. Paik, A.K. Thayamballi, and G.S. Kim. The strength characteristics of aluminum honeycomb sandwich panels. *Thin-Walled Structures*, 35:205–231, 1999.

[40] H. Seibert. Applications for pmi foams in aerospace sandwich structures. *Reinforced Plastics*, 50:44–48, 2006.

[41] G. Belingardi, M.P. Cavatorta, and R. Duella. Material characterization of a composite-foam sandwich for the front structure of a high speed train. *Composite Structures*, 61:13–25, 2003.

[42] J.S. Kim, S.J. Lee, and K.B. Shin. Manufacturing and structural safety evaluation of a composite train carbody. *Composite Structures*, 78:468–476, 2007.

[43] E.M. Knox, M.J. Cowling, and I.E. Winkle. Adhesively bonded steel corrugated core sandwich construction for marine applications. *Marine Structures*, 11:185–204, 1998.

[44] S. Reuterlöv. Cost effective infusion of sandwich composites for marine applications. *Reinforced Plastics*, 46:30–34, 2002.

[45] H.G. Allen. *Analysis and Design of Structural Sandwich Panels*. Pergamon Press, New York, 1969.

[46] M.J. Silva and L.J. Gibson. The effects of non-periodic microstructure and defects on the compressive strength of the two-dimensional cellular solids. *International Journal of Mechanical Sciences*, 39:549–563, 1997.

[47] E. Wu and W.S. Jiang. Crush of honeycombs contact and impact loads. In *Proc. of The 10th Internat. Conf. on Composite Materials*, volume 5, pages 567–574, 1995.

[48] E. Wu and S. Jiang. Axial crush of metallic honeycombs. *International Journal of Impact Engineering*, 19:439–456, 1997.

[49] Hilary Bart-Smith. *Metallic Foams: Performance and Use in Ultralight Sandwich Structures*. PhD thesis, Harvard University, Cambridge, Massachusetts, August 2000.

[50] B. Sosnik. *US Patent 2 434 775,*. 1948.

[51] J.C. Elliot. *US Patent 2 751 289*. 1956.

[52] D.J. Sypeck, P.A. Parrish, and H.N.G. Wadley. Porous and cellullar materials for structural applications. *Materials Research Society Proceedings*, 521:205, 1998.

[53] L.B. Torobin. *US Patent 4 671 909*. 1987.

[54] M. Jäckel. *German Patent 3 210 770*. 1982.

[55] T.J. Lim, B. Smith, and D.L. McDowell. Behaviour of a random hollow sphere metal foam. *Acta Materialia*, 50:2867–2879, 2002.

[56] S. Gasser, F. Paun, A. Cayzeele, and Y. Bréchet. Uniaxial tensile elastic properties of a regular stacking of brazed hollow spheres. *Scripta Materialia*, 48:1617–1623, 2003.

[57] W.S. Sanders and L.J. Gibson. Mechanics of hollow sphere foams. *Materials Science and Engineering A*, 347:70–85, 2003.

[58] W.S. Sanders and L.J. Gibson. Mechanics of bcc and fcc hollow-sphere foams. *Materials Science and Engineering A*, 352:150–161, 2003.

[59] S.E. Benzley, E. Perry, K. Merkle, B. Clark, and G.F. Sjaardema. A comparison of all-hexagonal and all-tetrahedral finite element meshes for elastic and elastic-plastic analysis. In *Fourth International Meshing Roundtable*, pages 179–191, Albuquerque, New Mexico, 1995.

[60] T. Fiedler, B. Sturm, A. Öchsner, J. Gracio, and G. Kuhn. Modelling the mechanical behaviour of adhesively bonded and sintered hollow sphere structures. *Mechanics of Composite Materials*, 42:559–570, 2006.

[61] H. Zhao, I. Elnasri, and S. Abdennadher. An experimental study on the behaviour under impact loading of metallic cellular materials. *International Journal of Mechanical Sciences*, 47:757–774, 2005.

[62] L. Sauve. *The use of sandwich structures in airplane construction.* Fullerton CA: Aircraft Spruce and Speciality Co., 1972.

[63] V.V. Vasiliev. *Mechanics of Composite Structures.* CRC, 1993.

[64] H. Bart-Smith, J.W. Hutchinson, and A.G. Evans. Measurement and analysis of the structural performance of cellular metal sandwich construction. *International Journal of Mechanical Sciences*, 43:1945–1963, 2001.

[65] C. A. Steeves and N. A. Fleck. Collapse mechanisms of sandwich beams with composite faces and a foam core, loadedin three-point bending. part i: analytical models and minimum weight design. *International Journal of Mechanical Sciences*, 46:561–583, 2004.

[66] C.A. Steeves and N.A. Fleck. Collapse mechanisms of sandwich beams with composite faces and a foam core, loaded in three-point bending. part ii: experimental investigation and numerical modelling. *International Journal of Mechanical Sciences*, 46:585–608, 2004.

[67] V.S. Deshpande and N.A. Fleck. Collapse of truss core sandwich beams in 3-point bending. *International Journal of Solids and Structures*, 38:6275–6305, 2001.

[68] H.N.G. Wadley, N.A. Fleck, and A.G. Evans. Fabrication and structural performance of periodic cellular metal sandwich structures. *Composites Science and Technology*, 63:2331–2343, 2003.

[69] K. Mohan, Y.T. Hon, S. Idapalapati, and H.P. Seow. Failure of sandwich beams consisting of alumina face sheet and aluminium foam core in bending. *Materials Science and Engineering A*, 409:292–301, 2005.

[70] Arnaud Pollien, Yves Conde, Laurent Pambaguian, and Andreas Mortensen. Graded open-cell aluminium foam core sandwich beams. *Materials Science and Engineering A*, 404:9–18, 2005.

[71] Altenbach J. and Altenbach H. *Einführung in die Kontinuumsmechanik. Introduction in the continuum mechanics.* B.G. Teubner, Stuttgart, 1994.

[72] G. Backhaus. *Deformationsgesetze. Laws of deformations.* Akademie-Verlag Berlin, 1983.

[73] Betten J. *Kontinuumsmechanik.* Continuum mechanics. Springer-Verlag, Berlin, 2001.

[74] R. J. Green. A plasticity theory for porous solids. *International Journal of Mechanical Sciences*, 14:215–224, 1972.

[75] Hahn J.G. *Elastizitätstheorie. Elasticity theorie.* B.G. Teubner, Stuttgart, 1985.

[76] W.-F. Chen and D. J. Hahn. *Plasticity for Structural Engineers.* Springer, New York, 1988.

[77] J. Hallquist. *Keyword manual.* Livermore Software Technology Corporation, Livermore, 2003.

[78] W.F. Chen and G.Y. Baladi. *Soil Plasticity.* Elsevier, Amsterdam, 1985.

[79] W.F. Chen. *Plasticity in Reinforced Concrete.* McGraw-Hill Book Company, 1982.

[80] J.C. Simo and T.J.R. Hughes. *Computational Inelasticity.* Springer-Verlag, New York, 1998.

[81] D.C. Drucker. *Proc. 1st U.S. Natn. Cong. Appl. Mech. Michigan*, chapter A more fundamental approach to plastic stress-strain relations, pages 487–491. Edwards Brothers INC, 1952.

[82] P. Jacob and L. Goulding. *An Explicit Finite Element Primer.* NAFEMS Ltd., Glasgow, 2002.

[83] J. Hallquist. *Theoretical manual.* Livermore Software Technology Corporation, Livermore, 1998.

[84] S.R. Bodner and P.S. Symonds. Experimental and theoretical investigation of the plastic deformation of cantilever beam subjected to impulse loading. *Journal of Applied Mechanics*, 29:719–728, 1962.

[85] R.C. Picu, G. Vincze, F. Ozturk, J. Grácio, F. Barlat, and A.M. Maniatty. Strain rate sensitivity of the strain rate sensitivity of the commercial aluminium alloy aa5182-ocommercial aluminium alloy aa5182-o. *Materials Science and Engineering A*, 390, 2005.

[86] Ohrndorf A., Schmidt, Krupp U., and Christ H.J. *Mechanische Untersuchung eines geschlossenporigen Aluminiumschaums. Mechanical investigation of a closed-pore aluminium foam.* Deutscher Verband für Materialforschung und Prürfung e.V., Bad Nauheim, 2000.

[87] F.P. Incropera and D.P. DeWitt. *Fundamentals of Heat and Mass Transfer.* John Wiley & Sons, 4 edition, 1996.

[88] J.P. Holman. *Heat Transfer.* Tata McGraw-Hill Publishing Company Ltd., 9 edition, 2004.

[89] B. Klein. *FEM Grundlagen und Anwendungen der Finite-Element-Methode. FEM Basics and applications of the finite element method.* Friedrich Vieweg & Sohn Verlag, 2003.

[90] R. Zurmühl. *Praktische Mathematik. Applied mathematics.* Springer-Verlag, 1954.

[91] B. Sturm. Numerische Untersuchung von Hohlkugelstrukturen mit homogenen und heterogenen Materialeigenschaften. *Numerical investigation of hollow sphere structures with homogeneous and heterogeneous material properties. Student project, Univeristy of Erlangen-Nuremberg, Germany*, 2006.

[92] O.C. Zienkiewicz and F.C. Scorft. On the principle of repeatability and its application in analysis of turbine and pump impellers. *International Journal for Numerical Methods in Engineering*, 4:445–452, 1972.

[93] R.D. Cook, D.S. Malkeis, M.E. Plesha, and R.J. Witt. *Concepts and Applications of Finite Element Analysis.* John Wiley & Sons, New York, 2002.

[94] A. Öchsner and J. Grácio. On the macroscopic thermal properties of syntactic metal foams. *Multidiscipline Modeling in Materials and Structures*, 1:171–181, 2005.

[95] C.P. Ling, M.B. Bush, and D.S. Perera. The effect of fabrication techniques on the properties of al-sic composites. *Journal of Materials Processing Technology*, 48:325–331, 1995.

[96] M. Vesenjak, T. Fiedler, Z. Ren, and A. Öchsner. Impact behaviour of composite hollow sphere structures. *Journal of Composite Materials*, submitted for publication.

[97] J.P. Jeandrau. Analysis and design data for adhesively bonded joints. *Adhesion and Adhesives*, 11:71–79, 1991.

[98] J.G. Kaufman, editor. *Properties of Aluminium Alloys*. ASM and the Aluminium Association of America, 1999.

[99] *Data Sheet*. Enterprise Gleich GmbH, Kaltenkirchen, Germany.

[100] D. Gierlich, C. Kühn, K. Hackeschmidt, and R. Riedl. Mechanische Kenndaten offenpooriger Aluminiumschäume. *Mechanical parameters of open-cell aluminimum foams. Konstruktion*, 9:69–74, 2004.

[101] Gerd Habenicht, editor. *Kleben Grundlagen, Technologien, Anwendung. Adhesive bonding basics, technologies, application.* Springer-Verlag, New York, 2002.

[102] *Military Handbook - MIL-HDBK-5H*. U.S. Department of Defence, USA, 1998.

[103] MSC Software Corporation. *MSC.Marc 2005 R2, material database*, 2005.

[104] A. Nyilas, R. Rehme, C. Wyrwich, H. Springer, and G. Hinrichsen. Thermal diffusivity and conductivity of highly filled epoxies as cover materials for microelectronical devices as measured by the heat pulse technique. *Journal of Materials Science Letters*, 15:1457, 1996.

[105] K. Hoffmann. *An Introduction to Measurements using Strain Gages*. Hottinger Baldwin Messtechnik GmbH, Darmstadt, 1989.

[106] C. Wheatstone. An account on several new instruments and processes for determining the constants of a voltaic circuit. *Philosophical Transactions of the Royal Society of London*, 1843.

[107] K. Hoffmann. Zum Linearitätsfehler bei Dehnungsmessungen mit Dehnungsmeßstreifen im Hochdehnungsbereich. *On the linearity error of strain gauges at high strains. Messtechnische Briefe*, 12:53–57, 1976.

[108] M. Kreuzer. Lineritäts- und Empfindlichkeitsfehler beim Messen mit Einzeldehnungsmeßstreifen bei spannungsgespeisten und stromgespeisten Schaltungen. *Linearity and sensitivity errors for measurement with single strain gauges with voltage-fed and current-fed circuits. Messtechnische Briefe*, 19:37–42, 1983.

[109] M. Kreuzer. Praktische Bedeutung der effektiven Dehnung für die Schaltungstechnik von Dehnungsmeßgeräten. *Practical importance of the effective strain for the circuitry of strain measuring instruments. VDI-Berichte*, 514:121–127, 1984.

[110] *German industrial standard DIN 50110.* 1962.

[111] T. Sato, K. Katagiri, T. Hokari, Y. Hatakeyama, A. Murakami, A. Nyilas, K. Kasaba, H. Teshima, and H. Hirano. Evaluation of youngs modulus of re123 bulk superconductors by three point bending tests. *Physica C*, 445-448:422–426, 2006.

[112] O. Almanza, M.A. Rodriguez-Pérez, and J.A. de Saja. Applicability of the transient plane source method to measure the thermal conductivity of low-density polyethylene foams. *Journal of Polymer Science: Part B: Polymer Physics*, 42:1226, 2004.

[113] E. Solórzano, M.A. Rodríguez-Pérez, J.A. Reglero, and J.A. de Saja. Density gradients in aluminium foams: Characterisation by computed tomography and measurements of the effective thermal conductivity. *Journal of Materials Science*, 2007, in press.

[114] T. Log and S. E. Gustafsson. Transient plane source (tps) technique for measuring thermal transport properties of building materials. *Fire and Materials*, 19:43–49, 1995.

[115] M. Gustavsson, E. Karawacki, and S.E. Gustafsson. *Review Science Instruments*, 12:3856–3859, 1994.

[116] T. Fiedler, A. Öchsner, J. Gracio, and G. Kuhn. Structural modeling of the mechanical behavior of periodic cellular solids: Open-cell structures. *Mechanics of Composite Materials*, 3:277–290, 2005.

[117] V.P.W. Shim, K.Y. Yap, and W.J. Stronge. Effects of nonhomogeneity, cell damage and strain rate on impact crushing of a strain-softening cellular chain. *International Journal of Impact Engineering*, 12:585–602, 1992.

[118] V.P.W. Shim and K.Y. Yap. Modelling impact deformation of foam-plate sandwich systems. *International Journal of Impact Engineering*, 19:615–636, 1997.

[119] M. Vesenjak, A. Öchsner, and Z. Ren. Behaviour of closed-cell foams under impact. In *Workshop on Computational Engineering Mechanics*, Erlangen, Germany, 2005.

[120] M. Vesenjak. *Computational simulations of cellular structures under dynamic loading.* PhD thesis, University of Maribor: Faculty of Mechanical Engineering., 2006.

[121] Loctite®. *Technical datasheet Hysol® FP4401*, 1986.

[122] C. Chen, A.M. Harte, and N.A. Fleck. The plastic collapse of sandwich beams with a metallic foam core. *International Journal of Mechanical Sciences*, 43:1483–1506, 2001.

[123] V. Crupi and R. Montanini. Aluminium foam sandwiches collapse modes under static and dynamic three-point bending. *International Journal of Impact Engineering.* In press.

[124] Software Maple 9.51 Internal Software Assistance. Maplesoft, 2004.

[125] K. Lamprecht. Numerische Simulation zellularer Werkstoffe. *Numerical simulation of cellular materials.* Master's thesis, University of Erlangen-Nuremberg, 2002.

[126] A. Öchsner. *Experimentelle und numerische Untersuchung des elasto-plastischen Verhaltens zellularer Modellwerkstoffe. Experimental and numerical investigation of the elastic-plastic behavior of cellular model materials.* PhD thesis, University of Erlangen-Nuremberg, 2003.

[127] I.N. Bronstein, K.A. Semendjajew, G. Musiol, and H. Mühlig. *Taschenbuch der Mathematik. Handbook of mathematics.* Harri Deutsch Verlag, 4 edition, 1999.

Appendix A - Mechanical Properties of MHSS

Morphology	Topology	t [mm]	ρ [g/cm^3]	E [N/mm^2]	ν [-]	k_c [N/mm^2]	k_t [N/mm^2]
Partial	pc	0.030	0.20	260	0.11	1.4	1.1
		0.052	0.31	420	0.10	2.3	1.9
		0.075	0.41	560	0.09	3.0	2.7
		0.113	0.58	750	0.09	4.0	3.8
		0.150	0.75	920	0.08	4.9	5.0
	bcc	0.030	0.28	580	0.07	1.4	1.4
		0.052	0.42	740	0.13	2.4	2.4
		0.075	0.56	830	0.18	3.4	3.4
		0.113	0.78	920	0.22	5.4	5.4
		0.150	0.99	980	0.25	7.2	5.4
	fcc	0.030	0.35	570	0.14	2.0	1.6
		0.052	0.50	730	0.17	3.2	1.7
		0.075	0.65	830	0.18	3.3	1.8
		0.113	0.89	950	0.19	3.6	2.0
		0.150	1.12	1030	0.20	3.7	2.0
Syntactic	pc	0.030	0.86	2400	0.35	8.6	8.6
		0.052	0.97	2890	0.35	11.5	11.5
		0.075	1.08	3270	0.35	13.9	13.9
		0.113	1.25	3810	0.34	17.2	17.2
		0.150	1.41	4250	0.34	20.3	20.3
	bcc	0.030	0.78	2400	0.34	7.4	7.4
		0.052	0.92	3080	0.34	11.6	11.6
		0.075	1.06	3590	0.35	14.7	14.7
		0.113	1.28	4210	0.34	19.3	19.3
		0.150	1.50	4670	0.34	22.5	22.5
	fcc	0.030	0.75	2400	0.34	7.9	7.9
		0.052	0.91	3140	0.34	12.0	12.0
		0.075	1.06	3700	0.34	14.7	14.7
		0.113	1.30	4410	0.34	17.9	17.9
		0.150	1.53	4940	0.34	21.2	21.2

Table I: Finite element results for adhesively bonded MHSS (St/Ep).

Morphology	Topology	t [mm]	ρ [g/cm^3]	E [N/mm^2]	ν [-]	$k_c = k_t$ [N/mm^2]
Partial	pc	0.030	0.43	570	0.19	1.5
		0.052	0.54	980	0.20	2.5
		0.075	0.64	1390	0.20	3.3
		0.113	0.81	2090	0.22	4.9
		0.150	0.98	2800	0.23	6.4
	bcc	0.030	0.67	2450	**-0.04**	1.6
		0.052	0.82	3890	**-0.01**	3.2
		0.075	0.95	5220	0.01	4.9
		0.113	1.18	7250	0.04	8.4
		0.150	1.39	9150	0.07	10.6
	fcc	0.030	1.01	3310	0.17	2.6
		0.052	1.16	4750	0.17	3.1
		0.075	1.31	6030	0.17	3.6
		0.113	1.55	7890	0.18	4.3
		0.150	1.78	9540	0.18	4.8
Syntactic	pc	0.030	4.51	58500	0.24	97.9
		0.052	4.62	60400	0.24	105.1
		0.075	4.73	62200	0.25	108.3
		0.113	4.90	65200	0.25	115.0
		0.150	5.06	68000	0.25	121.5
	bcc	0.030	3.78	37800	0.28	65.3
		0.052	3.93	40100	0.28	68.1
		0.075	4.06	42400	0.28	72.1
		0.113	4.29	46100	0.28	77.2
		0.150	4.50	49900	0.28	82.2
	fcc	0.030	3.50	31900	0.29	56.4
		0.052	3.66	34400	0.29	60.8
		0.075	3.81	36900	0.29	65.1
		0.113	4.05	41000	0.29	73.7
		0.150	4.28	45000	0.28	81.0

Table II: Finite element results for sintered and cast MHSS (St/St).

Morphology	Material	Topology	ρ [g/cm^3]	E [N/mm^2]	ν [-]	$k_c = k_t$ [N/mm^2]
Partial	Al/Ep	pc	0.19	365	0.12	0.23
	Al/Ep	bcc	0.26	690	0.13	0.28
	Al/Ep	fcc	0.33	675	0.18	0.42
	Al/Al	pc	0.25	740	0.21	0.27
	Al/Al	bcc	0.37	2780	0.02	0.38
	Al/Al	fcc	0.50	3220	0.18	0.29
Syntactic	Al/Ep	pc	0.85	2660	0.35	1.5
	Al/Ep	bcc	0.77	2760	0.35	1.4
	Al/Ep	fcc	0.74	3420	0.35	1.4
	Al/Al	pc	1.82	33500	0.274	8.8
	Al/Al	bcc	1.56	22600	0.30	5.8
	Al/Al	fcc	1.46	24000	0.31	5.3

Table III: Finite element results for aluminium MHSS (t = 0.075 mm, Al/Ep and Al/Al).

Material	ρ [g/cm^3]	E [N/mm^2]	$\sigma_{\max}$ [N/mm^2]	σ_{pl} [N/mm^2]
Partial	0.3	340	4	4
	0.6	730	11	8
Syntactic	0.75	1950	31	20
	1.2	2320	60	40

Table IV: Experimental results of the compressive testing of MHSS.

Appendix B - Thermal Properties of MHSS

Morphology	Topology	t [mm]	ρ [g/cm^3]	λ_{eff} [W/(m·K)]
Partial ($d_{\min} = 0.18$ mm)	pc	0.030	0.23	0.237
		0.052	0.36	0.298
		0.075	0.49	0.332
		0.113	0.69	0.364
		0.150	0.88	0.383
Syntactic ($d_{\min} = 0.18$ mm)	pc	0.030	1.02	0.775
		0.052	1.15	0.941
		0.075	1.27	1.035
		0.113	1.47	1.127
		0.150	1.66	1.179
Syntactic ($d_{\min} = 0.36$ mm)	pc	0.030	0.86	0.680
		0.052	0.97	0.790
		0.075	1.08	0.850
		0.113	1.25	0.905
		0.150	1.41	0.936
	bcc	0.030	0.78	0.808
		0.052	0.92	0.975
		0.075	1.06	1.070
		0.113	1.28	1.159
		0.150	1.50	1.210
	fcc	0.030	0.75	0.868
		0.052	0.91	1.066
		0.075	1.06	1.181
		0.113	1.30	1.290
		0.150	1.53	1.354

Table V: Finite element results for adhesively bonded MHSS (St/Ep).

Morphology	Topology	t [mm]	ρ [g/cm^3]	λ_{eff} [W/(m·K)]
Partial ($d_{\min} = 0.18$ mm)	pc	0.030	0.50	0.80
		0.052	0.63	1.29
		0.075	0.76	1.74
		0.113	0.96	2.46
		0.150	1.15	3.15
Syntactic ($d_{\min} = 0.18$ mm)	pc	0.030	5.32	22.5
		0.052	5.45	23.9
		0.075	5.58	25.3
		0.113	5.78	26.8
		0.150	5.97	28.6
Syntactic ($d_{\min} = 0.36$ mm)	pc	0.030	4.51	27.5
		0.052	4.62	28.4
		0.075	4.73	29.3
		0.113	4.90	30.7
		0.150	5.06	32.1
	bcc	0.030	3.76	22.2
		0.052	3.90	23.3
		0.075	4.04	24.3
		0.113	4.26	26.0
		0.150	4.47	27.6
	fcc	0.030	3.50	20.2
		0.052	3.66	21.3
		0.075	3.81	22.4
		0.113	4.05	24.2
		0.150	4.28	25.9

Table VI: Finite element results for homogeneous MHSS (St/St).

Appendix C - Mechanical Properties of Sandwich Structures

The geometric dimensions of sandwich structures correspond to Table 13. Al face sheets are aluminium Al5005.

Core material	Flexural Stiffness Eq. (64) [N/mm^2]	Load-carrying capacity [N]	Failure mode	Energy absorption [J]
Alporas®	5750	1700	CI	3.7 $^+$
M-Pore®	3300	700	CI	1.3 $^+$
Honeycomb	10300	940	CI / DL	5.8 $^+$
Partial MHSS	4100	2100	CI / CF	5.4
Syntactic MHSS	9600	3300	CF	3.7

Table VII: Mechanical properties of sandwich structures (averaged values).

Explanation of failure modes

CF: Core fracture
CI: Core indentation
DL: Delamination

Appendix D - Definition of Invariants

The general description of an arbitrary stress state requires the independence of particular coordinate systems. This aim can be achieved by representing the stress tensor by its invariants. Invariants are variables which are independent of the orientation of the coordinate system, but contain the same physical information as the stress tensor.

Based on the characteristic equation of the stress tensor

$$\det(\sigma_{ij} - \lambda\delta_{ij}) = 0 \tag{77}$$

the characteristic polynomial (78) can be deduced. The solution of this equation provides the eigenvalues λ_i of the stress tensor.

$$\lambda^3 - I_1\lambda^2 + I_2\lambda - I_3 = 0 \tag{78}$$

The main invariants are identical to the coefficients I_1, I_2 and I_3 of the characteristic polynomial. Based on these values, the following relations can be applied to calculate the base invariants J_1, J_2 and J_3:

$$J_1 = I_1 \tag{79}$$

$$J_2 = \frac{1}{2}{I_1}^2 - I_2 \tag{80}$$

$$J_3 = \frac{1}{3}{I_1}^3 - I_1 I_2 + I_3. \tag{81}$$

According to Fig. 107, the stress tensor σ_{ij} can be divided into a hydrostatic σ^o_{ij} and a deviatoric component s_{ij}.

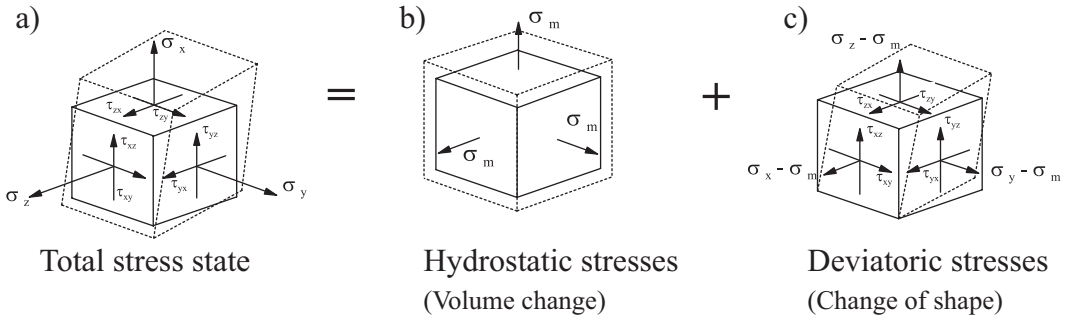

Figure 107: Decomposition of the stress tensor in its hydrostatic and deviatoric components [125].

Based on this decomposition, invariants describing the deviatoric ($'$) and hydrostatic stresses (^{o}) can be formulated. The definitions of these invariants are given in Table VIII.

Stress tensor		
σ_{ij}	σ^{o}_{ij}	s_{ij}
Base invariants		
J_1, J_2, J_3	$J^{\mathrm{o}}_1, J^{\mathrm{o}}_2, J^{\mathrm{o}}_3$	$J^{'}_1, J^{'}_2, J^{'}_3$
$J_1 = \sigma_{ii}$ $J_2 = \frac{1}{2}\sigma_{ij}\sigma_{ji}$ $J_3 = \frac{1}{3}\sigma_{ij}\sigma_{jk}\sigma_{ki}$	$J^{\mathrm{o}}_1 = \sigma_{ii}$ $J^{\mathrm{o}}_2 = \frac{1}{6}\left(\sigma_{ii}\right)^2$ $J^{\mathrm{o}}_3 = \frac{1}{9}\left(\sigma_{ii}\right)^3$	$J^{'}_1 = 0$ $J^{'}_2 = \frac{1}{2}\, s_{ij}s_{ji}$ $J^{'}_3 = \frac{1}{3}\, s_{ij}s_{jk}s_{ki}$
$\Rightarrow\ J_1, J_2, J_3$	$\Rightarrow\ J^{\mathrm{o}}_1$	$\Rightarrow\ J^{'}_2, J^{'}_3$

Table VIII: Definition of the base invariants [126].

Within the scope of the description of the stress state dependence on the deviatoric and hydrostatic base invariants, the following dependencies can be observed:

$$J^{\mathrm{o}}_2 = \tfrac{1}{6}(J^{\mathrm{o}}_1)^2 \qquad J^{o}_3 = \tfrac{1}{9}(J^{\mathrm{o}}_1)^3 \qquad J'_1 = 0.$$

Consequently, the number of required invariants for the unique description of an arbitrary stress state is reduced to the three base invariants J^{o}_1, J'_2 and J'_3.

Appendix E - Normalised Standard Deviation

In the scope of this work, the normalised standard deviation $\overline{\delta}(X)$ is use to quantify the scattering of material parameters X. The standard deviation $\delta(X)$ of n values is defined according to [127]

$$\delta(X) = \sqrt{\frac{\sum(X - \overline{X})^2}{(n-1)}}, \tag{82}$$

where $\overline{X}$ is the average value of the parameter X

$$\overline{X} = \frac{\sum X}{n}. \tag{83}$$

The normalised standard deviation $\overline{\delta}$ is obtained by dividing the standard deviation δ by the average value $\overline{X}$

$$\overline{\delta}(X) = \frac{\delta(X)}{\overline{X}}. \tag{84}$$